



**Politecnico
di Torino**

POLITECNICO DI TORINO

Master's degree course Aerospace Engineering

**Infield mini radio-probes measurements of physical fluctuations
inside warm clouds and environmental air**

Thesis associated with the EU project H2020

MSCA ITN ETN COMPLETE

Supervisor

Prof.ssa Daniela Tordella

Candidate

Pierpaolo Di Felice

Academic year 2022/2023

Graduation session April 2023

Abstract

Clouds are the key element that regulates the water cycle and the earth's energy balance. Nowadays, it is well known that the phenomena of cloud formation, droplet dynamics and turbulence are closely related; however, the reciprocal effects, descriptive and predictive models are still an open field of research. One of the reasons why the study of these phenomenologies is particularly challenging is the difficulty of being able to obtain accurate experimental data. For large scales, measurement campaigns are already being carried out, using large balloons or through appropriately equipped aircraft. For small scales, however, it is still challenging to be able to sample the characteristics of the atmosphere in a Lagrangian manner, for these reasons the COMPLETE H2020 project was born. It has the purpose of investigating these topics by making use of a new type of radiosonde, designing it, assembling it and launching it to collect new data. These radioprobes will necessarily have to be ultralight and biodegradable. They, floating on an isopycnic surface will collect thermodynamic (temperature, humidity, pressure) and positioning (position, velocity, acceleration) data and send them to ground receiving stations. In the course of this work, the basic aspects of turbulence and warm cloud physics will be explained; then, the components of the probe, the process of balloon sizing and realization will be described. At the end, a new experiment carried out in Valle d'Aosta in which ten probes were allowed to fly unconstrained will be presented and the results will be discussed. To conclude, the current situation of the project will be summarized and analyzed, and upcoming goals and possible improvements will be introduced.

Dedication

A tutte le persone che mi hanno ascoltato, sostenuto e spronato ad andare avanti.

Contents

1	Introduction	19
2	Turbulent flows	21
2.1	The approach to turbulent flows	22
2.2	The energy cascade	23
2.3	Entrainment	25
2.4	Diffusivity	26
3	Clouds, a key element for atmospheric dynamics and future research	28
3.1	Clouds classification	31
3.2	Warm clouds and droplet development	34
3.2.1	Particle activation	36
3.2.2	Relative motion	38
3.2.3	Droplet distribution	39
3.3	Turbulence influence	41
3.3.1	Effect of entrainment	42
3.3.2	Particle diffusion and Richardson approach	44
4	Radiosondes	48

4.1	Requirements and operating environment	50
4.2	Radiosondes design and system architecture	51
5	Aerostatical balloons	56
5.1	Materials	56
5.2	Physics	59
5.3	Sizing	63
5.3.1	Comparison with experimental results	65
5.4	PAWAN balloon testing	68
5.5	Assembly	71
5.6	A possible new shape	75
6	OAVdA experiment	76
6.1	Logistics and operations in Turin	77
6.1.1	Location of the experiment	78
6.1.2	Preparation, calibration and execution	79
6.2	Data from experiment	90
6.3	Richardson analysis and comparison with previous experiment	103
6.4	Validation by stereo vision	110
6.4.1	Preparation and setup	110
6.4.2	Stereo vision attempt through OpenCv	113
6.4.3	Length-to-pixel ratio variation method	116
7	Conclusions and future improvements	124

List of Figures

2.1	Energy cascade process: energy transfer from large scales to smaller scales. <i>Image taken from:"S.B. Pope and S.B. Pope. Turbulent Flows. Cambridge University Press, 2000" [39].</i>	24
2.2	Representation of the Entrainment process in a jet. <i>Image taken from:"Jimmy Philip and Ivan Marusic. Large-scale eddies and their role in entrainment in turbulent jets and wakes. Physics of fluids (1994), 24(5):055108–055108–10, 2012" [37].</i>	25
2.3	Representation of the dispersion phenomenon of a cluster of particles. <i>Image inspired by Lewis Fry Richardson. Atmospheric diffusion shown on a distance-neighbour graph. Proceedings of the Royal Society of London. 110(756):709–737, 1926. [42]</i>	26
3.1	The image shows the process of the water cycle, from evaporation to condensation to precipitation. <i>Image taken from:"NOAA. The water cycle. (dennis cain/nws). https://www.noaa.gov/education/resource-collections/freshwater/water-cycle. Accessed on 6 December 2022" [34].</i>	29

3.2	The complex situation of the Earth’s heat balance is shown in the image. Energy, arriving in the form of solar radiation will be partly absorbed and partly reflected. Clouds have a great influence on this process. <i>Image taken from: "Roger Williams University. Earth’s heat budget. https://rwu.pressbooks.pub/webboceanography/chapter/8-1-earths-heat-budget/. Accessed on 6 December 2022"</i> [49].	30
3.3	Classification currently adopted by the WMO for cloud types [15].	31
3.4	On the left: Cirrus: common clouds located over 6000 meters above sea level and unable to produce precipitation that reaches the ground. <i>Image taken from: "P. Kratochvil. https://www.publicdomainpictures.net/en/free-download.php?image=cirrus-clouds&id=438663. Accessed on 23 March 2023"</i> [20]. On the right: Stratiform clouds: this family of clouds can form at low to medium altitudes and are capable of generating drizzle to persistent precipitation. <i>Image taken from: "Ralph F. Kresge. Noaa photo library. weather wonders, clouds, stratus. https://photolib.noaa.gov/Collections/National-Weather-Service/ Other/emodule/627/eitem/18666. Accessed on 10 December 2022"</i> [21].	32

3.5	<p>On the left: Cumulus clouds: these clouds are generated by convection at low altitude and usually do not result in precipitation. Under appropriate conditions they can grow and generate rainfall. <i>Image taken from: "L. Mallette. https://www.publicdomainpictures.net/it/view-image.php?image=290510&picture=cumuli. Accessed on 23 March 2023"</i> [31].</p> <p>On the right: Fully developed cumulonimbus: this type of cloud extends from a base usually located below 2000 meters altitude to the tropopause. They can give rise to extremely heavy rain, hail and lightning. <i>Image taken from: "Meteorologiaenred. Cumulonimbus. https://www.meteorologiaenred.com/it/cumulonembi.html. Accessed on 10 December 2022"</i> [32].</p>	33
3.6	<p>Droplet growth. Condensation, collection and the gap between the two mechanisms. <i>Image taken from: "Dennis Lamb and Johannes Verlinde. <i>Physics and Chemistry of Clouds</i>. Cambridge University Press, Cambridge, 2011"</i> [26]. . .</p>	35
3.7	<p>Activation process viewed through the Köhler equation. The abscissae shows the radius of the particles while the ordinates show the saturation of the environment. The process takes place in a supersaturated environment. <i>Image taken from: "Dennis Lamb and Johannes Verlinde. <i>Physics and Chemistry of Clouds</i>. Cambridge University Press, Cambridge, 2011"</i> [26].</p>	37
3.8	<p>Droplet development within a typical cloud. On the left is shown the supersaturation trend considering a particle passing through the base of the cloud. On the right, the growth and eventual activation of three particles of different sizes is shown. <i>Image taken from: "Dennis Lamb and Johannes Verlinde. <i>Physics and Chemistry of Clouds</i>. Cambridge University Press, Cambridge, 2011"</i> [26].</p>	38

3.9	Spatial distribution of: (a) drop diameter [μm], (b) drop concentration [$\frac{n}{m^3}$], (c) water content [$\frac{g}{m^3}$]. Droplet size and water content are found to be higher at the upper part of the cloud while the concentration in number doesn't vary significantly with height. <i>Image taken from: "Hans R Pruppacher and J. D Klett. Microphysics of Clouds and Precipitation. Springer Science + Business Media, Dordrecht, 2. aufl. edition, 2010" [40].</i>	40
3.10	Droplet measurement made by sampling at $1000Hz$ during a flight within cumulus. It is possible to see the huge inhomogeneity present in the clouds, with peaks, uniform regions, and discontinuous areas. <i>Image taken from: "P.R. Jonas. Turbulence and cloud microphysics. Atmospheric research, 40(2):283-306, 1996" [19].</i>	41
3.11	Representation of the interface between cloud and clean air. Above is shown a hypothetical initial instant with the two environments clearly separated while below is shown a following situation in which an interface zone has been generated where the humid shell and dilution region can be identified. <i>Image taken from: "Mark Pinsky and Alexander Khain. Theoretical analysis of the entrainment-mixing process at cloud boundaries. part i: Droplet size distributions and humidity within the interface zone. Journal of the Atmospheric Sciences, 75(6):2049 - 2064, 2018" [38].</i>	43
3.12	Example of a distance-neighbour graph representing a case of constrained diffusion. More specifically, the evolution of 4 helium-filled balloons tied to the ground by a thread is shown. The distance parameter h was chosen as $h = 5m$	46
4.1	Operational requirements of the radiosondes [35].	50

4.2	System architecture of wireless sensor network (WSN). The information transmitted by the probes will be collected by ground stations and then sent to a processing machine.	51
4.3	PCB internal structure: the block diagram shows the interconnections between the various radioprobe modules.	52
4.4	Photo of the printed circuit board with the modules mounted.	52
4.5	Table showing the physical dimension of the PCB.	53
4.6	Sensors specifications [35] [5] [28] [47].	55
5.1	Contact angle of a drop on a solid material.	58
5.2	Representation of the forces acting on the balloon: balance between gravity and hydrostatic thrust.	60
5.3	Variation of air properties with altitude. The table shows the values of the ICAO standard atmosphere.	61
5.4	Example of the relationship between helium volume and buoyancy altitude for a probe-balloon with a fixed weight of 20g. It can be seen that to increase the buoyancy altitude from 500m to 2500m the volume must be increased by about 20%.	62
5.5	Balloon weight trend based on the assumption of spherical geometry and specific weight of material equal to $21 \frac{g}{m^3}$	63
5.6	Trend of net transportable weight (buoyancy) as the size of the mater-bi balloon changes. Assumptions were spherical geometry and density at sea level.	64
5.7	Weights of probe parts.	64
5.8	Size chosen to produce the balloons for the 3/11/22 experiment: 25g of liftable weight (buoyancy) at sea level corresponding to a radius of 0.20m. .	65

5.9	Comparison of balloon weights measured in the laboratory and the previously developed theoretical trend. The measurement uncertainties are as follows: radius measurement ± 0.5 cm; weight measurement ± 1 g. The difference between the two trends can be explained because there is more material in the balloons than in the ideal sphere.	66
5.10	Comparison of lifting capacity (buoyancy) measured on balloons in the laboratory (250m altitude) and that assumed. The measurement uncertainties are as follows: radius measurement ± 0.5 cm; liftable weight measurement ± 0.1 g.	67
5.11	Measured properties of balloons for the experiment.	68
5.12	PAWAN balloon inflated and ready for testing.	69
5.13	the table above shows the main characteristics of the balloon.	69
5.14	graph showing the performance comparison between Mater-Bi and PAWAN balloons. Measurements were conducted at Politecnico di Torino, at an altitude of about 250m. The measurement uncertainties are as follows: radius measurement ± 0.5 cm; floating capacity measurement ± 0.1 g.	70
5.15	Hand wheel sealer with knob for changing temperature and the silicone placemat.	72
5.16	Templates made of cardboard and some tools used: scissors and scalpel. . .	73
5.17	Cad model of the balloon with dimension in centimeters.	73
5.18	Balloons ready to be launched.	74
5.19	A possible new balloon geometry, stronger than the previous one.	75

6.1	Saint-Berthélemy Valley and OAVdA observatory, shot from above. <i>Image taken from: "Paolo Rey. Regione autonoma valle d'aosta per il progetto transfrontaliero interreg alcotra "exo/eco" realizzato con fondi europei. https://www.oavda.it/chisiamo. Accessed on 06 January 2023" [41].</i>	79
6.2	On the left: the ten radiosondes that will be mounted; on the right: the antenna ready to receive signals.	80
6.3	Photo of balloon inflation.	81
6.4	Calibration phase: temperature measurement by INRiM instrumentation and mounted probes.	81
6.5	Comparison of temperature data from INRiM instrumentation and radiosondes. It is possible to see that radiosondes have a tendency to slightly overestimate the temperature by a few degrees.	82
6.6	Calibration of temperature data based on probe averaging. The difference between the average of all temperatures and the values measured by instrumentation was subtracted from each curve obtained by radiosonde.	83
6.7	Table representing the mean temperature error obtained by averaging the data from all probes and the maximum absolute error of the individual probe.	83
6.8	Calibrated temperature for each individual probe. To the values of each radiosonde was subtracted its average error compared with the instrumentation.	84
6.9	Relative humidity measured during the calibration phase. Although the measured data are slightly different, the probes measure concordant trends.	85

6.10	Comparison of relative humidity data measured by the Vaisala probe and that of the COMPLETE project (9/06/21 experiment, Levaldigi airport). It can be seen that although there is a difference between the measured values the trends are comparable: maximum and minimum peaks tend to be detected by both probes.	86
6.11	Atmospheric pressure measured during the temperature calibration phase. It is possible to notice immediately that something is wrong: all probes measured constant values of pressure.	87
6.12	Balloons a few moments before launching: they will be released all together from the same spot.	88
6.13	Balloons launched: first moments of flight.	88
6.14	Images taken about 10 and 40 seconds after launch, respectively. It can be seen that the probes proceed in a cluster and follow the air swirls.	89
6.15	The top image shows the path taken as a function of time by all working probes while the bottom image for three selected ones; some of them reached 45 minutes of broadcast time.	91
6.16	The two images show the distance traveled by all working probes and for three selected probes, respectively; some of them reached up to 5 kilometers.	92
6.17	The two images show the path followed by three selected probes and their relative elevation. Due to double balloons per probe, high altitudes of over 3500 meters were reached.	93
6.18	Pressure data recovered from GNSS module and barometric formula.	95

6.19	The two graphs above show the change in relative humidity for all probes and for three of them selected. It is possible to observe that although most of them reached the cloud base none detected values close to saturation; peaks were measured, however.	96
6.20	The two graphs above show the change in temperature for all probes and for three of them selected. It is possible to see a change of slope in the vertical thermal gradient (considering the almost constant rate of increase in altitude): this could represent the entry into saturated air (clouds) by the probes.	97
6.21	The four graphs show spectral analysis for temperature (top) and relative humidity (bottom) measurements for three selected radiosondes. The data are plotted in log-log axes; two trend lines were added for comparison. Because the original data have irregular time intervals the datasets were resampled at regular 5-second intervals.	99
6.22	The two graphs show spectral analysis for wind speed measurements for three selected radiosondes. The data are plotted in log-log axes; two trend lines were added for comparison. Because the original data have irregular time intervals the datasets were resampled at regular 5-second intervals. . .	100
6.23	Top image: absolute velocity for three selected probes; bottom image: velocity along the vertical (down) axis. Some probes show an increase in speed with time; this, could be due to the marked increase in altitude.	101
6.24	Top image: velocity along the longitudinal (east) axis for three probes selected; bottom: velocity along the latitudinal (north) axis.	102

6.25	Plot of the position of probes at successive instants of time in a NED-type coordinate system. It is possible to see that the evolution of balloon positioning occurs in cluster.	103
6.26	Distance-neighbor graph related to the 10/02/22 experiment at OAVdA. The dispersion of 4 balloons tied to the ground by a thread about 15 meters long is shown. The distance parameter h was chosen to be 5 meters. The effect of the constraints is clearly visible; the peaks oscillate around distances of about 20 meters (1).	104
6.27	Distance-neighbor graph related to the 10/02/22 experiment at OAVdA. The dispersion of 4 balloons tied to the ground by a thread about 15 meters long is shown. The distance parameter h was chosen to be 5 meters. The effect of the constraints is clearly visible; the peaks oscillate around distances of about 20 meters (2).	105
6.28	Experimental setup on 10/02/22 at OAVdA with ground-tied probes.	105
6.29	Distance-neighbor graph concerning the unconstrained dispersion of 7 balloons using $h = 20m$ as distance parameter. The first 3 instants of time considered (0s, 150s, 300s) are shown. The effects of the absence of constraints in the dispersion can be seen: the peaks move to higher mutual distances and the curves tend to flatten.	106
6.30	Distance-neighbor graph concerning the unconstrained dispersion of 7 balloons using $h = 20m$ as distance parameter. The last 3 instants of time considered (300s, 450s, 600s) are shown. Having used a low h value, it can be seen that the curves have many slight sparse peaks; there are not enough particles within the cells to make a good statistic.	107

6.31	Distance-neighbor graph concerning the unconstrained dispersion of 7 balloons using $h = 50m$ as distance parameter. The first 3 instants of time considered (0s, 150s, 300s) are shown.	107
6.32	Distance-neighbor graph concerning the unconstrained dispersion of 7 balloons using $h = 50m$ as distance parameter. The last 3 instants of time considered (300s, 450s, 600s) are shown. The value of h chosen for this graph seems to be a good compromise to describe this dispersion situation.	108
6.33	Distance-neighbor graph concerning the unconstrained dispersion of 7 balloons using $h = 100m$ as distance parameter. The first 3 instants of time considered (0s, 150s, 300s) are shown. Having used a high h value, it can be seen that the resolution of the graph is quite low.	108
6.34	Distance-neighbor graph concerning the unconstrained dispersion of 7 balloons using $h = 100m$ as distance parameter. The last 3 instants of time considered (450s, 600s, 900s) are shown. It is possible to see that after a large time interval (900s) some balloons reached considerable distances from each other, in the range of 400-600 meters.	109
6.35	Sony HDV camera ready to shoot and freshly painted balloon.	112
6.36	Schematic representation of the position of the cameras and their field of view, in relation to the launch position.	113
6.37	Concept of disparity: difference in the placement of an object on two frames taken from different positions.	114
6.38	Tracker test. In the three consecutive frames it is shown how the algorithm loses tracking of the red balloon as soon as another one approaches it. . . .	115
6.39	Black-white chessboard, reference figure for OpenCv camera calibration. . .	115

- 6.40 Objects taken as reference to find an interpolating law. A cardboard box was used for the first three data, and a segment of a fence was taken for the fourth. The measurements are relative to the horizontal axis. 117
- 6.41 Trend obtained by interpolating with a power law the reference ratios measured and given in the table above. The interpolating function is: $y = a(x^b) + c$ where x is the length-pixel ratio, y is the distance to the camera, $a = 14.59$, $b = 1.518$ and $c = 3.078$ 117
- 6.42 Comparison of distances obtained from GNSS and camera vision between the black balloon and camera A. The two horizontal lines represent the nearest (21.8m) and furthest (24.0m) position seen by the camera during the oscillation around the fence, respectively. Also, the nearest and farthest position obtained from the GNSS were highlighted: $16.2 \pm 6.2\text{m}$, $25.7 \pm 6.6\text{m}$. 119
- 6.43 Comparison of distances obtained from GNSS and camera vision between the black balloon and camera B. The two horizontal lines represent the nearest (20.3m) and furthest (22.3m) position seen by the camera during the oscillation around the fence, respectively. Also, the nearest and farthest position obtained from the GNSS were highlighted: $16.7 \pm 7.3\text{m}$, $22.3 \pm 7.3\text{m}$. 119
- 6.44 Comparison of distances obtained from GNSS and camera vision between the yellow balloon and camera A. The two horizontal lines represent the nearest (22.5m) and furthest (24.9m) position seen by the camera during the oscillation around the fence, respectively. Also, the nearest and farthest position obtained from the GNSS were highlighted: $20.9 \pm 7.3\text{m}$, $28.9 \pm 7.7\text{m}$. 120

- 6.45 Comparison of distances obtained from GNSS and camera vision between the yellow balloon and camera B. The two horizontal lines represent the nearest (20.8m) and furthest (22.6m) position seen by the camera during the oscillation around the fence, respectively. Also, the nearest and farthest position obtained from the GNSS were highlighted: $19.1 \pm 7.3\text{m}$, $25.7 \pm 7.7\text{m}$. 120
- 6.46 The graph shows the comparison of the relative distance between the black and yellow balloons (RS21, RS22) obtained by GNSS and camera during oscillation at the fence. It is possible to observe a discrepancy between the two curves, however, the difference lies within the tolerance calculated for the measurements obtained from the GNSS modules. 122
- 6.47 Table showing the relative distances during the oscillation at the fence between the black and yellow balloon (RS21, RS22) obtained by GNSS and camera. A period of about three minutes was analyzed. Uncertainties are high because two data from the GNSS module are used to calculate the relative distance. 122

Chapter 1

Introduction

Since ancient times mankind has always marveled at looking up and observing the sky: the stars, planets the moon but also clouds and weather phenomena have represented a kind of boundary into the unknown, since there was no logical explanation for the motion of the stars or the evolution of the atmosphere. Today, thanks to scientific advances and modern technologies, it has been possible to answer many questions and even explore outer space. Despite this, the ability to predict cloud evolution and its meteorological developments is still a frontier field of scientific research. Turbulence and the behavior of droplets in clouds are phenomena that are not yet fully understood.

To study the dynamics of motions within clouds, it is necessary to consider that different spatial scales are involved, ranging from nanometers, where nucleation and coalescence of droplets occurs, to the kilometer range where gusts and atmospheric motions play a predominant role. In order to obtain data in a Lagrangian way, ultralight green radiosondes can be used that can passively track fluctuations in temperature, humidity, pressure, and velocity along an isopycnal surface for a couple of hours. They will operate at an altitude of one to three kilometers through warm clouds and clean air [1]. The probes will be

carried in the airflow motions by lightweight balloons made specially for this purpose. To minimize environmental impact, they will be made with a biodegradable material selected on the basis of properties like strength, flexibility and hydrophobicity. Other research groups have already tried to investigate these themes by means of special aircrafts (in a non lagrangian way) such as the "CIRPAS twin otter" capable of measuring fluctuations in velocity, temperature and liquid water content using high-tech fast-response instruments with spatial resolution of 1 meter [29]. Lagrangian way experiments have been carried out by NOAA by releasing large balloons with heavy probes floating over the ocean at altitudes ranging from 500 to 1500 meters [7].

The ultimate purpose of this work is to fill the gap present in the knowledge of small scales fluctuations for understanding the unsteady cycle of warm clouds life by using smaller and lighter balloons than before [1]. The capacity of gather such experimental data in an economically and environmental sustainable way will be very helpful for further studies.

The next chapters provide a bibliographical introduction regarding the phenomena of turbulence, cloud formation, and the influence turbulence has on condensation and accretion processes. Chapters 4 and 5 explain the structure of probes and balloons, the study of sizing, and assembly processes. In Chapter 6, the experiment conducted will be discussed and the results obtained will also be compared with those of the previous experiment. Finally, a concluding paragraph will follow where in addition to recalling the most important and interesting aspects, possible future developments will be proposed.

Chapter 2

Turbulent flows

Observing turbulent flows is not unusual, in fact they prove to be very common: water flowing down a river, wind whirling leaves or smoke coming out of a chimney; these are all examples of common turbulent flows that we can experience in everyday life.

The transition from laminar to turbulent state is caused by the inherent instability of a laminar flow when the Reynolds number becomes high; this increase means that inertial forces become very dominant over viscous ones [39].

Reynolds number, which is a non-dimensional parameter, is expressed as follows:

$$Re = \frac{\rho V L}{\mu} = \frac{V L}{\nu}$$

Where:

- ρ is the density of the fluid;
- V is the flow speed;
- L is a characteristic length;

- μ is the dynamic viscosity;
- ν is the kinematic viscosity.

It is possible to describe turbulence as a random, time- and space-dependent process with a large number of degrees of freedom. In a fully developed turbulence flow we can observe that all scales are coexistent, from the smallest determined by viscosity to the largest determined by the environment. The presence of eddies of different sizes accounts for the greater diffusivity than laminar flows [39].

The following chapters will show some turbulent phenomena that are found to have a great impact on the atmospheric physics of clouds.

2.1 The approach to turbulent flows

Over time, several methods have been adopted to describe turbulent flows. Three areas of investigation can be identified [39].

1. **Discovery:** experimental studies to improve understanding of certain phenomenologies.
2. **Modelling:** Theoretical or computational studies with the goal of developing mathematical models that can accurately describe the characteristics of a turbulent flow.
3. **Control:** Practical studies with the purpose of manipulating a turbulent flow to achieve some kind of benefit, such as reducing drag, controlling a boundary layer, or governing a mixing phenomenon.

Considering the second area, we have that the Navier stokes equations completely and in detail describe both laminar and turbulent flows. However, the amount of data that would involve these types of simulations would be enormous, making them effectively inapplicable

for direct approaches to high Reynolds number flows; for low Reynolds number flows and simple geometries, however, they turn out to be widely used [39].

If the governing equations of fluid motion are deterministic, why do the solutions turn out to be random? The answer to this question is due to a combination of two factors: the first is that in every turbulent flow there are unavoidable perturbations to the initial boundary conditions; the second is that turbulent motion fields turn out to be extremely sensitive to these kinds of perturbations [39]. A statistical approach will have to be used to model high Reynolds number flows, which turn out to be very common in practical applications [39].

Being able to access a large amount of information in a sustainable way (position, velocity, temperature, humidity) through biodegradable ultra-light balloons will help advance knowledge about atmospheric turbulence and clouds physics. This type of study falls into the first area of investigation but that in turn will make possible the establishment and validation of computational models.

2.2 The energy cascade

As mentioned earlier, in a turbulent flow, the coexistence of a large number of different spatial scales is observed. Therefore, there will be a mechanism that regulates the energy exchange between the different scales. The idea of the energy cascade was formulated by Richardson in 1922; briefly, it states that in turbulence kinetic energy is fed into the flow at the large scales; this energy will then be transferred to smaller scales by an inertial process. This mechanism will go on until smaller scales are reached where viscosity will no longer be negligible and will act by dissipating energy into heat. These small scales are called "Kolmogorov scales". [39]. By definition, turbulent flows possess nonzero vorticity. One of the fundamental mechanisms on which the energy cascade process is based is the so-called

"Vortex stretching," where, in order for angular momentum to be conserved a stretching is associated with an increase in vorticity in the same direction as the stretching. By definition, turbulent flows possess nonzero vorticity. One of the fundamental mechanisms on which the energy cascade process is based is the so-called "Vortex stretching," where, in order for angular momentum to be conserved a stretching is associated with an increase in the vorticity component of the same direction as the stretching [25].

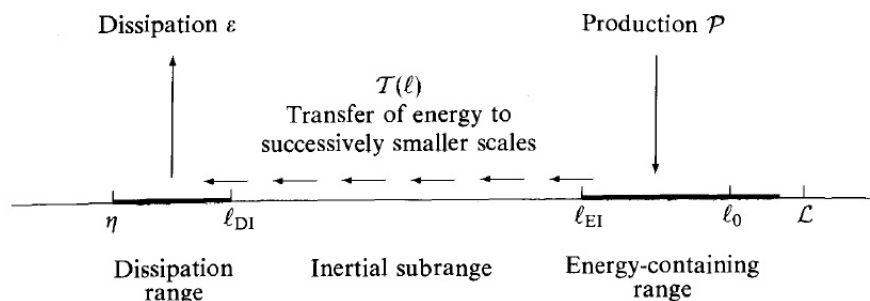


Figure 2.1: Energy cascade process: energy transfer from large scales to smaller scales. Image taken from: "S.B. Pope and S.B. Pope. *Turbulent Flows*. Cambridge University Press, 2000" [39].

In other words, the cascade continues until a sufficiently low Reynolds number is reached, where fluid motion is stable and viscosity can dissipate kinetic energy. Subsequent studies by Kolmogorov led to the assertion that for sufficiently high Reynolds numbers the smaller scales assume universal behavior, that is, they are completely independent of the larger scales. Small-scale turbulent motion was seen to be statistically isotropic with a universal form that is uniquely determined by ν and ε which is the dissipation rate; it is determined by the first step in this process, the transfer of energy from large scales; a trend equal to $\frac{V_0^3}{L_0^2}$ can be assumed (the subscript "0" indicates the largest structures) [39].

2.3 Entrainment

Another relevant phenomenon that occurs in free-shear turbulent flows is the so-called "entrainment". It has been observed that a flow in movement is able to "drag" in its motion the irrotational flow around it through "frictional" effects. The cause of this "friction" is viscosity in laminar flows and inertia in turbulent flows (with much greater effectiveness) [25]. For example, we can suppose that we observe a jet blowing from a hole in a calm environment. We can see that the boundary layer of the jet tends to become very unstable and turbulent, creating entrainment of the stationary ambient fluid into the moving one. In the following image we can see a representation of this phenomenon with an example of a jet:

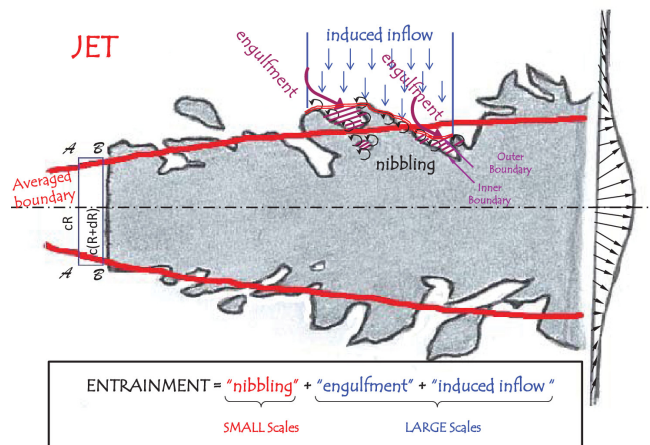


Figure 2.2: Representation of the Entrainment process in a jet. *Image taken from: "Jimmy Philip and Ivan Marusic. Large-scale eddies and their role in entrainment in turbulent jets and wakes. Physics of fluids (1994), 24(5):055108-055108-10, 2012" [37].*

As is shown in the image above the entrainment process can be seen as composed of three mechanisms involving both small and large scales: the process of "nibbling" for the first ones and "engulfment" and "induced inward motion" for the second [37]. The same processes also occur in atmospheric situations; for example, we can see that entrainment

plays a very important role in the evolution of the upper section of warm clouds and has a lot of influence on the activation of CCNs (Cloud Condensation Nuclei) [36]. These last phenomena will be discussed in detail in the following paragraphs.

2.4 Diffusivity

In a stationary fluid or laminar flow we have that diffusion occurs essentially by molecular agitation; this process turns out to be very slow. By an essentially statistical factor we will have that the net flow of the molecules in question will be directed from areas of higher concentration toward those of lower concentration until a homogeneous situation is reached. In the case of turbulent flows this diffusion process is drastically accelerated by the so-called "eddy diffusion". Thanks to the large-scale motions, the fluid particles are rapidly transported over much longer lengths resulting in a much more effective mixing process. The study of diffusion in turbulent flows is still a source of debate today. Several models have been developed over the years, however, there is still no model that is based on fundamentals of physics capable of giving a sufficient explanation of all the inherent aspects [39] [42].

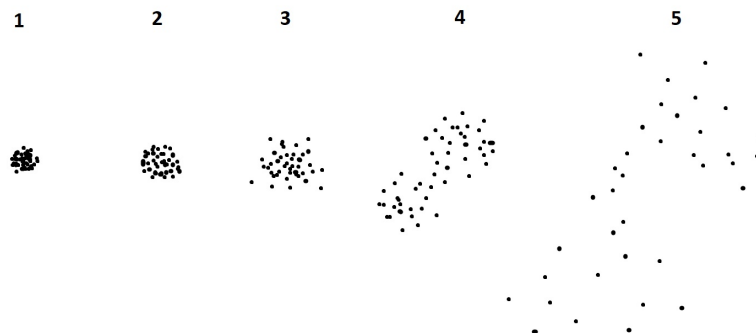


Figure 2.3: Representation of the dispersion phenomenon of a cluster of particles. *Image inspired by Lewis Fry Richardson. Atmospheric diffusion shown on a distance-neighbour graph. Proceedings of the Royal Society of London. 110(756):709–737, 1926. [42]*

The above images show a diffusion phenomenon of a cluster of particles. In the first images it is possible to see the action of molecular diffusion spreading the particles in a spherical way. In the latter, however, we can see the greater diffusive action of turbulent motions.

As mentioned previously, these topics will be detailed in the following paragraphs.

Chapter 3

Clouds, a key element for atmospheric dynamics and future research

The systematic study and classification of clouds did not begin until the turn of the 18th and 19th centuries, later than many other branches of science. A first classification based on altitude was proposed by a French naturalist, Jean-Baptiste Lamarck; unfortunately, due to the fact that he wrote the results of his research in French, his work was not widely circulated. Only a year later an English pharmacist, Luke Howard, proposed another subdivision based this time on shape, but which in fact also goes on to generate an altimetric differentiation. This time, because Latin (the universal language of science at the time) was used for terminology, the classification was widely accepted and is still the one used today [15].

Another thesis that proved to be instrumental in starting the study of the physics of clouds is the theory of chemist-physicist John Dalton, who also in the same period stated

that in clouds there are no elements that "float" by their own nature as previously thought, but, that all suspended droplets are actually continuously falling under the effect of Earth's gravity. This thesis was also taken up by Howard, who was convinced that clouds are quite different from being "airy nothings", but instead are elements subject to "the same fixed laws which pervade every other department of Nature" (Howard, 1804) [15].

Nowadays it is well established that clouds are anything but "airy nothings" as they strongly contribute to environmental processes in many different ways. For example, they are responsible for the functioning of the water cycle, condensing atmospheric humidity into droplets and then causing them to precipitate to the ground. This then, in the case where it remains liquid goes directly to replenish aquifers and springs directly usable by both humans and animals; in the case where it freezes, it will fall to the ground as snow while also going to feed snowfields and glaciers in mountainous areas, which will provide a water supply for the following warm months [26].

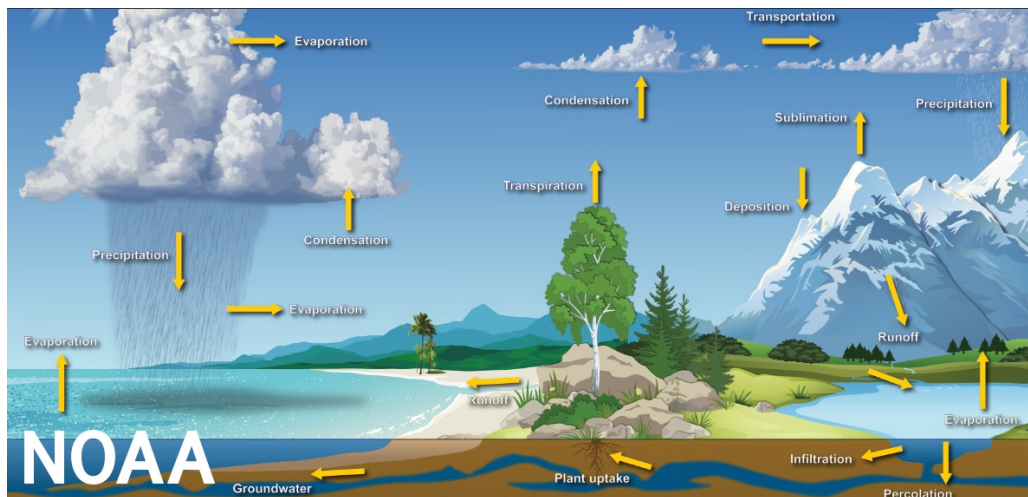


Figure 3.1: The image shows the process of the water cycle, from evaporation to condensation to precipitation. *Image taken from: "NOAA. The water cycle. (dennis cain/nws). <https://www.noaa.gov/education/resource-collections/freshwater/water-cycle>. Accessed on 6 December 2022" [34].*

Rain is also capable of transporting chemicals, in fact, in order to condense humidity it needs a condensation nucleus that can be a dust, for example, or other chemical compounds. The rain that is generated will therefore also be able to bring in nutrients but also to spread pollutants. Less evident but still important is the contribution that clouds make in regulating the energy balance of the atmosphere. They are able both to reflect solar radiation directly back upward and to intercept infrared radiation from the earth that would otherwise be lost into space [26].

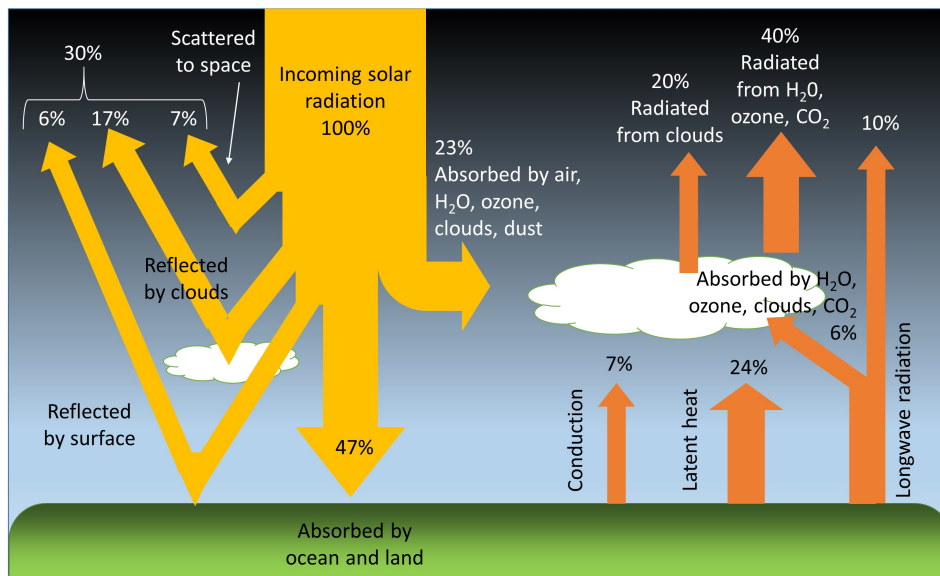


Figure 3.2: The complex situation of the Earth's heat balance is shown in the image. Energy, arriving in the form of solar radiation will be partly absorbed and partly reflected. Clouds have a great influence on this process. *Image taken from: "Roger Williams University. Earth's heat budget. <https://rwu.pressbooks.pub/webboceanography/chapter/8-1-earths-heat-budget/>. Accessed on 6 December 2022" [49].*

So, it turns out to be clear why being able to predict the evolution of clouds turns out to be a crucial achievement.

3.1 Clouds classification

As mentioned in the section above, the classification used nowadays is still based on the one proposed by Howard in the early 1800s, which has been given additions and minor modifications over time. Today's subdivision proposed by the World Meteorological Organization (WMO) divides clouds into 10 genera based on the altitude of the base and the shape the cloud takes [15]. The appearance in particular, can be indicative of the behavior (stability) of the cloud; it may be stable or have an evolution that will generate meteorological phenomena such as precipitation and electrical activity.

Altitude	Genera
High clouds: basis generally over 6 km	0 – Cirrus (Ci)
	1 – Cirrocumulus (Cc)
	2 – Cirrostratus (Cs)
Medium clouds: basis generally between 2 and 6 km	3 – Alto cumulus (Ac)
	4 – Altostratus (As)
	5 – Nimbostratus (Ns)
Low clouds: basis generally under 2 km	6 – Stratocumulus (Sc)
	7 – Stratus (St)
	8 – Cumulus (Cu)
	9 – Cumulonimbus (Cb)

Figure 3.3: Classification currently adopted by the WMO for cloud types [15].

A brief description of some representative types will follow; photographs will also be featured.

- **Cirrus.** All types belonging to the high clouds, are a type of cirrus. They are very common and can be observed at all times of the year. Cirrus occur as short, detached clouds that are whiter than the other types because they are composed entirely of ice crystals. They form as a result of the rise of quite dry air at the advance of a warm front. These clouds are associated with stable but changing weather due to

the arrival of a new front; technically they can produce precipitation which does not reach land anyway by re-evaporating along the descent [48].

- **Stratus.** Clouds that have no observable characterization and appear to be composed of multiple layers are described as stratus. They may be low, even at ground level (fogs) capable of generating faint drizzle; or they may be mid-altitude, called altostratus. These clouds form at the head of a warm or occluded front, and as they condense, they can evolve into nimbostratus, a dark gray cloud type capable of generating persistent and heavy precipitation of rain or snow [48].



Figure 3.4: On the left: Cirrus: common clouds located over 6000 meters above sea level and unable to produce precipitation that reaches the ground. *Image taken from: "P. Kratochvil. <https://www.publicdomainpictures.net/en/free-download.php?image=cirrus-clouds&id=438663>. Accessed on 23 March 2023" [20].* On the right: Stratiform clouds: this family of clouds can form at low to medium altitudes and are capable of generating drizzle to persistent precipitation. *Image taken from: "Ralph F. Kresge. Noaa photo library. weather wonders, clouds, stratus. <https://photolib.noaa.gov/Collections/National-Weather-Service/Other/emodule/627/eitem/18666>. Accessed on 10 December 2022" [21].*

- **Cumulus.** One of the most characteristic clouds are cumulus, shaped like a fluffy cauliflower, always generated by convection. They are common on sunny days, but if certain conditions are present they can evolve into very large, towering structures called cumulonimbus. The base of these clouds is generally flat and can be found

on the order of hundreds of meters in height but they are marked by a very high vertical development, in fact, the top can reach the tropopause (about 10 km at mid-latitudes) and the cloud to continue growing is forced to assume an anvil shape. These clouds are associated with intense even torrential rains that can also produce hail, lightning and thunder [48].



Figure 3.5: On the left: Cumulus clouds: these clouds are generated by convection at low altitude and usually do not result in precipitation. Under appropriate conditions they can grow and generate rainfall. *Image taken from: "L. Mallette. <https://www.publicdomainpictures.net/it/view-image.php?image=290510&picture=cumuli>. Accessed on 23 March 2023" [31].* On the right: Fully developed cumulonimbus: this type of cloud extends from a base usually located below 2000 meters altitude to the tropopause. They can give rise to extremely heavy rain, hail and lightning. *Image taken from: "Meteorologiaenred. Cumulonimbus. <https://www.meteorologiaenred.com/it/cumulonembi.html>. Accessed on 10 December 2022" [32].*

3.2 Warm clouds and droplet development

The study that will be carried out in this research project is related to so-called warm clouds, which are low-altitude clouds (usually with a base below 2 km) characterized by the presence of water only in the liquid state, so above zero temperatures and the absence of snowflakes and ice.

Usually a warm cloud is generated by simple rising of a moist air mass, either due to a slow ascent on a synoptic scale or a rapid rise due to convection, above the thermodynamic cloud base (100% relative humidity). Taking a simplified case as an example, we can observe what happens to a moist air mass containing dry particles (most of which have diameters of about $0.02\mu\text{m}$ but with the presence of others with larger sizes as well) subjected to an adiabatic ascent from near the surface. As the air mass rises it expands and cools, so the relative humidity within the particles increases until they become liquid droplets by deliquescency (the particles were assumed to be water-soluble). Due to the great competition for the finite excess of vapor (supersaturation condition) the growth of droplets by condensation appears to be very slow; a colloidal state remains persistent (i.e., a system that can be classified neither as homogeneous single-phase nor heterogeneous multiphase). This colloidal system formed by small droplets suspended in the air turns out to be very stable in warm clouds and can last for a long time. The droplets in this state interact very little with each other since they can faithfully follow the motions of the air. The only mechanism capable of breaking the colloidal state in warm clouds is the collision of droplets, the result of which is coalescence into a larger droplet; this process is called collection. To make collisions between the various droplets possible, there must obviously be significant relative movement between them, whether caused by turbulence or sedimentation; as well as requiring a sufficiently large size. It is therefore not to be taken for granted that the collection mechanism can take place; the situation is illustrated in the graph below [26].

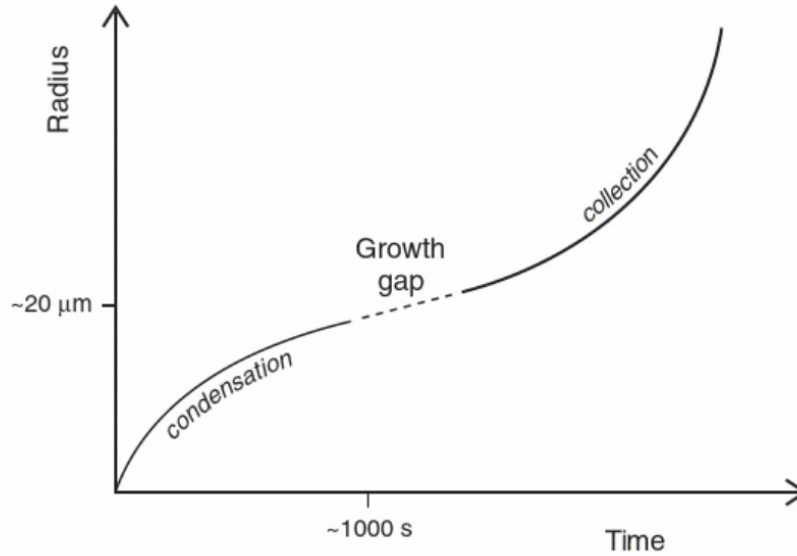


Figure 3.6: Droplet growth. Condensation, collection and the gap between the two mechanisms. *Image taken from: "Dennis Lamb and Johannes Verlinde. Physics and Chemistry of Clouds. Cambridge University Press, Cambridge, 2011" [26].*

In the above image, it can be seen that there is a size gap between the growth mechanism by condensation and the one by collection. The first one, in fact, can only form very small droplets with a radius of less than $20\mu m$, in contrast, the second process requires sizes larger than $20\mu m$ to be activated. The growth behavior of the droplets in this gap and consequently the initiation of the collection mechanism does not yet appear to be known, however, it is suspected that a not negligible role is to be attributed to the amount and size of aerosol particles initially present in the rising air mass. For example, if few droplets are present for a given vapor excess, there will be a higher supersaturation value, faster growth by condensation, and then earlier growth by collection caused by the different fall velocities for the wide particle size spectrum that has been developed. Indeed, it has been observed that colloidal stability in clouds over a marine environment (very clean air) tends

to break down earlier than that present on clouds developed over a continental environment (dirtier air). However, the mechanisms are not so simple; one might indeed expect that in air extremely rich in aerosols (natural or anthropogenic) such high competition for vapor would be generated that growth beyond a certain size would be inhibited, but this does not occur [26].

3.2.1 Particle activation

The phenomenon of activation is crucial to understanding how particles act as condensation nuclei and determine the starting microstructure in clouds. It is important to distinguish particles that are said to be "activated" from those that are not. The activation process can be conceptualized in the same way as nucleation in the sense that a free energy barrier (referred to as the saturation ratio $S = e^{\left(\frac{\Delta G}{RT}\right)}$) must be overcome. However, it should not be confused with nucleation since the liquid phase is already created with deliquescency but instead delineates a change in trend from stable to unstable growth resulting from increasing ambient humidity. During activation, the particles grow by passing through the peak of Köhler functions and transform from fog droplets into cloud droplets [26]. The Köhler saturation ratio expression and a graph showing the activation process will follow.

$$S_K = 1 + \frac{A_K}{r_d} - \frac{B_K i N_s}{r_d^3}$$

where A_k and B_k are parameters slightly affected by temperature, i the van't Hoff factor, and N_s the solute content.

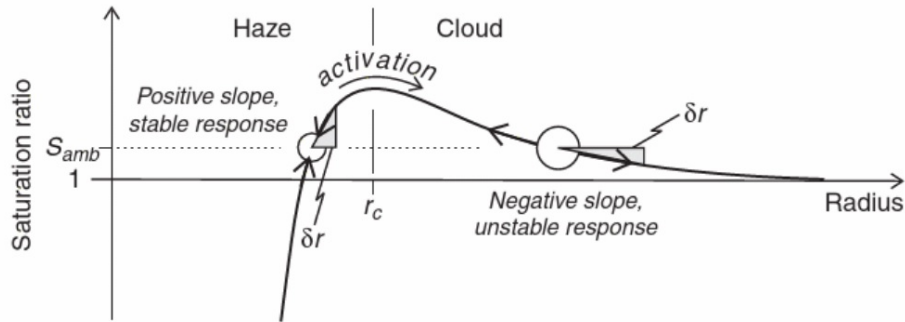


Figure 3.7: Activation process viewed through the Köhler equation. The abscissae shows the radius of the particles while the ordinates show the saturation of the environment. The process takes place in a supersaturated environment. *Image taken from: "Dennis Lamb and Johannes Verlinde. Physics and Chemistry of Clouds. Cambridge University Press, Cambridge, 2011" [26].*

What distinguishes them is the fact that the first one is on the stable side characterized by the positive first derivative while the second one (beyond r_c) has a negative slope and therefore presents an unstable response. Turns out that the most effective condensation nuclei are precisely those with lower critical saturation ratios. As the diameter of a particle increases, the critical supersaturation decreases. Within common clouds, supersaturation conditions of no more than 10 percent can be found, from which it is concluded that particles with a size greater than about $0.01\mu m$ are classifiable as CCNs. These, under favorable supersaturation conditions will be activated and become cloud droplets capable to grow, while the other smaller ones will remain inactivated fog droplets and lie in the region of space between the activated ones [26].

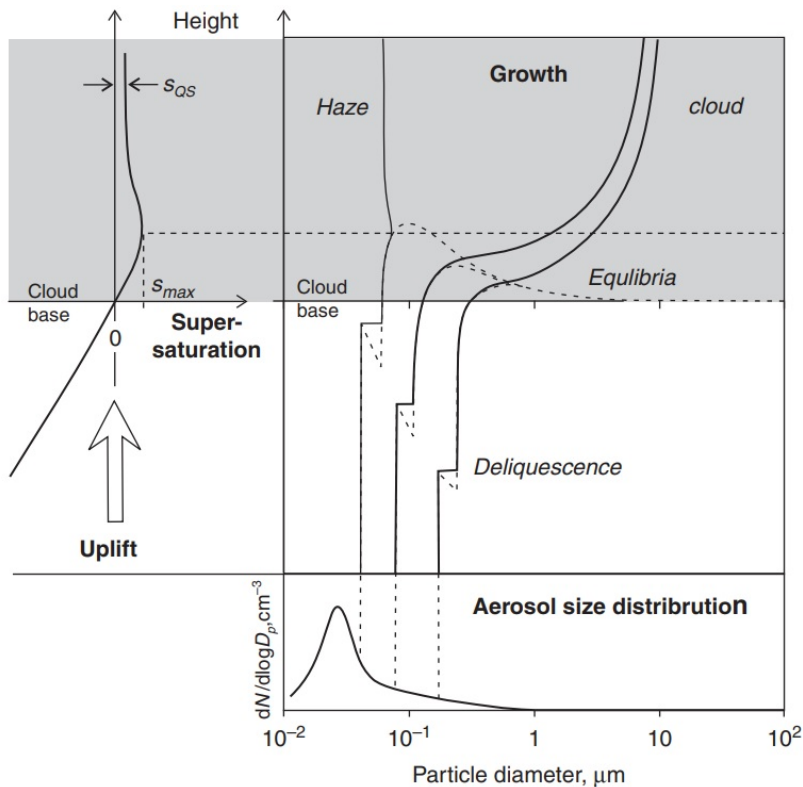


Figure 3.8: Droplet development within a typical cloud. On the left is shown the supersaturation trend considering a particle passing through the base of the cloud. On the right, the growth and eventual activation of three particles of different sizes is shown. *Image taken from: "Dennis Lamb and Johannes Verlinde. Physics and Chemistry of Clouds. Cambridge University Press, Cambridge, 2011" [26].*

The image summarizes what was explained above and illustrates qualitatively the evolution of ascending particles crossing the base of the cloud showing both the supersaturation trend and the eventual activation and growth of CCNs.

3.2.2 Relative motion

Considering the mechanisms by which droplets can grow it becomes clear that the presence of relative motion is of primary importance.

Two non-dimensional parameters, Stokes number and velocity ratio, can be used to evaluate the particle motion status [50]. The first is defined as follows:

$$St = \frac{\tau_p}{\tau_\eta}$$

where the numerator is the response time of a particle while the denominator consists in the characteristic time of the Kolmogorov scale η . If a particle is characterized by a $St \gg 1$ it means that it has a high inertia toward the flow and cannot follow its movement while if the $St \ll 1$ it behaves like a Lagrangian float meaning that it can faithfully follow the motion of the flow. The other parameter is defined as:

$$Sv = \frac{V_T}{v_\eta}$$

where V_T is the terminal velocity of droplets and v_η the Kolmogorov velocity scale. The droplets undergoing sedimentation move with relative motion respect to the flow; if it turns out $Sv \gg 1$ the interaction time between droplets and eddies will be almost zero while on the contrary for $Sv \ll 1$ it will be the phenomenon of sedimentation that can be neglected. For typical properties of droplets evolving into turbulent eddies in cumuliform clouds, $Sv \sim 1$ is observed, from which it can be concluded that sedimentation is not negligible [50].

3.2.3 Droplet distribution

It has been noticed that the ability of clouds to produce precipitation is closely related to the concentration of droplets in the cloud, thus to from the spectrum of CCNs and the maximum supersaturation value reached slightly above the cloud base; the properties of

absorbing and reflecting radiation are also affected [22]. The distribution of droplets and their size, and also the volumetric content of liquid water turn out to be quite inhomogeneous within clouds. They vary consistently not only between clouds of different genera or of the same ones at different stages of development, but also vary within a single cloud (both along height and on horizontal levels). Wanting to report numerical data, we have that within cumulus in early stages and stratiform clouds, water concentrations between 0.2 and $0.5 \frac{g}{m^3}$ are observed, but that can increase greatly to values of $3 - 5 \frac{g}{m^3}$ in fully developed cumulonimbuses. These types of measurements were carried out using aircraft equipped with appropriate meteorological equipment [40].

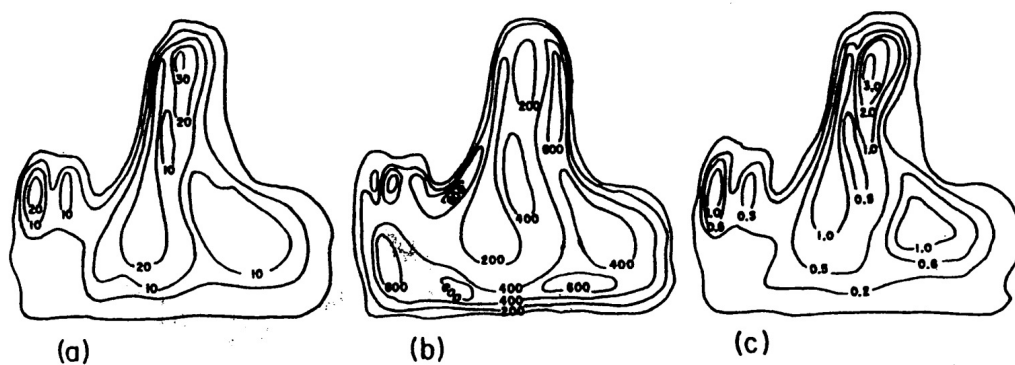


Figure 3.9: Spatial distribution of: (a) drop diameter [μm], (b) drop concentration [$\frac{n}{m^3}$], (c) water content [$\frac{g}{m^3}$]. Droplet size and water content are found to be higher at the upper part of the cloud while the concentration in number doesn't vary significantly with height. Image taken from: "Hans R Pruppacher and J. D Klett. *Microphysics of Clouds and Precipitation*. Springer Science + Business Media, Dordrecht, 2. aufl. edition, 2010" [40].

In the illustration above, it is possible to see the inhomogeneity in properties and distribution of droplets within a cumuliform cloud. It turns out to be clear that the mean size of the drops increases with height and with it also the concentration of water, which reaches a maximum in the upper part of the cloud. Regarding the concentration in numbers, on the other hand, it appears not to vary significantly with height while showing

slight maxima in the lower part where many small droplets are present. In addition, the variation in droplet properties can be observed on both the vertical and horizontal axes.

Regarding variability along the horizontal axis, similar observations can be made.

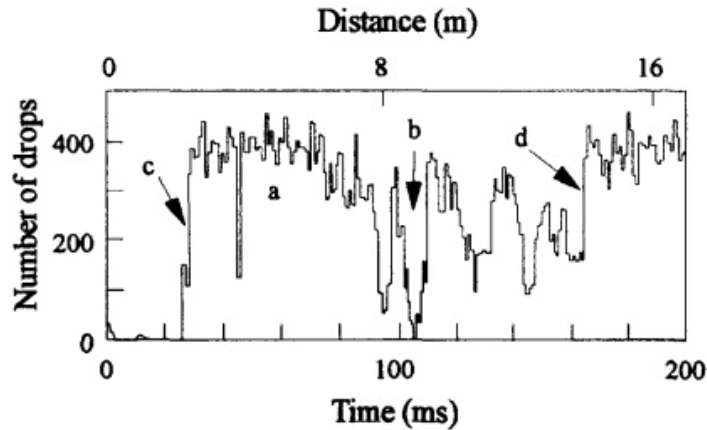


Figure 3.10: Droplet measurement made by sampling at 1000Hz during a flight within cumulus. It is possible to see the huge inhomogeneity present in the clouds, with peaks, uniform regions, and discontinuous areas. Image taken from: "P.R. Jonas. *Turbulence and cloud microphysics. Atmospheric research*, 40(2):283–306, 1996" [19].

In this case there are large variations in droplet distribution outside the zones of homogeneity as in section (a). There are even spots of discontinuity where the droplet count is close to zero within (b). Zones where there is a sudden change in concentration can be interpreted as discontinuities between the clean air and the cloud (c, d) [19].

3.3 Turbulence influence

Nowadays, it is well known that turbulence plays a fundamental role in the development of clouds and atmospheric phenomena, despite the fact that for a long time it was neglected as a field of research, particularly the small-scale one. Currently, there is a growth of interest

especially from researchers who work on turbulence, probably due to improved computer simulation performance and more accurate and punctual measurement capabilities [11]. Turbulence, however, affects both small and large scales, both growth by condensation and by collection. Through its fluctuations it can effectively move droplet-containing air masses to areas of different supersaturation, increasing or decreasing droplet growth. Fluctuations in the mutual velocities of nearby air masses will increase the chances of collision [4]. Several studies observe that turbulence accelerates droplet formation by coalescence following collision, this is because inside clouds turbulent motions can generate accelerations comparable with that of gravity and so influence the fall and relative motions between droplets [43]. For example, a simulation performed at high Reynolds number suggests that the accretion per collection of droplets with sizes larger than $10\mu m$ increases as collision efficiency increases between 25% and 40% [14].

3.3.1 Effect of entrainment

Several numerical simulations show similar results stating that the entrainment of clean air within a cloud and the subsequent mixing lead to a significant reduction in the liquid water content in a region of space ranging from a tens to several hundred meters from the cloud edge. These phenomena generate a very complex situation to analyze [38].

The mechanisms of turbulence and entrainment in particular have been shown and explained in the previous chapter, so now their effects on cloud dynamics will be shown.

A qualitative case of an interface between cloud and clean air is depicted in the image below. A time $t = 0$ is represented on the top, while a fully developed interface is illustrated on the bottom, where the dilution zone and the so-called humidity shell (where the liquid water content is close to zero and the humidity rises) can be observed.

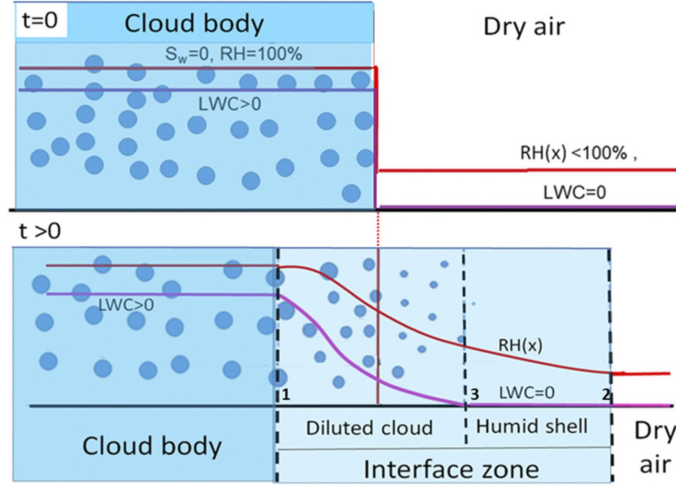


Figure 3.11: Representation of the interface between cloud and clean air. Above is shown a hypothetical initial instant with the two environments clearly separated while below is shown a following situation in which an interface zone has been generated where the humid shell and dilution region can be identified. *Image taken from: "Mark Pinsky and Alexander Khain. Theoretical analysis of the entrainment–mixing process at cloud boundaries. part i: Droplet size distributions and humidity within the interface zone. Journal of the Atmospheric Sciences, 75(6):2049 – 2064, 2018" [38].*

With the premise that these scenarios are not fully known, it is possible to say that the turbulent mixing that occurs at the boundary is an unsteady process that can lead to the accretion or dissipation of the cloud. Due to the non-stationarity of the entrainment-mixing phenomena, a situation of spatial homogeneity is not achieved, contrary to what one might think[38]. The process starts with the engulfment of clean air at the large scales and the nibbling at the smaller scales; vortices and filaments formed by clean and cloudy air that are still mostly separate and identifiable are generated; finally, a condition of homogeneity is reached by the time the motions reach the small scales and molecular diffusion also takes effect [12]. It can be deduced that one of the main consequences of entrainment is the reduction of water concentration, a factor that has much influence in droplet development. However, entrainment also influences the activation of CCNs: for

example, in the case of shallow cumulus it has been shown that through the swirling structures clean supersaturated air is able to enter the interior of the cloud increasing its supersaturation going to facilitate the activation of CCNs [6].

To better understand what the predominant effects are in an entrainment process, it is possible to evaluate the Damköhler number, formulated as follows:

$$Da = \frac{\tau_r}{\tau_s}$$

where the numerator represents the characteristic time of a vortex structure of radius r while instead the denominator represents the thermodynamic reaction time of the phenomenon being observed.

Having a $Da \gg 1$ implies that turbulent fluctuations will be much slower than thermodynamic reactions, which results in having that during the mixing of clean air and droplets some of the droplets will evaporate before a homogeneous condition can be achieved within the cloud. The number of droplets will go down resulting in the increase of supersaturation of the air that will favor the growth of the remaining ones. On the other hand, having a $Da \ll 1$ means that the velocity of turbulence is predominant and there is no decrease in droplets; slight evaporation will occur, which will decrease their diameter slightly. There is a broadening of the spectrum due to a decrease in air supersaturation [19].

3.3.2 Particle diffusion and Richardson approach

In a situation of calm or uniform motion, diffusion phenomena occur very slowly and have been extensively studied and described. When motions become turbulent, on the other hand, the situation is reversed; diffusion is much faster and able to act on much larger scales through the presence of eddies of different sizes. As mentioned in the previous paragraphs this process is called eddy-diffusion. The study of these phenomena is still

ongoing and not completely understood and described.

This topic is strictly related to the diffusion of particles in the atmosphere. One of the first scientists to investigate the problem of particle diffusion is Lewis Fry Richardson by now a century ago. In his studies it is stated that all attempts to extend models of molecular diffusion even making use of the superposition theorem of effects cannot represent reality because they would not be based on the typical phenomena of turbulence. The key idea of his work is that the rate of diffusion rises as the distance between the particles increases; for example, if two particles are at such a distance that they are involved in two different gusts they will be drawn into different motions going to increase more the speed with which they move apart [42].

To study the phenomenon of particle diffusion Richardson decided to follow a statistical approach. Suppose we consider a region containing a number N of marked molecules that we will denote with the letters of the alphabet. Let us take one and assume that its position corresponds with the origin of our graph. Let us now divide the study domain into a series of lines positioned at a distance equal to a positive or negative multiple of h . This will generate cells of size $h \times h$. The h interval should be chosen so that a sufficient number of molecules are present in each one. For each instant of time we are going to count the number of molecules marked present in each cell and we will repeat all this process for every marked molecule. In this way we are now able to calculate the following mean

$$Q_{n,n+1} = \frac{1}{N}(A_{n,n+1} + B_{n,n+1} + C_{n,n+1} + \text{etc... to } N \text{ terms})$$

and obtain the quantities $Q_{0,h}$, $Q_{h,2h}$, $Q_{2h,3h}$ etc... representing the number of marked molecules per length, categorized on the basis of distances h from other molecules. Calculated these quantities, it is possible to draw the so-called distance-neighbour graph [42].

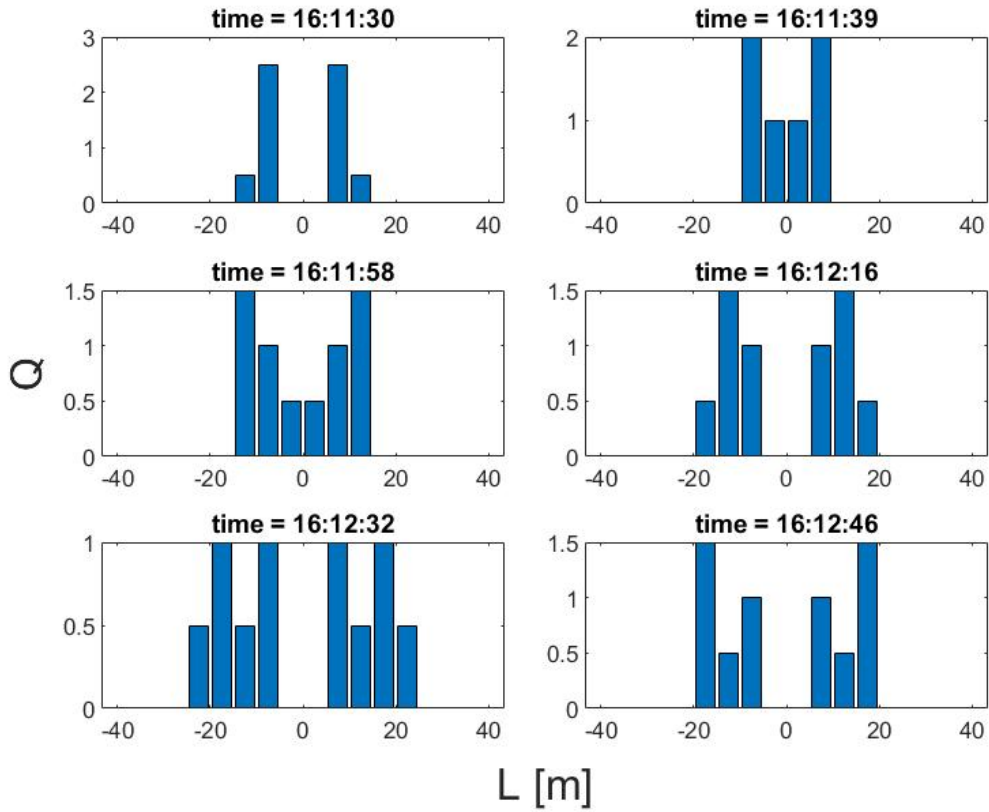


Figure 3.12: Example of a distance-neighbour graph representing a case of constrained diffusion. More specifically, the evolution of 4 helium-filled balloons tied to the ground by a thread is shown. The distance parameter h was chosen as $h = 5m$.

In the graphs above, an example of constrained dispersion of 4 particles using distance-neighbor graphs is shown. The data were collected during an experiment held on 10/02/22 using 4 helium-filled balloons tethered to the ground. Each graph represents an instant of time. It can be seen that at the "zero" instant, the particles are all clustered and thus are at mutual distances between $1 - 2h$, while in the later graphs they are at higher reciprocal distances. As the diffusion process proceeds, it will be possible to see the distribution widening, while still maintaining peaks. Since the diffusion is not free, the distribution will

remain confined within certain values. It can be seen that the relative distance to each other shows symmetry around the origin, since each relative distance between two particles is counted twice, once positive and once negative.

Another property we observe is that during evolution the area subtended between the Q curve and the abscissa (which we will now call l) remains constant; N had also been considered constant by assumption. This suggests that Q should respect a differential equation of the type:

$$\frac{d Q}{d t} = \frac{d}{d l}$$

and so:

$$\int_{-\infty}^{\infty} \frac{d Q}{d t} d l = 0.$$

Chapter 4

Radiosondes

As explained in previous sections, cloud dynamics includes highly complex phenomena such as those related to turbulence and mixing that are not yet fully understood. All this goes to constitute a still open challenge in the fields of meteorological modeling and pure knowledge of the phenomena. In order to better understand what is happening in the real world, it is useful to set up a data collection campaign, consisting of balloons and radio probes that will follow small-scale turbulence outside and inside clouds in a Lagrangian manner, collecting various thermodynamic parameters as well as position and velocity and acceleration data [35]. Other methods of investigation for these phenomena include remote sensing with radar and lidar [9] [18], in situ observations with manned and unmanned aerial platforms (airplanes, helicopters, tethered lift systems, etc.) [45] [27] [30], laboratory experiments in wind tunnels and climate chambers [17] [44] [8], and numerical simulation experiments conducted through direct Navier-Stokes numerical simulation of small portions of clouds [23] [24].

In the field of research balloons, the radio probes under study result to be categorizable as mini ultralight instrumented weather balloons. They turn out, however, to be quite dif-

ferent from other instrumented systems developed for atmospheric sounding, such as the NCAR-NOAA Global Hawk tethered dropsonde (weight 167 g, length 30.5 cm, diameter 4.6 cm; square cone-shaped parachute of 20 cm side) used for vertical atmospheric profile measurements (they are not following Lagrangian trajectories) and launched from a National Aeronautics and Space Administration (NASA) unmanned aircraft [51], or NOAA's ground-launched smart balloon (335-cm diameter) that houses the sensors inside the balloon itself and is used for Lagrangian experimental hurricane research [33]. Other systems used include a short-range weather balloon launched from the ground by NOAA carrying a tethered radiosonde (balloon diameter about 152 cm) [13], and a balloon-tethered microprobe released into the air (total weight 65.6 g) for supercell thunderstorm studies [46].

The idea of starting a project based on the use of small radiosondes carried in the air by biodegradable helium-filled balloons was developed during the writing of a proposal for a European Horizon 2020 Marie Skłodowska Curie project, approved in 2016 (H2020 MSCA ITN ETN COMPLETE, GA 675675: Innovative Training Network on Cloud-MicroPhysics-Turbulence-Telemetry [10]). The aim is to achieve lightweight, compact systems with a target weight of 20g and radius of 15cm; with the ability to float at altitudes up to 2 kilometers and to send data to the ground for at least one hour [35].

It is possible to see the Lagrangian balloons under discussion as fluid particles equipped with instruments that incorporate an assortment of compact-sized sensors for measuring local fluctuations in temperature, pressure, humidity, acceleration and trajectory. In the future, following further development they may be released into the atmosphere by unmanned aerial vehicles or small aircraft in addition to people on the ground [35]. These balloons could be used over different types of environments, from oceanic (still for the study of local small-scale fluctuations) to continental and alpine environments.

4.1 Requirements and operating environment

As mentioned earlier the environment we want to go to study is that involving clouds and their interfaces with clear air, particularly for thermal-convective clouds. These clouds, generated due to the thermal gradient between hot air masses near the ground and cold air masses at high altitude, are typical of the spring and summer months, whether over alpine or hilly terrain as well as over extended plains [35]. The turbulence that characterizes these phenomena turns out to be shearless and very frayed. The interaction zone between the saturated (cloud) and subsaturated (clean air) zones appears to have an intermittent and strongly anisotropic character [35].

These radiosondes left free to float (not tethered), have the purpose of measuring eddies with dimension not less than $0.5 - 1m$ characterized by a maximum frequency equal to $0.5 - 1Hz$ and kinetic energy per unit mass between $0.001 - 0.01(\frac{m}{s})^2$. The upper limit instead corresponds to a size of the eddies of about a few kilometers characterized by frequencies as low as $10^{-4}Hz$. Each radiosonde must have a series of sensors capable of measuring pressure, temperature, humidity, velocity, acceleration and vorticity during their activity inside warm clouds [35].

Type of requirement	Required range
External temperature	0 — +30 °C
External relative Humidity (RH)	0 — 100%
External pressure	400 — 1100 mbar
Trajectory accuracy	± 100 mm
Air-flow fluctuation	5 — 6 m/s

Figure 4.1: Operational requirements of the radiosondes [35].

Knowing the environmental conditions that will actually be found inside the warm clouds, it was possible to list the operational requirements of the radiosondes in the table above.

Meanwhile our devices are gathering data, they also have to be able to send them to a receiver radio-station on the ground. To achieve that, it is fundamental to have a low power consuming transmission technology that can reach sufficiently long distances [35].

4.2 Radiosondes design and system architecture

It is possible to divide the system in three main part:

- **balloon-radiosonde system**, this part performs the task of collecting data appropriately and sending them correctly to the ground;
- **base stations**, having the task of receiving, storing and transmitting incoming data to the processing machine;
- **processing machine**, used for database management, filtering operations, visualizations, and other operations [35].

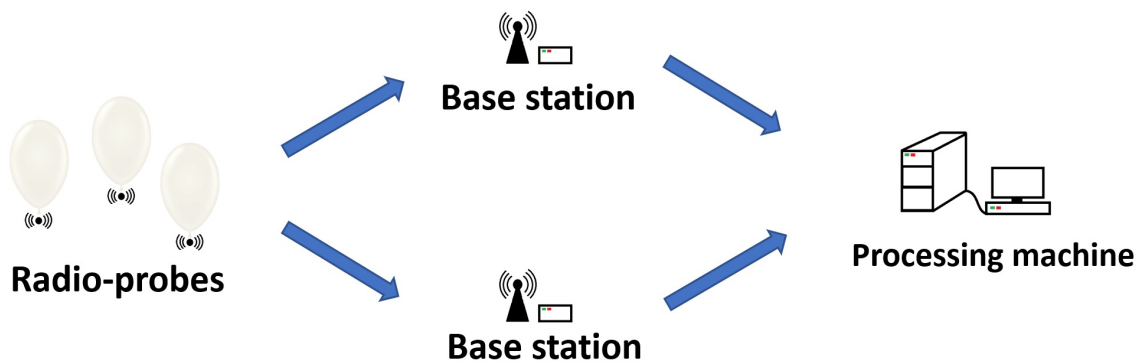


Figure 4.2: System architecture of wireless sensor network (WSN). The information transmitted by the probes will be collected by ground stations and then sent to a processing machine.

A block diagram representing the parts and their connections of the PCB is shown in the figure below:

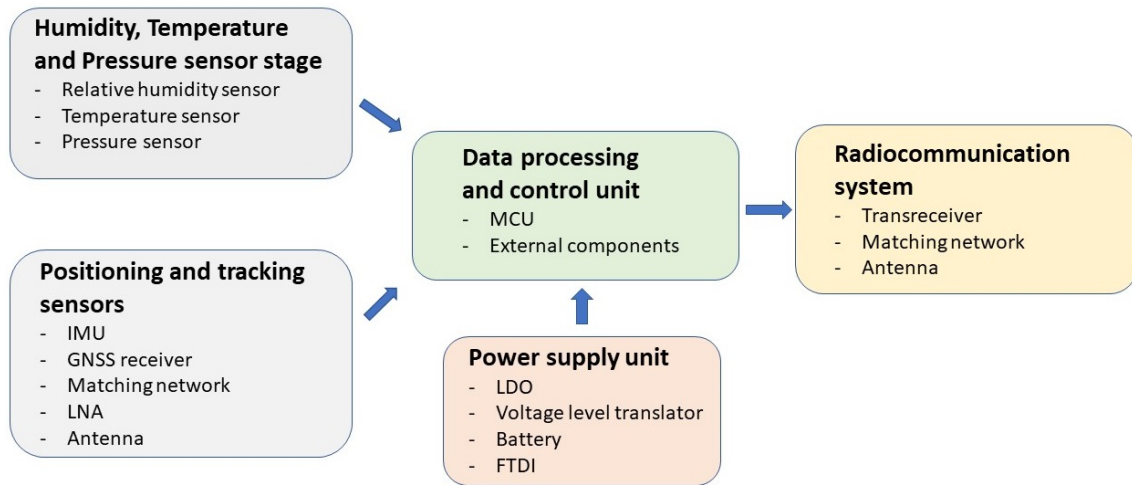


Figure 4.3: PCB internal structure: the block diagram shows the interconnections between the various radioprobe modules.

Regarding the PCB, it is assembled on both sides of a FR4 double-layer substrate with components mounted via surface-mount-technology (SMD) [35].

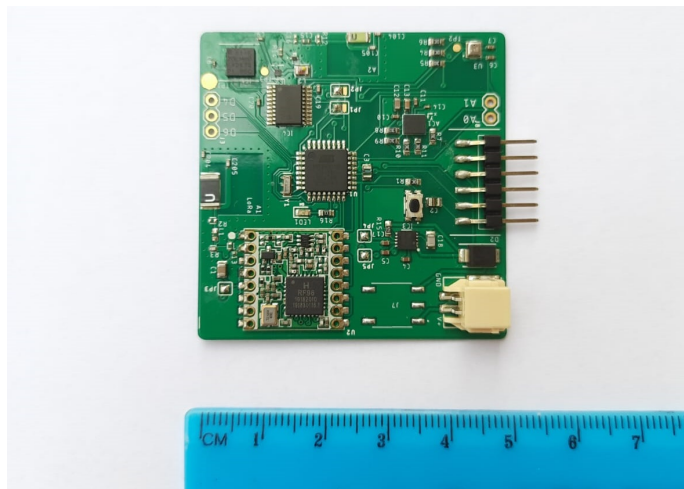


Figure 4.4: Photo of the printed circuit board with the modules mounted.

The table below shows the physical dimensions of the PCB:

Property	Value
Length	50 mm
Width	50 mm
Thickness	0.8 mm
Weight	7 g

Figure 4.5: Table showing the physical dimension of the PCB.

A brief description of the various modules implemented in the PCB follows [35].

- Data-Processing and Control Unit.** This unit is the calculation module of the radiosonde and allows several processes to be performed in an automated way. Incoming data from the sensors are processed, saved and sent to the transmission module to send to the ground station. An ATmega328 8-bit [2] low-power complementary metal oxide semiconductor (CMOS) on-board microcontroller from Microchip was chosen. Its dimensions are $9\text{mm} \times 9\text{mm} \times 1\text{mm}$ and its weight is 70mg . The microcontroller requires a voltage between 1.8V and 5.5V and has an operating temperature range of -40°C to $+85^{\circ}\text{C}$. It is characterized by low current consumption: 0.2mA in active mode, $0.1\mu\text{A}$ in power-down mode, and $0.75\mu\text{A}$ in power-save mode.
- Radio Communication System.** This module enables one-way communication with the ground station via LoRa-type communication. This module, RFM95 from HopeRF [16], requires a voltage between 1.8V and 3.7V and has an operating temperature range of -20°C to $+70^{\circ}\text{C}$. The transceiver is characterized by a current consumption of $0.2\mu\text{A}$ in sleep mode, $1.5\mu\text{A}$ in idle mode, 20mA in transmit mode at $+7\text{dBm}$ output power (OP), 29mA in transmit mode at $+13\text{dBm}$ OP, and 120mA in transmit mode at $+20\text{dBm}$ OP.

- **Antennas.** Each radiosonde has two RF stages, one to send information to the ground and the other to receive timing and position from the satellites. The antennas used for the two stages are quarter-wave ceramic antennas integrated into the system, one operating in the sub-1GHz LoRa frequency band and the other in the L1 frequency band, respectively. Both antennas are linearly polarized and small in size, $5mm \times 3mm \times 0.5mm$ and $3.2mm \times 1.6mm \times 0.5mm$, respectively. They were mounted in the center of two different PCB edges.
- **Temperature, Barometric Pressure, and Relative-Humidity Measurement.** An all-in-one type of sensor was used for this block, the BME280 combined module [5], which consists of a humidity sensor that measures ambient temperature, relative humidity, and barometric pressure. This module has a really low power consumption, in the range of μA . This feature makes it ideal for use with a battery as a power source. The device comes in a land grid array (LGA) package of dimensions $2.5mm \times 2.5mm \times 0.93mm$ and requires a voltage between $1.2V$ and $3.6V$. The operating ranges of the module are 0 to 100% RH for relative humidity, 300 to $1100hPa$ for pressure, and -40 to $+85^{\circ}C$ for temperature.
- **Positioning and Tracking Measurement.** This block is necessary to obtain the data that will be used to determine the position and trajectory of the radiosondes during flight. The IMU can obtain orientation, force and angular velocity information. The module LSM9DS1 [28] used consists of a three-axis digital linear acceleration sensor, a three-axis digital angular velocity sensor, and a three-axis digital magnetic sensor, all in the same unit. The module has the following dimensions: $3.5mm \times 3mm \times 1mm$. It requires a voltage between $1.9V$ and $3.6V$ and has an operating temperature range between $-40^{\circ}C$ and $+85^{\circ}C$. The GNSS receiver module used is of the professional type, super-low-power system-in-package (SiP) ZOE-M8B

[47]. The module has the following dimensions: $4.5\text{mm} \times 4.5\text{mm} \times 1\text{mm}$ It requires a voltage of 1.71V to 1.89V and has an operating temperature range of -40°C to $+85^\circ\text{C}$.

- **Power Supplay Unit.** One of the most critical aspects of radiosondes is power consumption because as power consumption increases, the energy required for operation and therefore also the weight of the battery increases considerably. There are two possibilities. The first and the use of an lithium metal oxide (LMO) battery with a nominal capacity of 125mAh , a volume of 3.2cm^3 , a weight of 9g and an operating temperature range of -55°C to $+85^\circ\text{C}$. The second alternative is a USB-type connection, which is mainly used to upload code. To provide the required voltages (1.8V and 3.3V) an low-dropout (LDO) voltage regulator is built into the circuit.

Further modules specifications is shown in the table below.

Device code	Property	Sample rate	Range
BME280	Humidity	1 Hz	0 % — 100 %
BME280	Pressure	1 Hz	300 — 1100 hPa
BME280	Temperature	1 Hz	-40°C — $+85^\circ\text{C}$
LSM9DS1	Acceleration	10 — 952 Hz	$\pm 16\text{ g}$
LSM9DS1	Angular velocity	14.9 — 952 Hz	$\pm 2000\text{ dps}$
LSM9DS1	Magnetic field	0.625 — 80 Hz	$\pm 16\text{ Gauss}$
ZOE-M8B	Longitude	4 — 10 Hz	$\pm 180^\circ$
ZOE-M8B	Latitude	4 — 10 Hz	$\pm 90^\circ$
ZOE-M8B	Altitude	4 — 10 Hz	0 — 50 km
ZOE-M8B	Velocity	4 — 10 Hz	$\pm 500\text{ m/s}$

Figure 4.6: Sensors specifications [35] [5] [28] [47].

Chapter 5

Aerostatical balloons

The development of proper balloons is of crucial importance to the success of data collection experiments. They will have to make the radio-probe follow the movements of fluid particles in and out of clouds in a Lagrangian manner. They will have to float on an isopycnic, that is, a "level" characterized by constant density. The balloons will have to carry the radio probes in a stable manner and making as little disturbance to the environment as possible. To achieve this, a balloon with the most spherical shape possible will be developed. Once data collection is finished, the balloon will continue to fly until it crashes to the ground. It will then have to be made of biodegradable material to minimize its impact on the environment as much as possible.

The following sections will discuss the choice of material, sizing and assembly of the balloons.

5.1 Materials

The material to be used must possess certain properties, in particular it has to be [3]:

- biodegradable
- cheap
- not too elastic
- impermeable to helium
- hydrophobic

The material must be biodegradable because the balloons will be left to float in the atmosphere and then fall back to the ground at the end of data collection; thus, their environmental impact is reduced; In addition, it must be inexpensive and easy to find because several balloons must be made. The material should be minimally elastic, as it is important that the volume of the balloons does not change with variations in atmospheric pressure. It must, of course, be impermeable to helium so that there is no leakage and thus no loss of lift. Hydrophobicity is important because this way when flying inside the clouds the droplets do not tend to adhere to the surface putting weight on the balloon. This property can also be achieved by applying special coatings directly to the balloon; it should be kept in mind that this will also increase its weight [3].

In case the sensors were placed inside the balloon, it should also have the property of having a low heat capacity so as not to distort the temperature measurements. However, in both the last experiment and the next one, the radiosonde was placed outside in order to have more accurate measurements. In particular, we get the elimination of the thermal inertia of the balloon and the helium in it and the ability to measure the relative humidity of the outside air, which would not be possible with sensors placed inside. In the future, an internal radiosonde could be considered (better weight distribution and stability) with the sensors placed on the outside of the balloon. This would also eliminate the influence

of heat developed by the battery and electronics during operation. In the current version, in order to reduce the influence of heat produced, it was decided to separate the battery from the printed circuit board (PCB) by a sponge insulation element.

After some laboratory tests, some valid materials were indentified: Latex, Myral, Polylactic Acid (PLA) and Mater-Bi [3].

To evaluate hydrophobicity, the contact angle of a $5\mu\text{l}$ drop of water deposited on the surface of the sheet was derived. This angle is identified by the direction of the solid-liquid tension and one of the liquid-gas tension, tangent to the outer surface of the droplet; the vertex corresponds to the three-phase liquid-solid-gas point. [3]

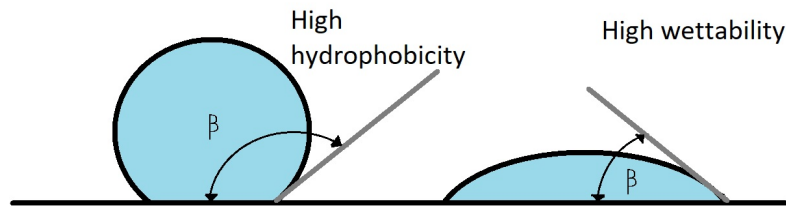


Figure 5.1: Contact angle of a drop on a solid material.

To estimate helium permeability, balloons composed of different materials were inflated with helium and placed on a balance; the rate at which the balloons weight rises is directly related to the amount of helium loss [3].

As a result of the evaluation of all these characteristics, it was decided to opt for Mater-Bi, which turns out to have good characteristics of strength, hydrophobicity, and helium impermeability in addition to being biodegradable, inexpensive, and easily findable in bag form.

5.2 Physics

Before we begin discussing balloon sizing and performance, it is useful to recall the basic laws governing aerostatic balloon physics. The phenomenon of buoyancy is described by Archimedes' famous principle, proposed in 246 BC. It states that:

"every body immersed in a fluid is subjected to a force directed from bottom to top of an intensity equal to the force-weight of the fluid displaced".

In a more mathematical way, the above statement translates to:

$$T_h = Vg(\rho_f - \rho_o)$$

where T_h is the hydrostatic thrust, V is the volume, g is the gravitational acceleration, and in the parenthesis we have the difference between the density of the fluid and that of the object.

Returning to the topic of balloons, knowing this law, we want to use it to figure out the correct size of balloons to achieve proper buoyancy at a fixed altitude. In other words, we need to match the total force-weight of the probes with the hydrostatic lift.

$$T_h = W_t = M_t g$$

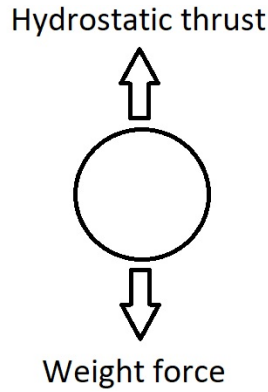


Figure 5.2: Representation of the forces acting on the balloon: balance between gravity and hydrostatic thrust.

By manipulating the above formulas, an expression for the volume under equilibrium conditions can be obtained. It is elementary to derive:

$$V = \frac{M_t}{\rho_{air} - \rho_{he}}$$

Considering the perfect gas law:

$$\rho = \frac{pM}{RT}$$

it is possible to express the volume as a function of air density and the quotient between the molecular weights of helium and air:

$$V = \frac{M_t}{\rho_{air} \left(1 - \frac{M_{he}}{M_{air}}\right)}$$

where we assume that the molecular weight of air is approximated to that of dry air $M_{air} = 28.96$ and that of helium is $M_{he} = 4.003$. Once the mass of our probe is fixed, the only variable in this equation is the density of the air, which will tend to vary significantly

with altitude. The change in thermodynamic properties of the atmosphere with altitude can be described by ICAO standards, shown in the table below.

<i>Altitude [m]</i>	<i>Pressure [10^4 Pa]</i>	<i>Temperature [K]</i>	<i>Density [Kg/m^3]</i>
0	10.0	288	1.225
250	9.8	286	1.196
500	9.5	285	1.167
750	9.3	283	1.139
1000	9.0	282	1.112
1250	8.7	280	1.084
1500	8.5	278	1.058
1750	8.2	276	1.032
2000	7.9	275	1.006
2250	7.7	273	0.981
2500	7.5	272	0.956
2750	7.2	270	0.933
3000	7.0	269	0.909

Figure 5.3: Variation of air properties with altitude. The table shows the values of the ICAO standard atmosphere.

At this point, it is possible to write a simple script in MatLab that can calculate the volume of helium needed to float a probe with a fixed weight to a certain desired altitude. Considering, for example, a probe weighing 20 grams, with the above data and formulas, the following graph can be obtained:

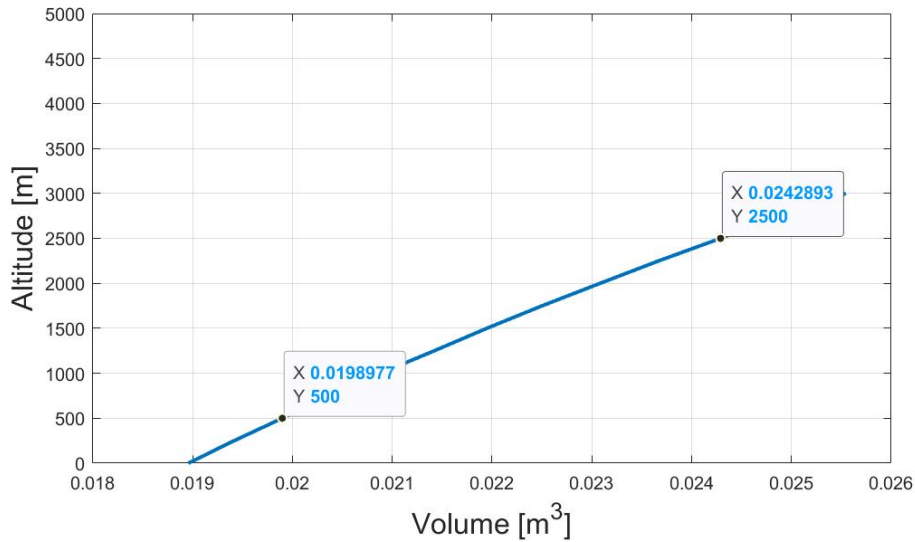


Figure 5.4: Example of the relationship between helium volume and buoyancy altitude for a probe-balloon with a fixed weight of 20g. It can be seen that to increase the buoyancy altitude from 500m to 2500m the volume must be increased by about 20%.

It is therefore clear that atmospheric density variation plays a decisive role in balloon sizing. Indeed, in the above graph, it can be seen that given a fixed-weight probe (20 grams), the volume required to float the probe at 2500 meters instead of 500 must be increased by 20%. The calculation of buoyancy altitude in a real case turns out to be very complex. If we are using industrially produced latex or rubber balloons we will have that they will be standardized in size, but, as the material is flexible it is possible that their volume will vary as atmospheric pressure and temperature change. In the case of the balloons made of Mater-Bi the volume turns out to be fixed since the material's minimal elasticity, however, with hand production it is difficult to control the accuracy and follow a standard; the buoyancy rate turns out to be susceptible to even small variations in volume.

The next section will explain the balloons sizing process in detail.

5.3 Sizing

As explained earlier, the correct sizing of a balloon is a fundamentally important part. To begin the process, it is convenient to analyze commercially available material. A sheet of Mater-bi obtained from a waste bag purchased from a popular chain store in Turin, turned out to be suitable for our purpose. It is necessary to weigh the material to obtain its specific weight per unit area, which turned out to be $21 \frac{g}{m^2}$. At this point, assuming that we consider the balloons to be perfectly spherical in shape, it is already possible to estimate the weight of the balloons based on the volume (and thus surface area and radius) realized. The graphs that will follow in the chapter were all made using MatLab software.

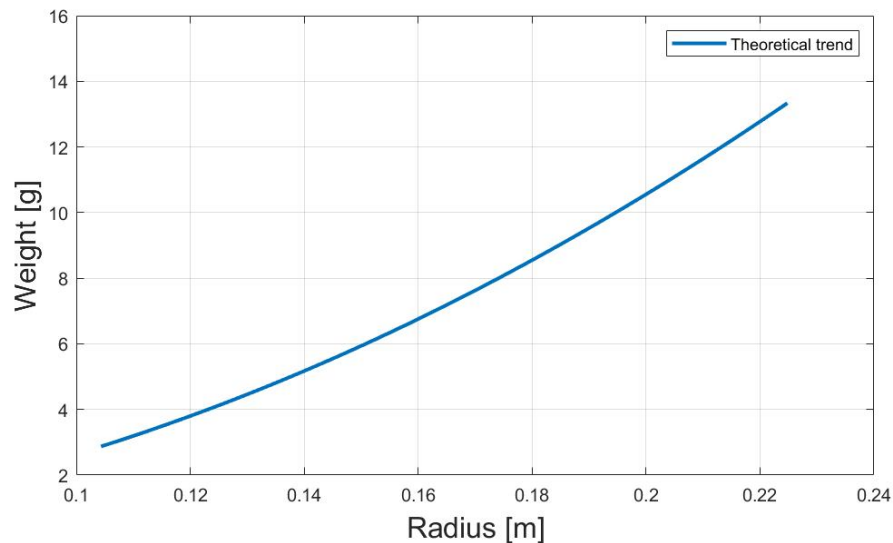


Figure 5.5: Balloon weight trend based on the assumption of spherical geometry and specific weight of material equal to $21 \frac{g}{m^2}$.

Once the weight has been determined, using the formulas shown in the previous chapter, the net transportable load can be calculated by subtracting the weight-force of the balloon from the aerostatic thrust generated. In this way, the following graph is obtained:

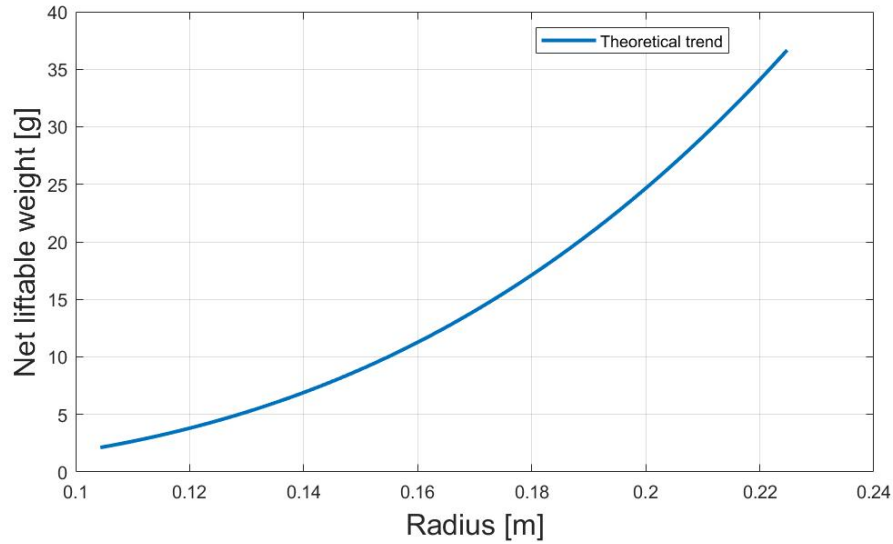


Figure 5.6: Trend of net transportable weight (buoyancy) as the size of the mater-bi balloon changes. Assumptions were spherical geometry and density at sea level.

Knowing these trends, it is now possible to size our balloons. A comparison with experimental data will be shown at the end of the paragraph in order to validate the theoretical calculations.

As a first step, the total weight that has to be carried must be determined:

Part	Weight
PCB	7.5 g
Battery, sponge and thread	10 g
Total	17.5 g

Figure 5.7: Weights of probe parts.

Since the PCB will be mounted externally to the balloon, there will be no need for any additional structure. At this point it becomes possible to choose the size of the balloon; it was decided to make a balloon capable of carrying about 25 grams, so that it would have some tolerance and to allow it to reach a sufficiently high altitude.

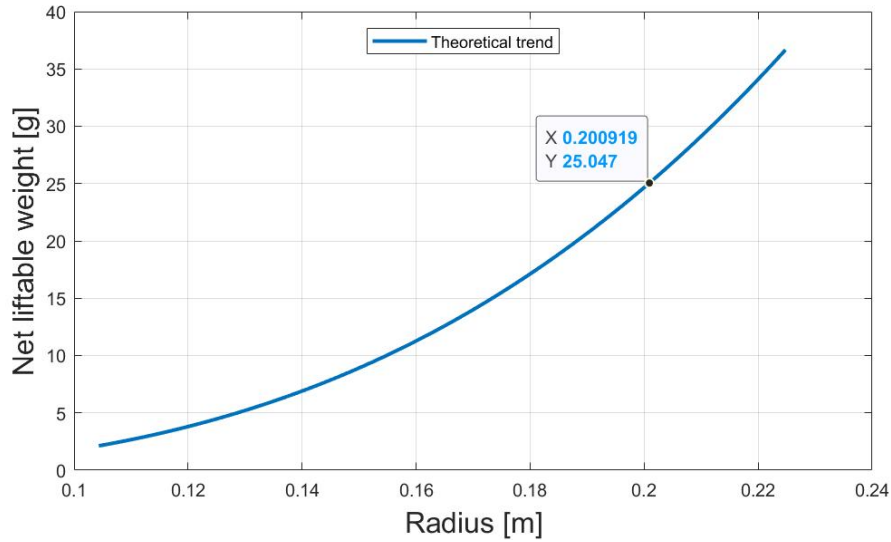
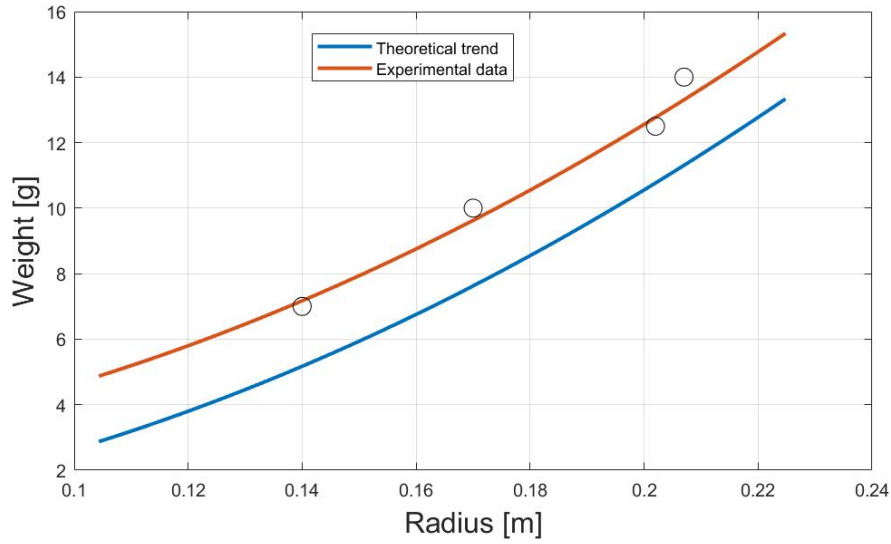


Figure 5.8: Size chosen to produce the balloons for the 3/11/22 experiment: 25g of liftable weight (buoyancy) at sea level corresponding to a radius of 0.20m.

Returning to the graph previously plotted, we obtain that to have a net lift of about 25 grams we will need to make a ballon with a radius of about 20 centimeters. This will be the dimension that will be used.

5.3.1 Comparison with experimental results

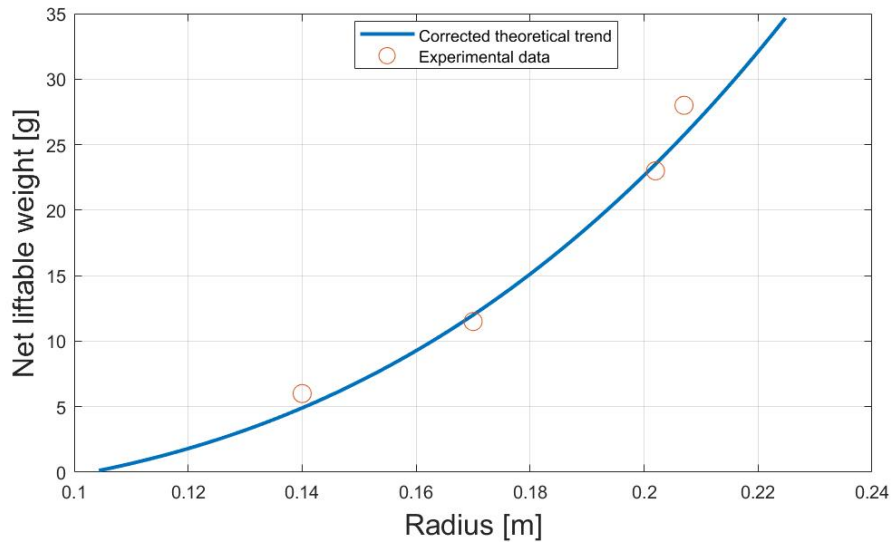
This section will show the experimental results obtained and compare them with the theoretical trends calculated in the previous paragraphs. The first graph shows the comparison of the weights obtained with those calculated:



Radius	Weight
14.0 cm	7 g
17.0 cm	10 g
20.2 cm	12.5 g
20.7cm	14 g

Figure 5.9: Comparison of balloon weights measured in the laboratory and the previously developed theoretical trend. The measurement uncertainties are as follows: radius measurement ± 0.5 cm; weight measurement ± 1 g. The difference between the two trends can be explained because there is more material in the balloons than in the ideal sphere.

It is possible to see that there is some distance between the theoretical trend and the experimental data. This can be explained by knowing that there is extra material in each balloon compared to the ideal sphere to allow for welding and to make the part underneath that permits its inflation and connection with the probe.



Radius	Liftable weight
14.0 cm	6.0 g
17.0 cm	11.5 g
20.2 cm	23.0 g
20.7cm	28.0 g

Figure 5.10: Comparison of lifting capacity (buoyancy) measured on balloons in the laboratory (250m altitude) and that assumed. The measurement uncertainties are as follows: radius measurement ± 0.5 cm; liftable weight measurement ± 0.1 g.

A comparison of net lifting capacity is shown in this graph. It can be seen that, in this case, there is a very good correlation between the theoretical and experimental data; the trend of corrected weights shown above was used to calculate the net lift capacity.

At this point it is useful to summarize the process by listing in a table the characteristics of the balloons that will be made:

Property	Measured value
Sea level lifting capacity	23.0 g
Volume	0.0345 m ³
Radius	0.202 m
Balloon weight	12.5 g
PCB weight	17.5 g
Total weight	30 g
Predicted buoyancy altitude	2000 – 2500 m

Figure 5.11: Measured properties of balloons for the experiment.

These are the experimental quantities measured on a real balloon. It can be seen that some data are discordant from those assumed or chosen in the previous paragraph. This is because some assumptions were not very precise, such as the one about the weight of the balloons and the one about assuming an ideal sphere. Also it must be remembered that balloons are made by hand, from which it follows that they cannot be made precisely, and there is always an uncertainty given by the human factor.

5.4 PAWAN balloon testing

Ten radiosondes were launched in the experiment carried out on 3/11/22, but it is expected that in future experiments this number will be increased to try to have many more measurement points, which are essential for obtaining good statistics. The manual production of a balloon takes a long time, up to 4 hours; so the process becomes unsustainable for the production of large numbers. Another problem is the inevitable dimensional difference that hand-produced balloons have from each other. For these reasons, the purchase of industrially produced balloons is being considered in order to achieve time savings and standardization of all balloons: those mass-produced industrially will all be identical to a

good approximation. A further advantage is the near-perfect sphericity of the balloon once inflated.



Figure 5.12: PAWAN balloon inflated and ready for testing.

The balloon is produced by an Indian company, PAWAN, from which orders can be made. In this case it was possible to find different sized samples to be tested. The table below shows the characteristics of the tested balloon. The tests were carried out on the smallest balloon of those obtained since it was more in line with the required dimensions of the radiosondes in use. The balloon is made of an elastic material, which, unlike Mater-Bi allows the volume to be varied as desired.

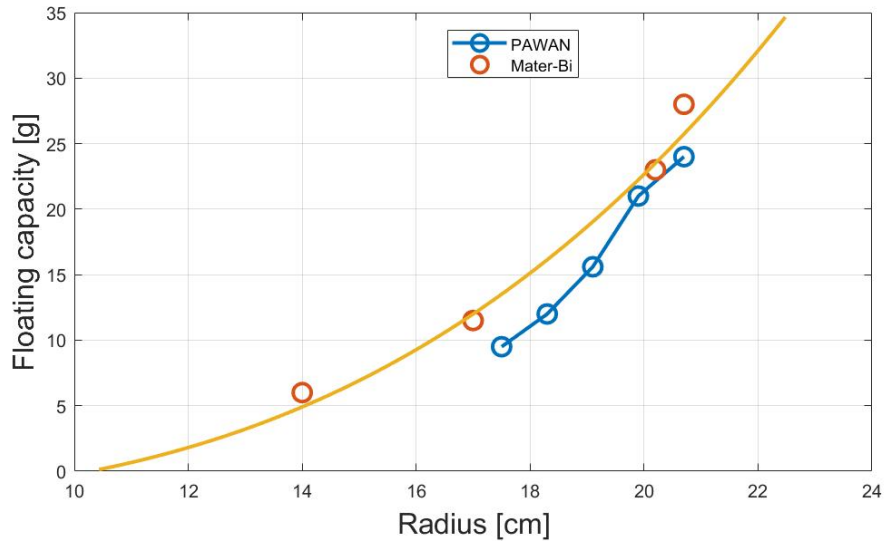
Pawan specification	
Material	Natural rubber
Weight	10 g
Bursting Radius	22.5 cm

Figure 5.13: the table above shows the main characteristics of the balloon.

The company claims that the balloons are biodegradable, however, this property will have to be tested at PoliTo by experts in materials chemistry. Tests conducted in the laboratory are designed to measure performance as carrying capacity in relation to geo-

metric dimensions. The balloon was inflated to a proper size; then the weight it was able to sustain at that size was evaluated. After slightly deflating it and then slightly reducing its volume, the same operation was carried out and so on for different sizes.

A graph showing the results of the test is now presented.



Mater-Bi	
Radius	Floating capacity
14.0 cm	6.0 g
17.0 cm	11.5 g
20.2 cm	23.0 g
20.7 cm	28.0 g

Pawan	
Radius	Floating capacity
17.5 cm	9.5 g
18.3 cm	12 g
19.1 cm	15.6 g
19.9 cm	21.0 g
20.7 cm	24.0 g

Figure 5.14: graph showing the performance comparison between Mater-Bi and PAWAN balloons. Measurements were conducted at Politecnico di Torino, at an altitude of about 250m. The measurement uncertainties are as follows: radius measurement ± 0.5 cm; floating capacity measurement ± 0.1 g.

In the graph just above, a comparison between the assembled balloons made of Mater-Bi

and those produced by PAWAN in natural rubber is shown. As can be seen, net of an error of less than a centimeter (the radius measurements were derived from the circumference measurement: small errors are due to the fact that the surface of the balloon is deformable and shrinks during measurement) in the range of 15 to 25 grams of transportable weight the dimensions of the two balloons are comparable. The reason why the Mater-bi balloons turn out to be slightly better in performance probably lies in the fact that for a given circumference size its actual volume will be slightly larger than that of an equivalent ideal sphere; this is due to the non-perfect geometry of the balloon. Observing the behavior for smaller radii, it is possible to detect a distancing of the two curves: this trend is due to the fact that while the weight of the PAWAN balloon is fixed, that of the balloons that can be made of Mater-Bi varies as a function of volume, dropping below 10 grams in sizes smaller than 0.175 meters in radius.

It can be concluded that in the case where it is necessary to carry between 15 and 25 grams of weight the performance given by the two balloons is comparable; however, the advantage given by the PAWAN balloons cannot be ignored, which being made of elastic material allow to obtain the desired volume with precision. On the other hand, in the case where the weight to be lifted varies between 5 and 15 grams, the balloons that can be made of Mater-Bi offer higher performance because their weight is optimized for the size used. This leads to smaller dimensions for the same transportable weight.

5.5 Assembly

This section will explain the procedure for assembling balloons and show the tools used. The work is completely manual and requires a great amount of patience and precision since the material used is very fragile and consequently very damageable.

The materials and tools used are:

- waste bags made of Mater-Bi with a thickness of about $30\mu\text{m}$, available in common stores;
- template for cutting out shapes;
- surgical scalpel used to precisely cut out the shapes;
- markers, paper yardstick, ruler and scissors for multiple uses;
- a hand wheel sealer used to make welds having the heated wheel coated with a Teflon tape to prevent it from sticking to the material;
- a silicone placemat on which to make the soldering joints;
- a tank filled with 99% pure helium in order to inflate the balloons.

Some pictures of the above items will now be shown:

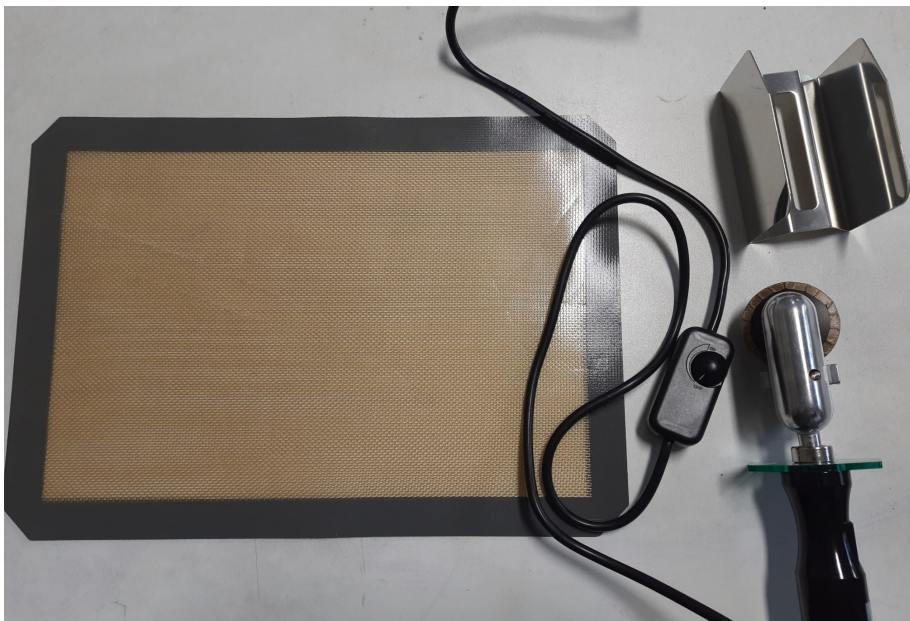


Figure 5.15: Hand wheel sealer with knob for changing temperature and the silicone placemat.

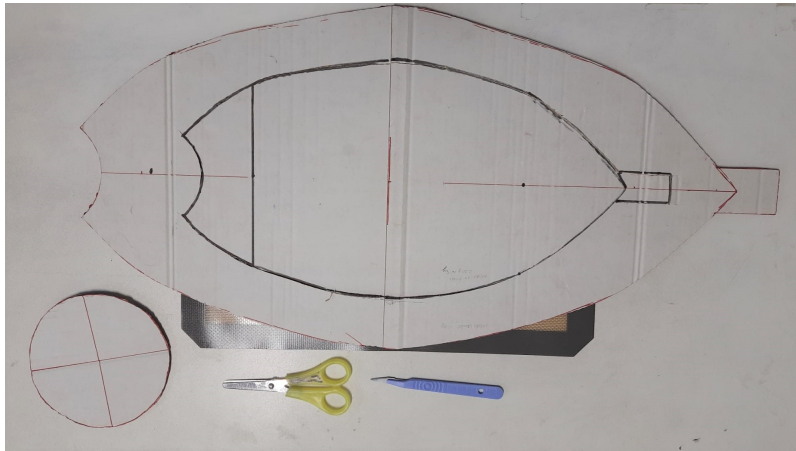


Figure 5.16: Templates made of cardboard and some tools used: scissors and scalpel.

To begin building the balloon, start by preparing a suitable sheet of Mater-Bi; this is done by "opening" the bag and making a rectangular sheet out of it. At this point it is critical to carefully inspect the resulting sheet as there may be holes or scratches that would compromise the balloon's seal. Now it is possible, by making use of a previously drawn model, to trace the shape on the sheet and then cut it out with the scalpel. The model used was made of cardboard and the measurements are expressed in the drawing below:

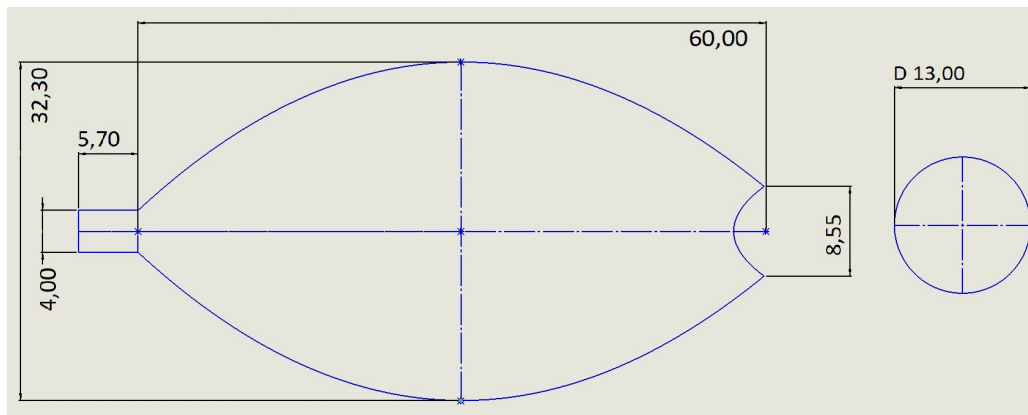


Figure 5.17: Cad model of the balloon with dimension in centimeters.

The measurements given are for making a balloon with a diameter of $0.20m$, taking into account some extra material to make the welds (specifically, $4mm$ of material was considered necessary for each weld.). Having cut out four "A" shapes and one "B" shape, it is possible to begin the welding operation. Connect the hand wheel sealer to the power and turn it on via the potentiometer. It will take several minutes for the system to reach the optimum temperature of about $70^{\circ}C$; in the meantime, it is convenient to lay out the silicone placemats and prepare the material to be processed. Each time, before starting a solder on the balloon, it is important to do a test on some discarded material to make sure that the temperature is the optimal one; if it is too low the two flaps will not stick properly, if it is too high the material will be irreparably damaged getting a hole in it. Once everything is ready, it is possible to proceed to solder together the four "A" elements and then the "B" closure element at the top. Particularly critical is the lower part where the beak is created to allow inflation and connection with the PCB. Each solder should be visually inspected and tested for strength. In case it is not strong enough the soldering operation can be repeated until the desired result is achieved.

The balloon is welded from the inside, so it will need to be turned inside out and will then be ready to be inflated. The beak can be closed using a thread. Once the PCB is connected, again using the same thread, our system will be ready to launch.



Figure 5.18: Balloons ready to be launched.

5.6 A possible new shape

As will be explained in the section concerning the experiment, during the inflation step, some balloons showed small leakage in the connection area between the spherical and the cylindrical geometry that allows inflation and probe attachment. This happens because there is a high concentration of tension in this area due to the small radius of curvature of the geometry. To solve this problem it will be necessary to eliminate these areas by avoiding edges and trying to fillet as smoothly as possible.

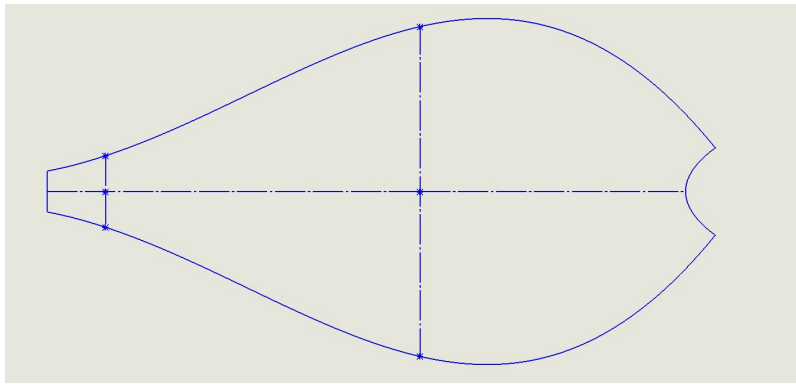


Figure 5.19: A possible new balloon geometry, stronger than the previous one.

In the image above, a drawing of a possible new geometry is shown; as it can be seen in the bottom part there is no longer the sharp-edged area, but everything is connected by curved lines. This should make the balloon significantly more resistant to tearing and leakage. One drawback of this geometry is that it deviates slightly from the spherical shape by losing symmetry on one axis. As is often the practice in the design process, the design will always turn out to be a compromise between various aspects, in this case between spherical shape and strength. In case there will still be a need to build balloons manually in future experiments, adopting this type of geometry might be the best choice to have more reliable balloons.

Chapter 6

OAVdA experiment

Experimental activity is a fundamental part of scientific research that allows the whole system (instruments, materials and software) used to be put to the test. It brings benefits both in the case of a positive outcome and in the case of a negative one; in the first case, a validation of methods and tools used is obtained, confirming that the path being taken is the right one; in the second case, on the other hand, it allows us to determine that some instruments, materials or approaches are not functional for our project. It is often very difficult to predict the behavior of systems theoretically, even if laboratory tests are carried out, because, in the real case the conditions will be uncontrolled and unpredictable unlike those present in the laboratory.

The system (balloon, radiosondes and ground receiving station) we used is not yet the final one that will be used for future data collection campaigns; developments and testing of new components are still needed. What we performed was the first experiment in which our radiosondes were allowed to fly freely in the atmosphere; previously the probes were kept tethered to the ground. Also, until now, an experiment with ten radiosondes had never been carried out, and this will also serve to test the behavior of the ground stations with such a

number of probes (a number that will increase in future experiments). Before launching, our sensors were calibrated through the use of professional instrumentation provided and used by qualified personnel from the "Istituto Nazionale di Ricerca Metrologica" (INRiM). This made it possible to verify their accuracy in the environment. It is possible to divide the analyses performed into three groups.

- **PHT analysis.** It consists of the gathering and analysis of thermodynamic data collected by the pressure, humidity and temperature sensor.
- **Positioning analysis.** Through the position and time data, the relative distance between the probes at each instant can also be reconstructed; in this way, Richardson analysis can be performed.
- **Stereovision analysis.** Through the use of two appropriately positioned cameras, it is possible through the principles of stereovision to derive the distance of the probes from the cameras. This makes it possible to validate the data from the GNSS module through an independent system.

The following sections will show all these topics, from preparation to analysis of the collected data while also describing the problems that were encountered during the experimental activity.

6.1 Logistics and operations in Turin

Preparation for an experiment is crucial; the success or failure of a project will depend on it. Especially when dealing with experiments involving different fields (aerostatics, electronics, computer science etc...) and therefore different people having efficient and collaborative logistics can make all the difference. The preparation of this experiment took several

months, to receive the imported parts, to make the balloons, and to prepare the software. In particular, my work at this stage focused on studying the sizing of the balloons and making them. In the first phase it was necessary to learn the use of instrumentation and the handling of materials (hand wheel sealer, scalpel, mater-bi etc...) and later to learn how to make balloons. Once the methodologies were mastered, there was the phase of sizing and then studying the different sizes, which was followed by seal tests in the laboratory. Having determined the characteristics that the balloons should have, the assembly step began where 15 balloons were assembled: 10 needed for the experiment and 5 as a spare. Contrary to what one might think, assembling a balloon is an operation of great patience and precision: an average of 4 hours of work per unit is required. The assembly of all the balloons has finally taken several weeks of manual labor. At this point, all the equipment and devices needed for the experiment were collected: 15 balloons, 10 PCBs and related batteries, 2 ground stations for data acquisition, latex balloons as an additional backup, helium cylinders, meter for measuring distances (both analog and laser), power strips, Schuko and industrial outlets, extension cords, 2 cameras and related components to be able to do the stereovision analysis.

Unfortunately, it was not possible to find all the necessary batteries with the previously decided specifications, 2 batteries turned out to be heavier than planned. This led to consequences in balloon flight that will be explained later.

6.1.1 Location of the experiment

The place that has been chosen to carry out the experiment is the astronomical observatory of the Valle d'Aosta called OAVdA; this place, where the previous experiment with tethered balloons was carried out, has reconfirmed its availability to host the project and provide the necessary support. The observatory is located in the upper part of the Saint-Barthélemy

valley, not far from Nus and reachable from Turin by car in an hour and a half. It is located at an elevation of 1675 meters above sea level, on a kind of almost flat terrace well exposed to the south. It is surrounded on three sides by mountains that reach as high as 3,000 meters above sea level, while to the south the landscape is more open with the valley descending rapidly toward Nus. The observatory has a professional-grade meteorological station and its collected data has been made available. A room where instrumentation can be prepared, as well as shelter from the cold, has been provided, in addition to a yard where operations can be carried out.



Figure 6.1: Saint-Berthélemy Valley and OAVdA observatory, shot from above. *Image taken from: "Paolo Rey. Regione autonoma valle d'aosta per il progetto transfrontaliero interreg alcotra "exo/eco" realizzato con fondi europei. <https://www.oavda.it/chi-siamo>. Accessed on 06 January 2023" [41].*

6.1.2 Preparation, calibration and execution

The day chosen for the experiment was November 3, 2022, a day that turned out to be sufficiently suitable for carrying out our operations, with the absence of dominant winds (except for a probable updraft on the slope where the observatory is located) and widespread cloud

cover. This makes it possible to test the operation of the probes outside and inside the clouds. The departure at sunrise from Politecnico di Torino made it possible to reach the site early in the morning so that there was plenty of time to prepare the equipment.

The work that needs to be done involves inflating the balloons, preparing the probes to be connected to them, preparing the ground receiving stations and properly positioning the two cameras.

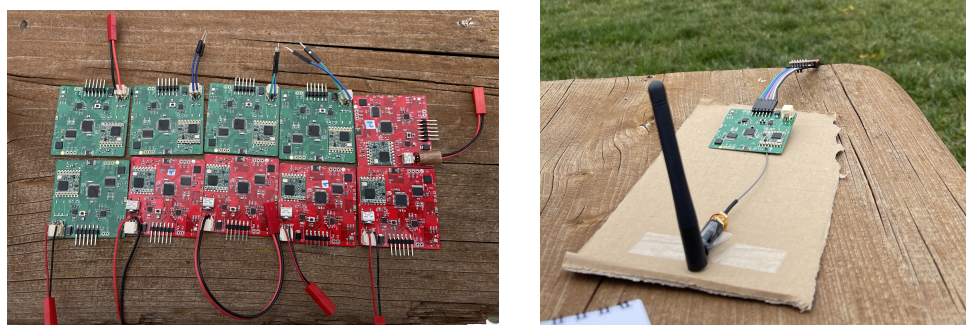


Figure 6.2: On the left: the ten radiosondes that will be mounted; on the right: the antenna ready to receive signals.

During the attachment process of the probes, it was noticed that the balloons were not found to be able to lift the probes mounting the latest purchased batteries, which were heavier than planned. In addition, it was observed that some balloons were showing small leaks in the area where there is the transition between the spherical and cylindrical geometry that allows inflation and connection with the probe; this region has welds with very narrow curvature angles that cause a considerable concentration of tension capable of compromising the integrity of the material. Although they had shown proper sealing in the laboratory (under stationary and controlled conditions), some balloons were damaged probably due to waving while tethered to the ground or as a result of overinflation in an attempt to be able to lift the heavier batteries. A possible solution to this problem will be presented in the concluding section.



Figure 6.3: Photo of balloon inflation.

To overcome these problems and perform the launch, it was decided to attach each individual probe to two balloons, and since Mater-Bi ones were not sufficient, some made of latex were also used.

After all the balloons and other equipment were prepared and ready for use, a calibration was performed by comparing the data from the probes with those obtained through INRiM's measurement instruments. Having prepared the measuring equipment and tied the balloons to a fence, it was necessary to move a few meters away so as not to affect the temperature measurement by the radiation produced by human body heat.



Figure 6.4: Calibration phase: temperature measurement by INRiM instrumentation and mounted probes.

The following graph shows the measured values; the ten probes were numbered from 20 to 29. Radio-probe 27 was excluded due to a malfunction probably in data transmission.

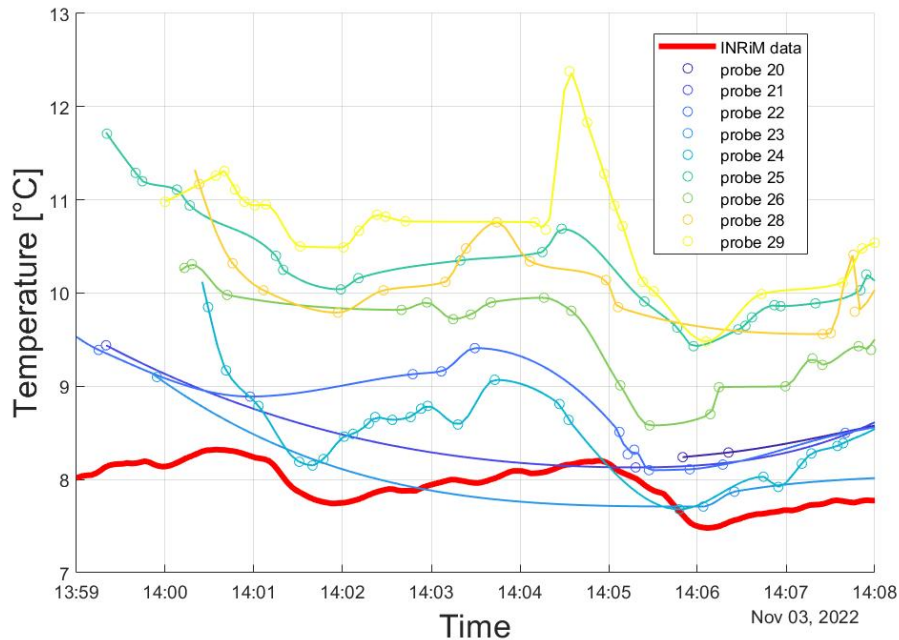


Figure 6.5: Comparison of temperature data from INRiM instrumentation and radiosondes. It is possible to see that radiosondes have a tendency to slightly overestimate the temperature by a few degrees.

It can be observed that after the first few minutes in which there is a decrease in temperature due to the elimination of the disturbance caused by human irradiation, the measured values tend to stabilize; in particular, the values measured by the probes turn out to be slightly higher than those of the instrumentation probably due to the heat produced by the system itself. It is also possible to notice a slight discordance in the measured values between the various probes.

In order to calibrate the probes, the average error was calculated by subtracting the values obtained from the instrumentation (assumed to be exact data) from the average

of the temperatures received from the probes. Some probes were excluded from these calculations (20,27,29) because of loss of data (20,27) or because an unlikely temperature peak was obtained (29). The following graph shows the calibrated temperature values.

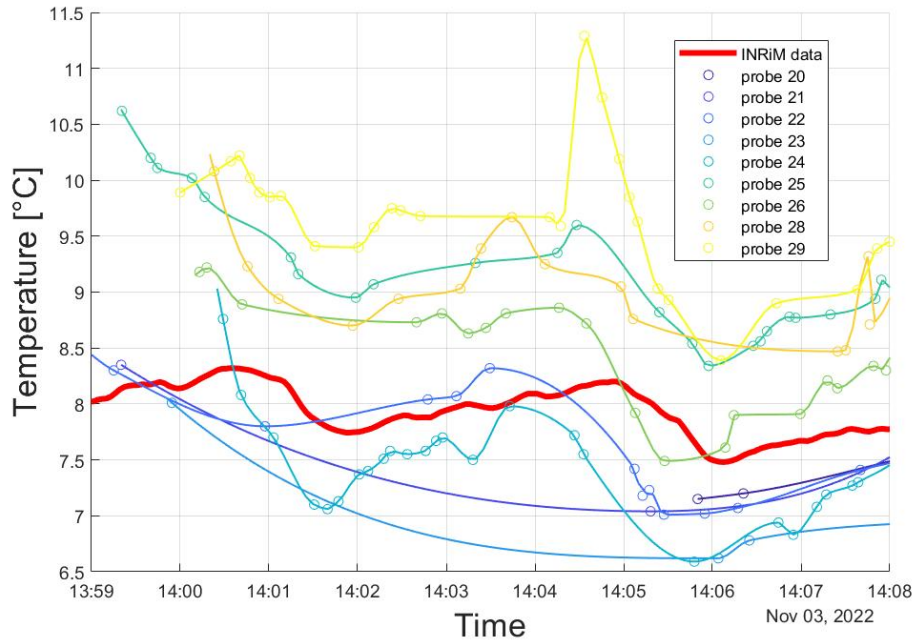


Figure 6.6: Calibration of temperature data based on probe averaging. The difference between the average of all temperatures and the values measured by instrumentation was subtracted from each curve obtained by radiosonde.

Property	Value
Mean error	1.09 °C
Max absolute error	2.74 °C

Figure 6.7: Table representing the mean temperature error obtained by averaging the data from all probes and the maximum absolute error of the individual probe.

In cases where different sites are to be measured and the signals will not be averaged (different altitude, residence in different eddies etc...) it is useful to do a more precise job by calibrating the measurement of each individual probe.

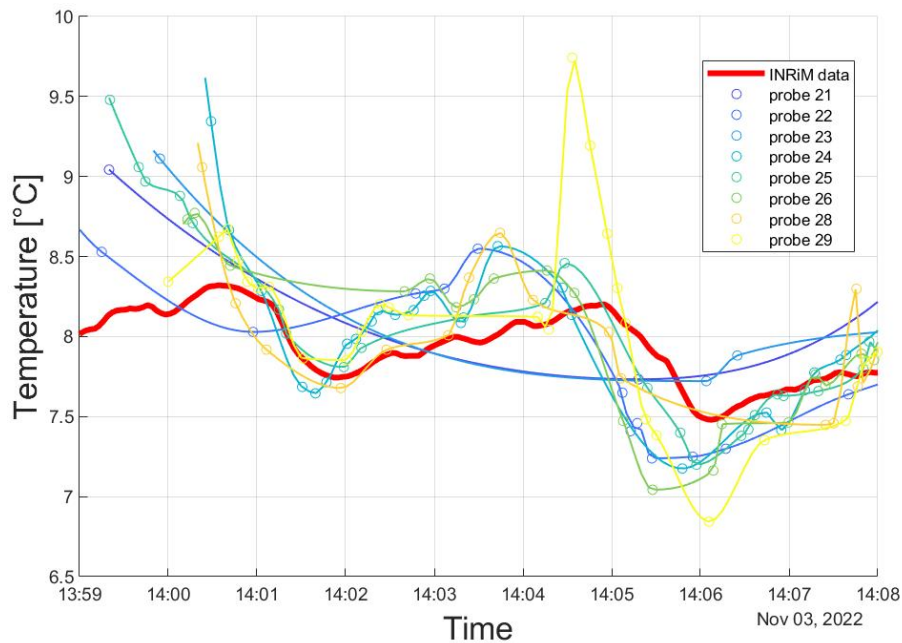


Figure 6.8: Calibrated temperature for each individual probe. To the values of each radiosonde was subtracted its average error compared with the instrumentation.

The graph just given shows the individually calibrated temperature curves related to the various probes. From each curve was subtracted its own the average error with respect to the data obtained by INRiM instrumentation.

The next image shows the relative humidity values measured by the probes during the temperature calibration phase. Unfortunately, no reference measurement is available to validate these data; instead, some considerations will be made based on results obtained in past experiments.

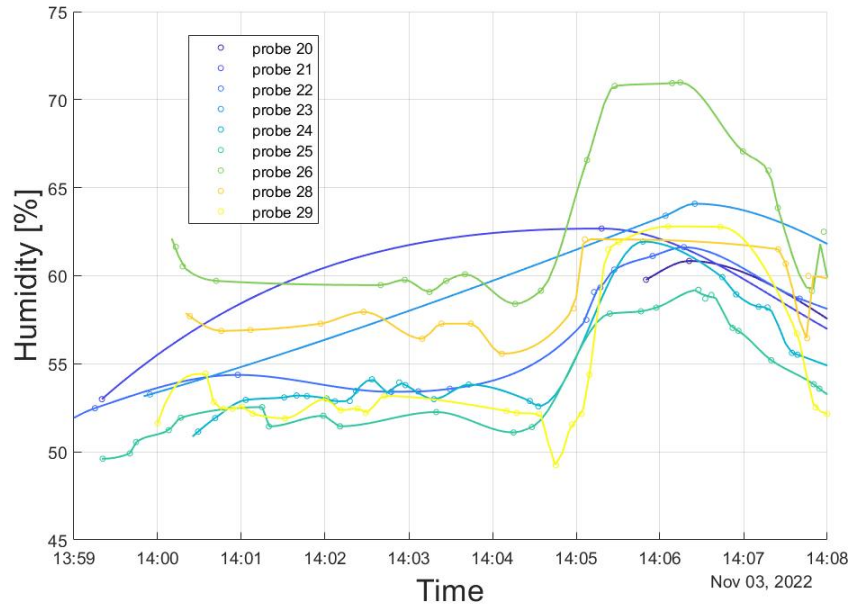


Figure 6.9: Relative humidity measured during the calibration phase. Although the measured data are slightly different, the probes measure concordant trends.

A well-known problem in relative humidity measurement is inaccuracy at high values near air saturation. This phenomenon turns out to be even more pronounced in case extremely small sensors, such as the BME280 used, were being considered. Even the highest performing sensors, on the other hand, tend to fail in measuring the supersaturation condition. During previous experiments, tests were conducted to compare measurements obtained through the PCB-mounted modules of the COMPLETE project with those of other, more accurate systems. The next image shows the comparison with the Vaisala probe, during a weather radiosounding launch. This launch took place on June 9, 2021 at Levaldigi Airport with the collaboration of ARPA Piemonte.

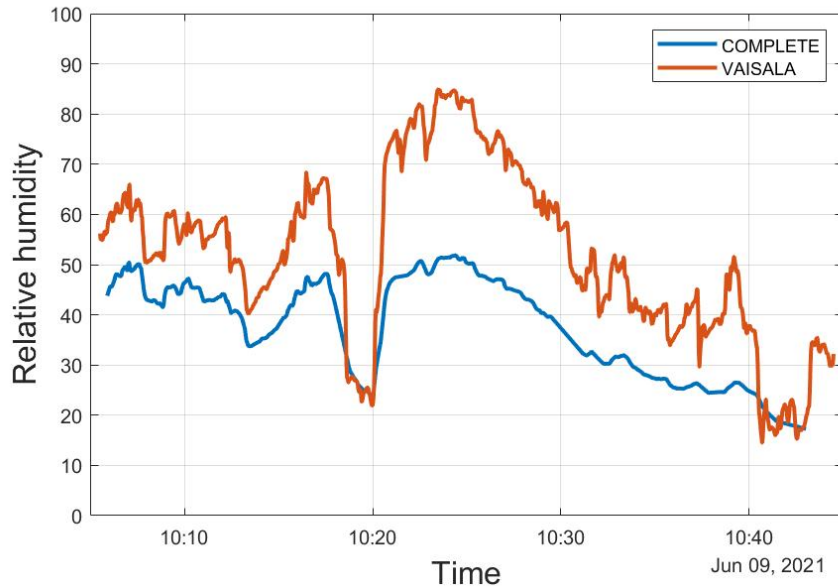


Figure 6.10: Comparison of relative humidity data measured by the Vaisala probe and that of the COMPLETE project (9/06/21 experiment, Levaldigi airport). It can be seen that although there is a difference between the measured values the trends are comparable: maximum and minimum peaks tend to be detected by both probes.

In the graph just shown, the problems just described can be observed. The BME280 sensor, which is much more compact and has lower power consumption than the one used in the Vaisala probe (where the sensors are mounted on a 1.3m diameter balloon) experiences difficulties in measuring high values of relative humidity. It can be seen that the values tend to be underestimated and the measurements fail to exceed 50–60% relative humidity. Despite this, the measured trend seems to be faithful to that detected by the Vaisala probe; the maximum and minimum peaks appear to be concordant.

In the future, this aspect needs to be better investigated. The use of a new sensor could be considered, or an attempt could be made to mitigate the error of this one by making use of modifications in the assembly or corrective post-processing of the data obtained.

The next graph will show the atmospheric pressure values measured during this calibration phase.

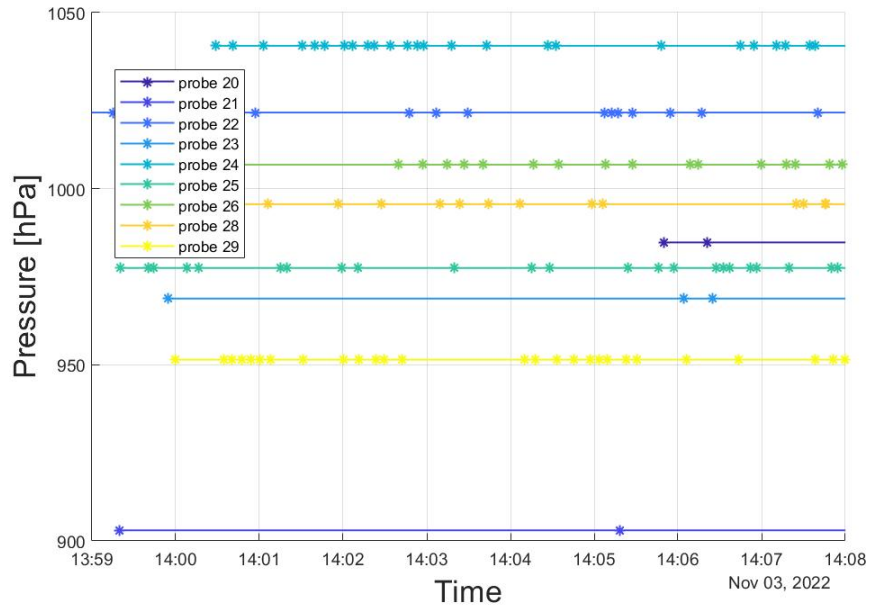


Figure 6.11: Atmospheric pressure measured during the temperature calibration phase. It is possible to notice immediately that something is wrong: all probes measured constant values of pressure.

From the graph just shown, it can be seen that the sensors returned a constant value throughout the entire measurement interval, which is obviously not reliable. Since the problem occurred simultaneously in all the probes, a malfunction in the pressure sensors should be excluded. Later, it was discovered that there was an error in the software library code that unfortunately caused the probes to return a constant value. For this reason, it was not possible to measure the change in atmospheric pressure during the experiment.

At this point the actual launch took place, all the balloons were picked up and released at the same time, at 14:13 and 30 seconds. Some pictures of the launch and the next instants follow.



Figure 6.12: Balloons a few moments before launching: they will be released all together from the same spot.



Figure 6.13: Balloons launched: first moments of flight.



Figure 6.14: Images taken about 10 and 40 seconds after launch, respectively. It can be seen that the probes proceed in a cluster and follow the air swirls.

Right after the launch, the balloons quickly started to gain altitude due to the aerostatic

thrust given by the combination of two balloons. It was possible to visually observe that during the first minute they flew close to each other, in the same cluster while having visible turbulent movements. After a couple of minutes, it was clearly seen that the balloons started to follow different paths, a sign that they entered different turbulent eddies with significant size scales. A few minutes later, the balloons passed cloud altitude and were no longer visible.

6.2 Data from experiment

This section will present through an extensive use of graphs and images the data obtained during the radiosonde flight. Through the entire system of probes and receiving stations, a large amount of data regarding atmospheric conditions and three-dimensional positioning of the probes over time were obtained. Once the data were acquired and saved, the post-processing phase began. A dataset was created in a format that can be used in software for calculations and graphing, such as Excel and MatLab. In particular, Matlab was used for the processing of all calculations and graphs in this work, using several packages in addition to the basic version.

The graphs on the following pages show the path taken by the probes from the time they were released to the time the signal was lost. An early loss of data reception was seen, the reasons for which have not yet been clarified; as according to tests and lifetime estimates knowing the capacity of the batteries, the system should have been transmitting for more than an hour and up to two hours at best. In the experiment, most of the radiosondes transmitted correctly for more than 30 minutes, while three of them reached 40 minutes; the operating times turned out to be shorter than expected.

The path traveled by the probes projected on a satellite map will now be shown, displaying flight time, distance traveled and altitude.

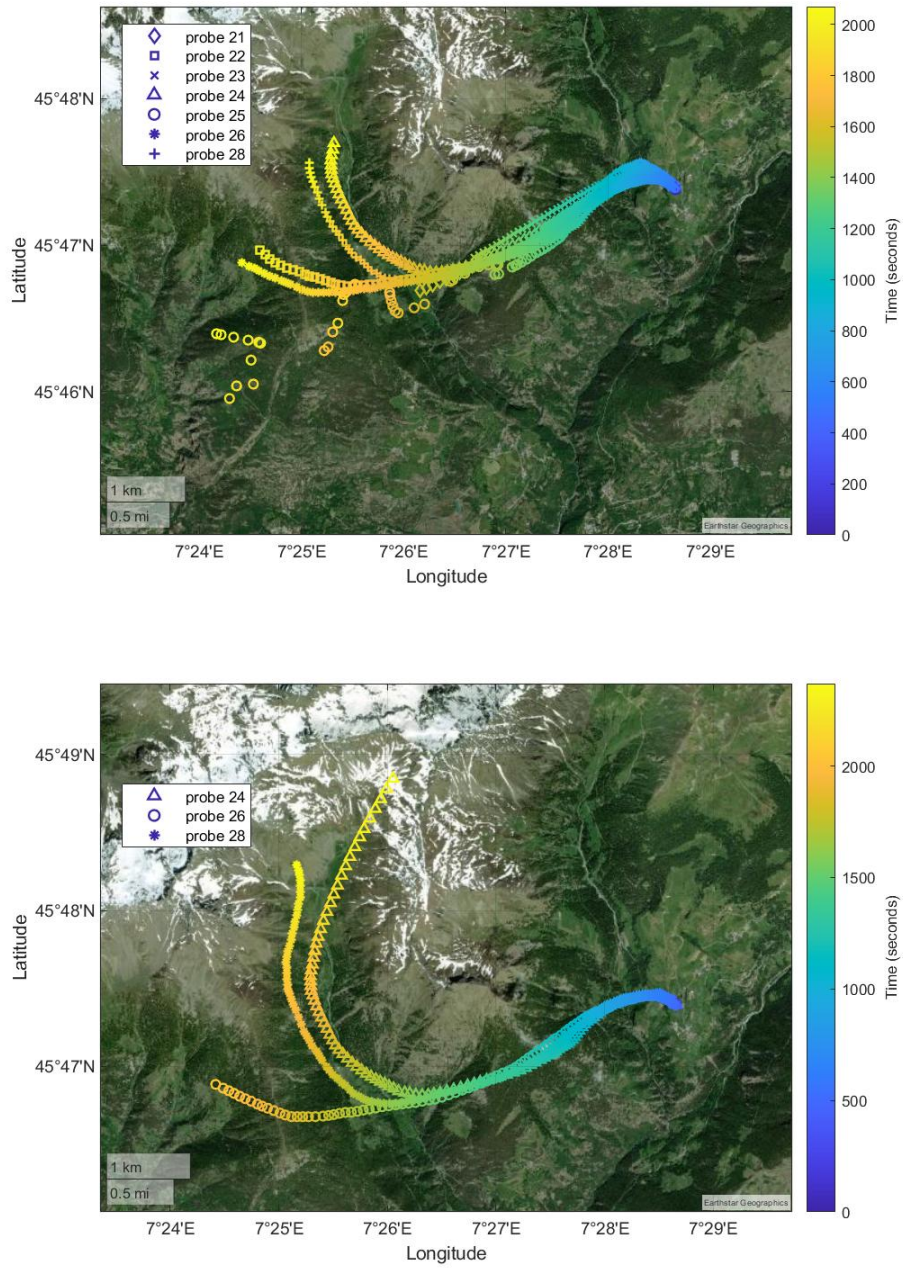


Figure 6.15: The top image shows the path taken as a function of time by all working probes while the bottom image for three selected ones; some of them reached 45 minutes of broadcast time.

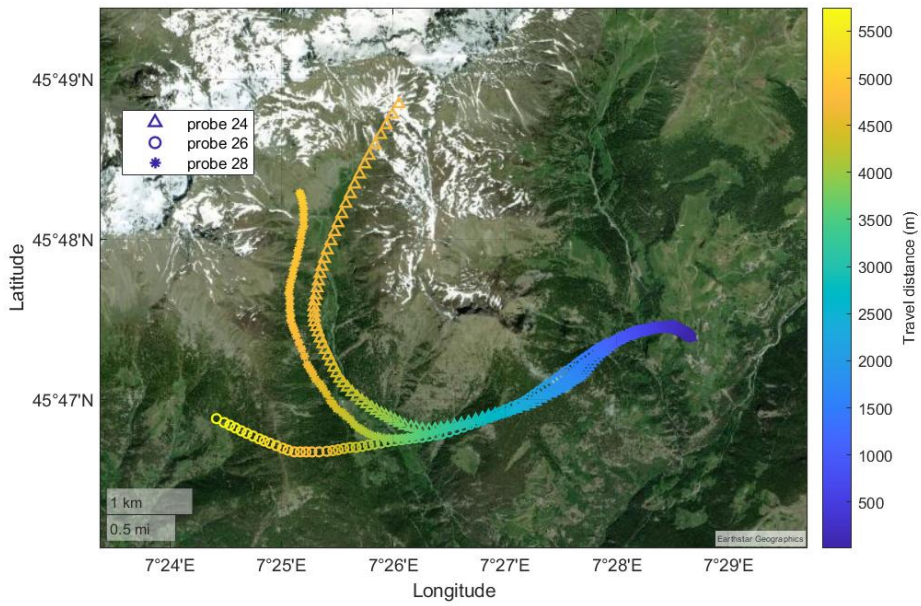
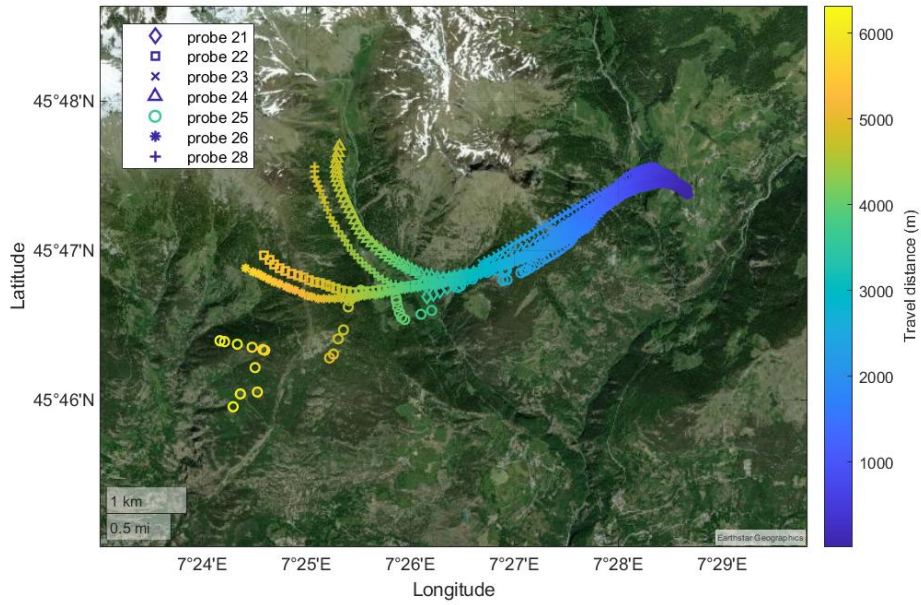


Figure 6.16: The two images show the distance traveled by all working probes and for three selected probes, respectively; some of them reached up to 5 kilometers.

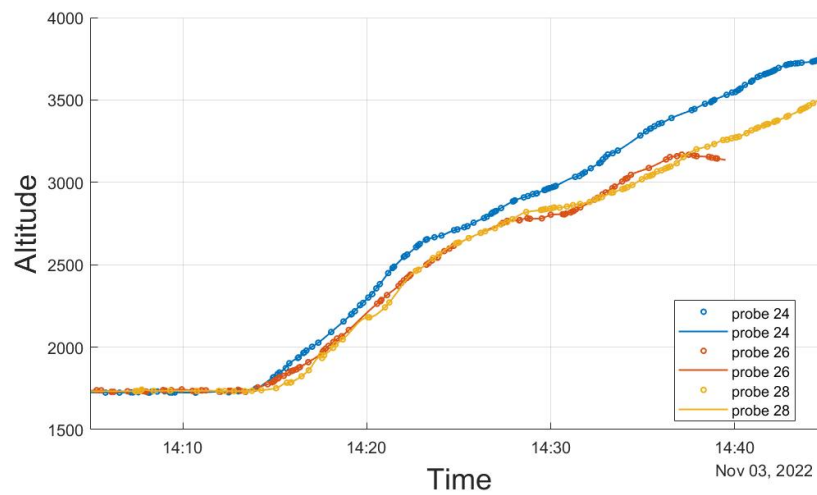
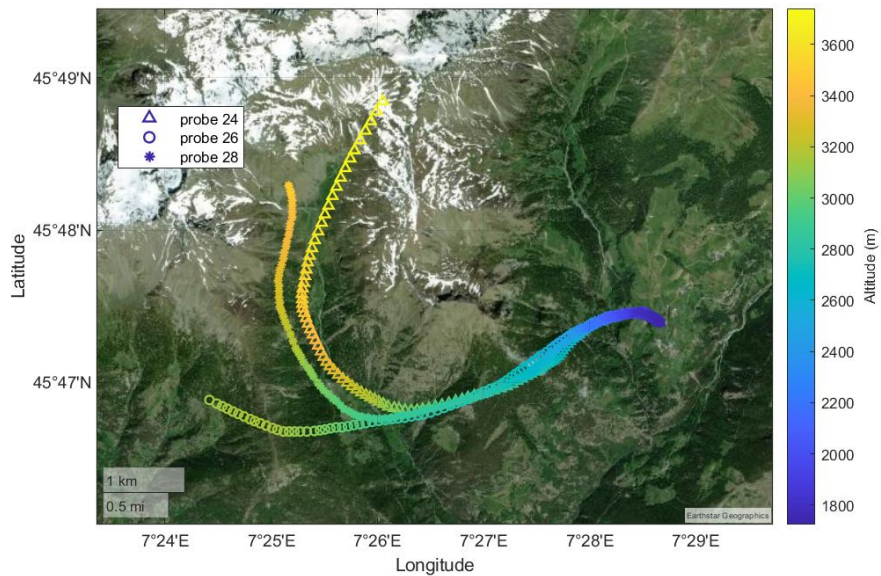


Figure 6.17: The two images show the path followed by three selected probes and their relative elevation. Due to double balloons per probe, high altitudes of over 3500 meters were reached.

It can be seen from the various graphs above that immediately after the launch, the probes began to gain altitude and move first slightly to the northwest and then sharply to

the southwest; some probes (24,26) in the second half of their path turned strongly to the north. Probes that continued transmitting for at least 30 minutes (22,24,25,26,28) traveled distances on the order of 6 kilometers in different directions.

Regarding altitude, further considerations can be made. The variation for three selected probes based on data continuity has been reported. It can be seen from the graphs how the probes continue to gain altitude during the entire period. In addition to the contribution of updrafts likely present along the valley, the determined cause is definitely the use of two balloons for each probe. As shown in the section inherent to sizing, as the volume increases, the buoyancy altitude increases considerably, and compared to the approximately 2000 to 2500 meters predicted, having almost doubled the resulting aerostatic force, the probes in question showed signs of stationarity between 3000 and 4000 meters. This, of course, should not happen in the case of accurate measurements, where all probes should be as equal as possible and possess a well-determined buoyancy altitude; however, the main purpose of this experiment (as well as previous and subsequent ones) is to test the functioning of the whole system.

The following graphs will show the evolution of thermodynamic quantities. As anticipated in the calibration section, due to an error in the software, it was not possible to measure the pressure during the experiment. However, it was possible to extrapolate it from the data provided by the GNSS module. Knowing pressure and temperature at reference altitudes, through the use of barometric formulas it was possible to estimate the atmospheric pressure at the altitude detected by the radiosondes. The formula is as follows:

$$p = p_0 \cdot \left(1 - \frac{g \cdot h}{c_p \cdot T_0}\right)^{\frac{c_p \cdot M}{R_0}}$$

where: p is the pressure, p_0 the pressure value at sea level, g the gravitational acceleration, h the altitude above sea level, c_p the constant-pressure specific heat, T_0 the

temperature at sea level, M the molar mass of dry air and R_0 the universal gas constant.

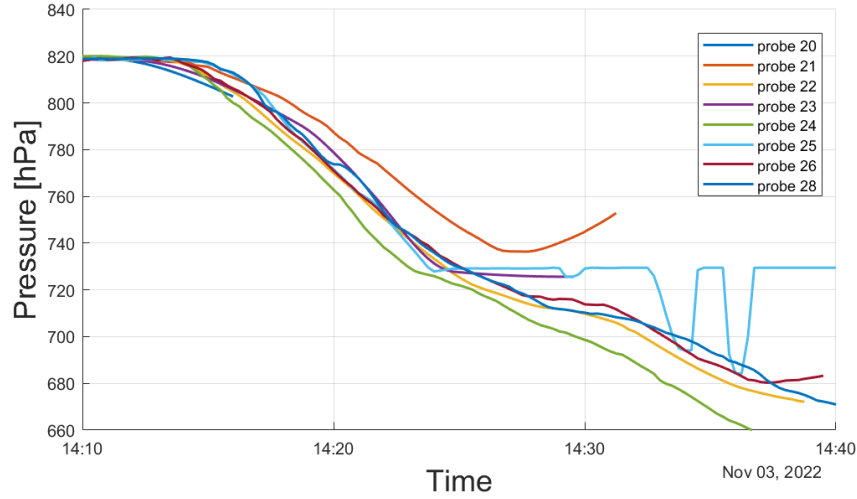


Figure 6.18: Pressure data recovered from GNSS module and barometric formula.

The calculated pressure values appear to be valid, although it should not be neglected that they are only an extrapolation and not a direct measurement. In fact, the formula used represents the decrease in pressure for an atmosphere with conditions averaged over geographic locations and meteorological conditions.

The change in relative humidity and temperature for all probes and for three selected ones are then shown; the time of launch is also plotted on the graphs for better clarity. From the graphs it can be seen that for humidity near the time of launch there is a sharp spike followed by a steep descent; this spike could probably have been caused by pre-launch handling. It is also possible to notice that the probes never record the presence of saturated air, despite having passed through consistent cloud cover. During the flight, another peak is observed after about 15 minutes of flight, which could correspond to the probes' entry into the clouds. After that peak, the values stabilize at 65-70% relative humidity.

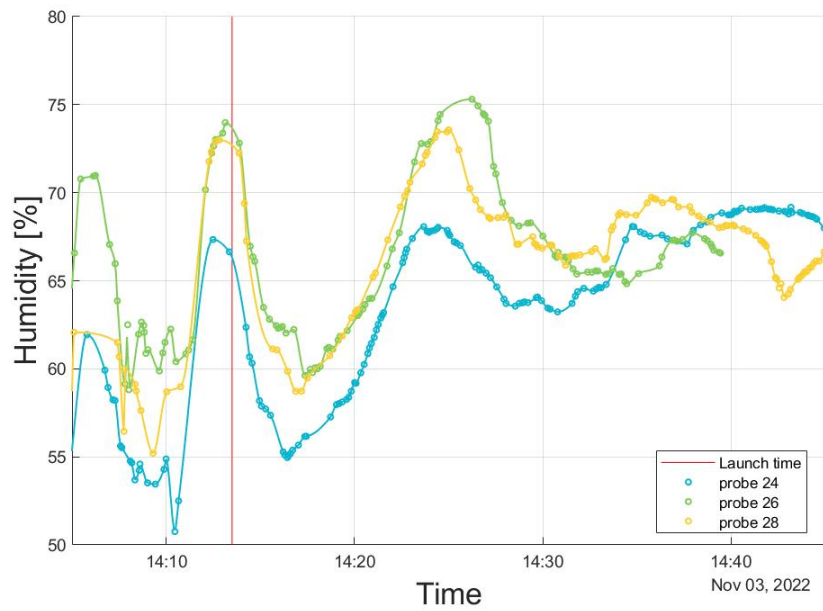
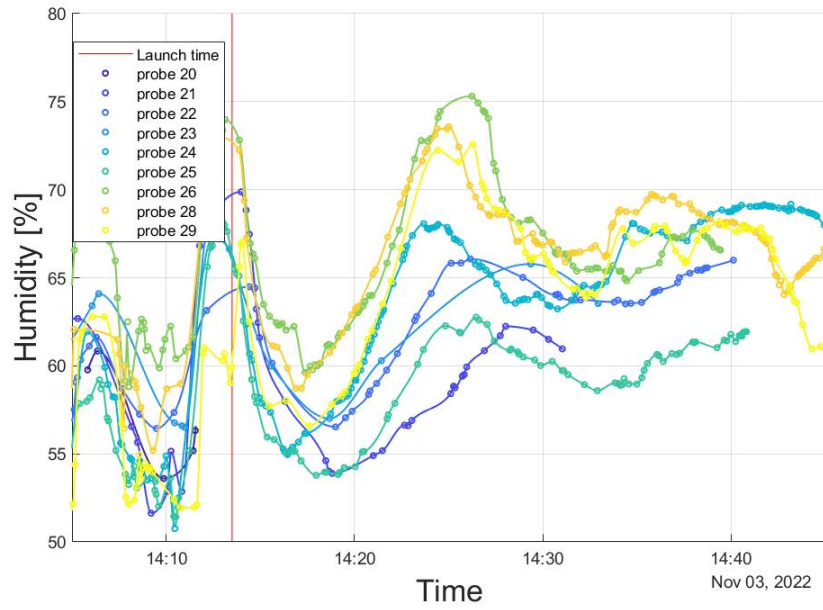


Figure 6.19: The two graphs above show the change in relative humidity for all probes and for three of them selected. It is possible to observe that although most of them reached the cloud base none detected values close to saturation; peaks were measured, however.

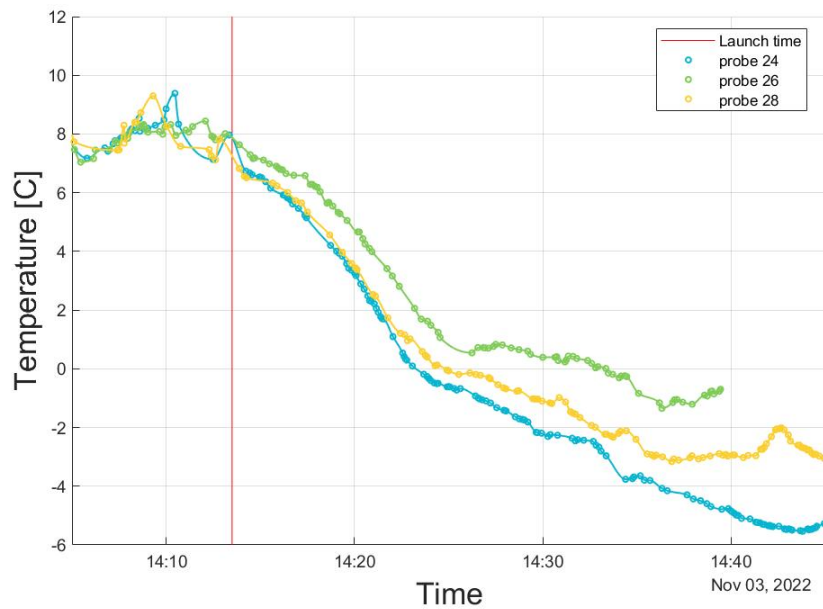
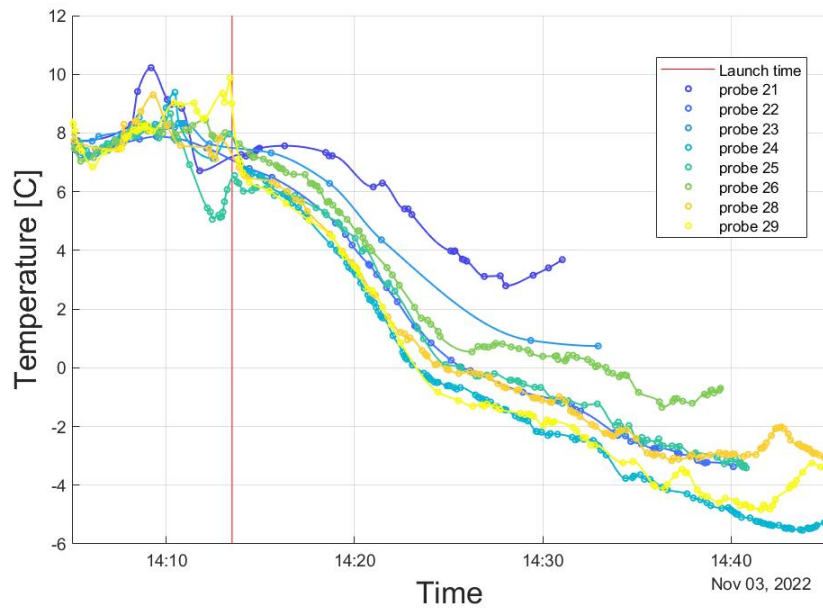


Figure 6.20: The two graphs above show the change in temperature for all probes and for three of them selected. It is possible to see a change of slope in the vertical thermal gradient (considering the almost constant rate of increase in altitude): this could represent the entry into saturated air (clouds) by the probes.

The graphs showing the temperature values were corrected using the procedure presented in the previous subsection, correcting the values for each probe. Before launch, numerous fluctuations caused by disturbances brought by handling can be seen; after launch, almost all probes show agreeing trends. Because of the problem we had with batteries and balloons, Lagrangian sampling was not possible; however, since the probes traveled a considerable vertical distance, it is possible to make considerations about vertical thermal gradients. During the first 1.000 meters of ascent, which lasted about 13 minutes (14:13 - 14:26), a decrease of about 7 to 8 degrees was recorded, a value that is close to the dry adiabatic gradient of $-9.8^{\circ}C$ per 1.000 meters (by adiabatic gradient we mean an ideally static atmosphere whose moving air masses do not exchange heat; the vertical thermal gradient in standard air was set at $-6.5^{\circ}C$ per 1.000 meters). In addition, at 14:26 a clear drop in the gradient toward lower values can be observed; this confirms the fact that the peak in relative humidity actually corresponds to the entry into clouds and saturated air. In fact, after the gradient change, it drops to about $-5^{\circ}C$ per 1000 meters as that of saturated adiabatic air. From this, it can be concluded that the interface between clean air and cloud is located at approximately 2700 meters altitude. Probes that transmitted longer and reached altitudes above 3000 meters encountered temperatures below zero, reaching up to $-5^{\circ}C$.

Starting from the raw data, it was also possible to perform a basic spectral analysis. The following graphs show the spectral analyses for relative humidity, temperature, and wind speed data. Two graphs are given for each measure, one as a function of time (1/s) and the other as a function of altitude (1/m).

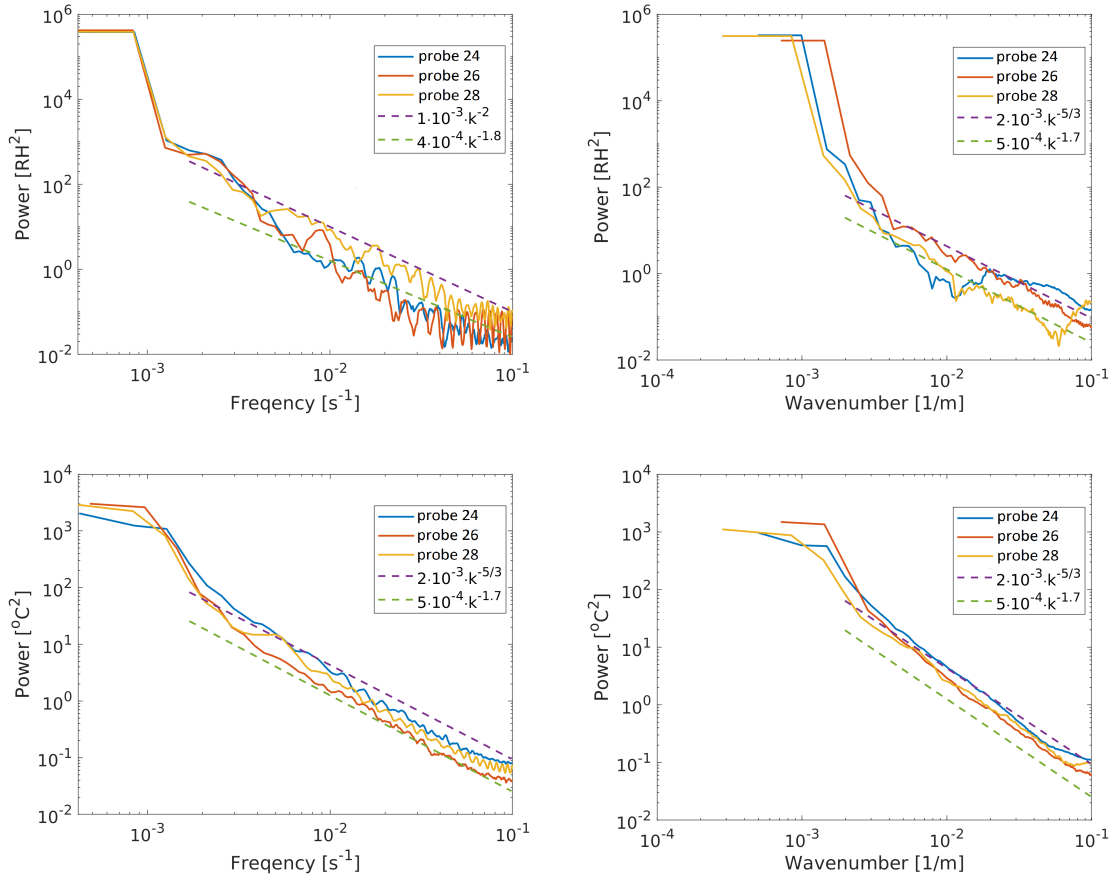


Figure 6.21: The four graphs show spectral analysis for temperature (top) and relative humidity (bottom) measurements for three selected radiosondes. The data are plotted in log-log axes; two trend lines were added for comparison. Because the original data have irregular time intervals the datasets were resampled at regular 5-second intervals.

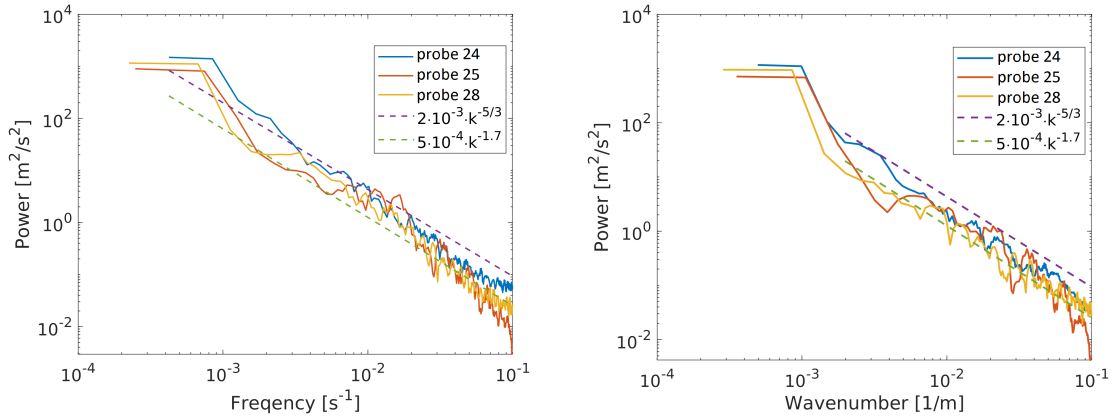


Figure 6.22: The two graphs show spectral analysis for wind speed measurements for three selected radiosondes. The data are plotted in log-log axes; two trend lines were added for comparison. Because the original data have irregular time intervals the datasets were resampled at regular 5-second intervals.

The original data were received at irregular time instants so resampling was necessary to perform such analysis. By linear interpolation the signals were resampled at regular intervals of 5 seconds. To obtain the graphs, the *FFT* (Fast Fourier Transform) was used. In particular, the measurements of three selected probes were analyzed. The graphs are in log - log format and trend lines were added in order to make comparisons.

To conclude this section, four more graphs are presented, which show the velocity values possessed by the three selected probes. The NED coordinate system (north-east-down) was used as the reference system.

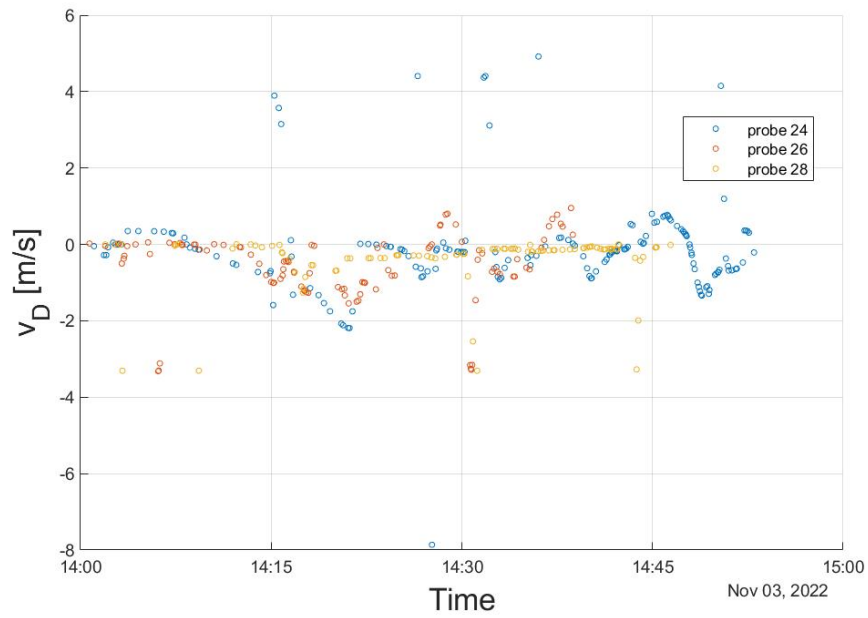
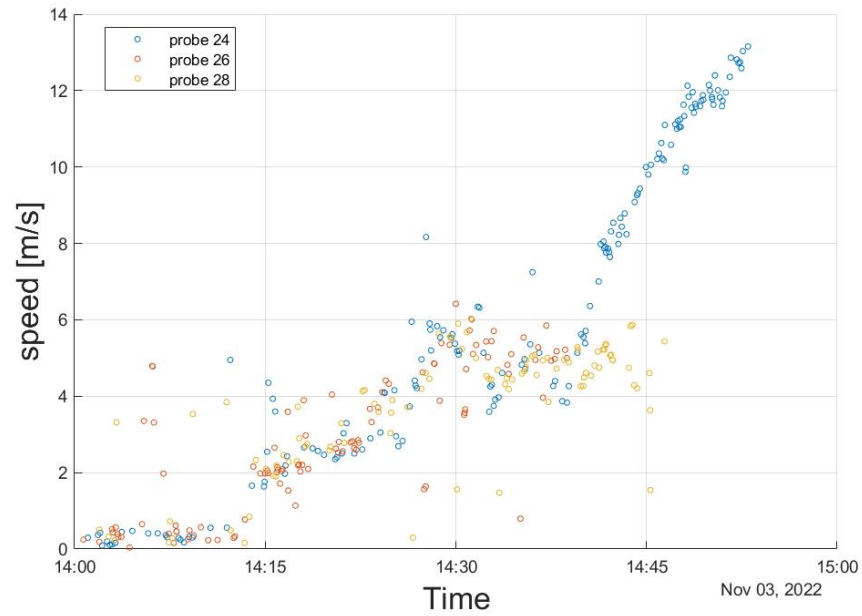


Figure 6.23: Top image: absolute velocity for three selected probes; bottom image: velocity along the vertical (down) axis. Some probes show an increase in speed with time; this, could be due to the marked increase in altitude.

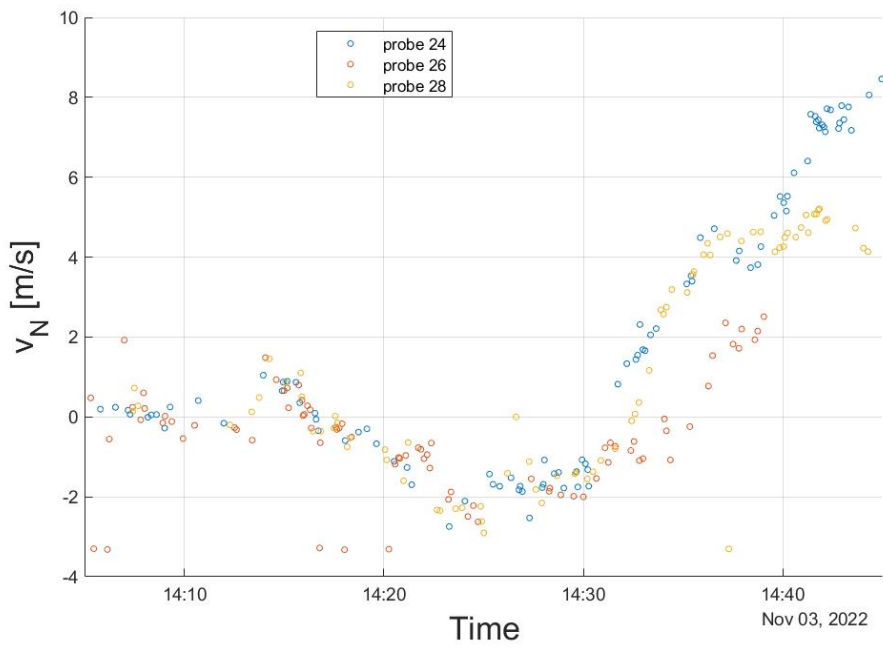
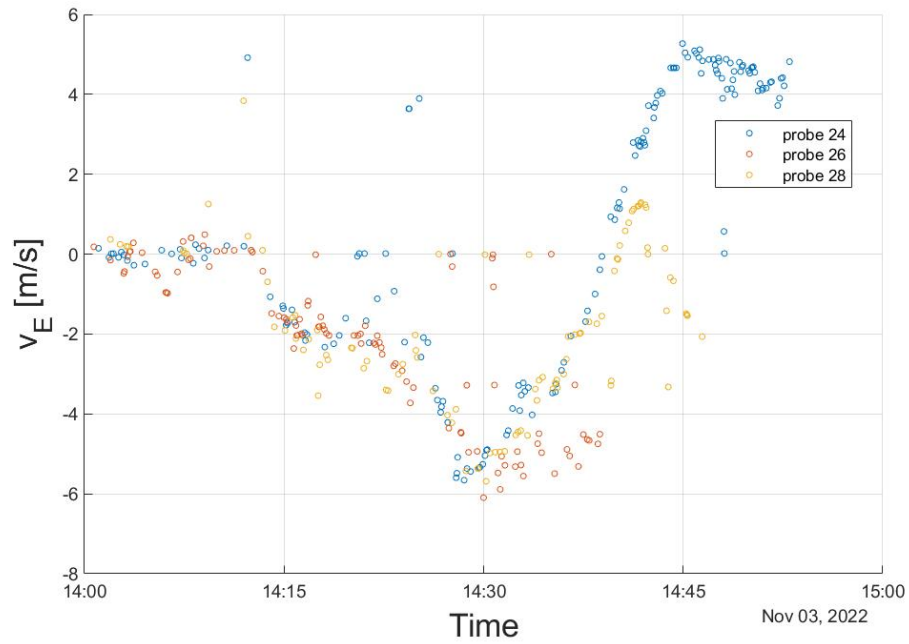


Figure 6.24: Top image: velocity along the longitudinal (east) axis for three probes selected; bottom: velocity along the latitudinal (north) axis.

6.3 Richardson analysis and comparison with previous experiment

This section will compare the distance-neighbor graphs of the previous experiment carried on 10/02/22 with those of the one just conducted. This comparison is interesting since in the previous experiment the probes were kept tethered to the ground while in this one free to fly.

In order to do such analysis, it is necessary to be in possession of the position data of each individual probe at the time instants of interest. Using GNSS modules, it is possible to obtain this type of data in a sufficiently precise way. The graph below shows the position of seven probes at successive instants of time, selected on the basis of data continuity.

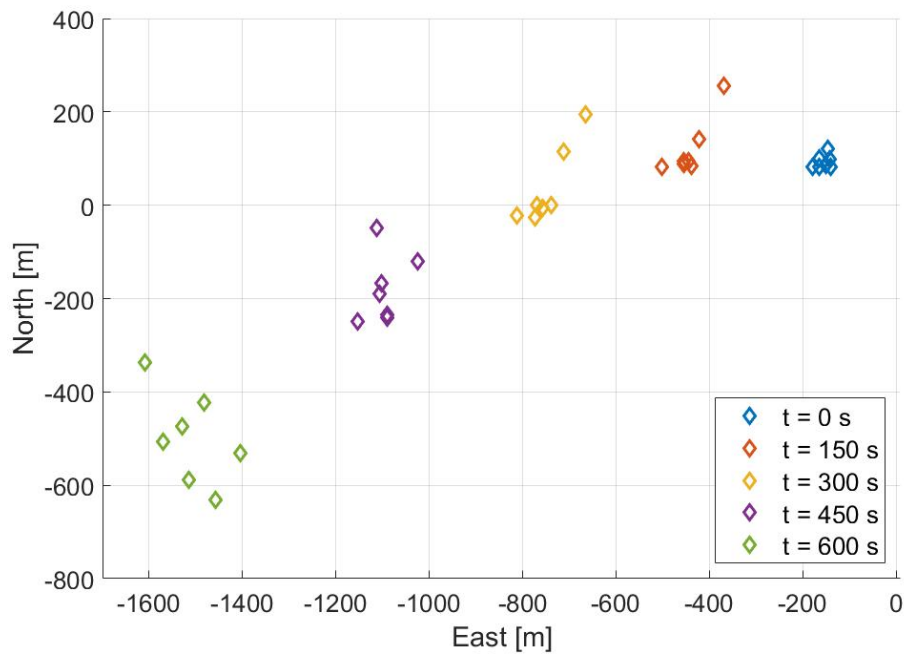


Figure 6.25: Plot of the position of probes at successive instants of time in a NED-type coordinate system. It is possible to see that the evolution of balloon positioning occurs in cluster.

Once position data are obtained, reciprocal distances can be derived, and, using methodologies and formulas shown in Chapter 3.3.2, Q can be calculated and distance-neighbor graphs can be plotted.

The first two graphs shown are from the previous experiment. The measurement was conducted through 4 probes which were tied to ground supports by a light thread that was about 15 meters long. A time interval of about 5 minutes was considered; the interval h was chosen to be 5 meters.

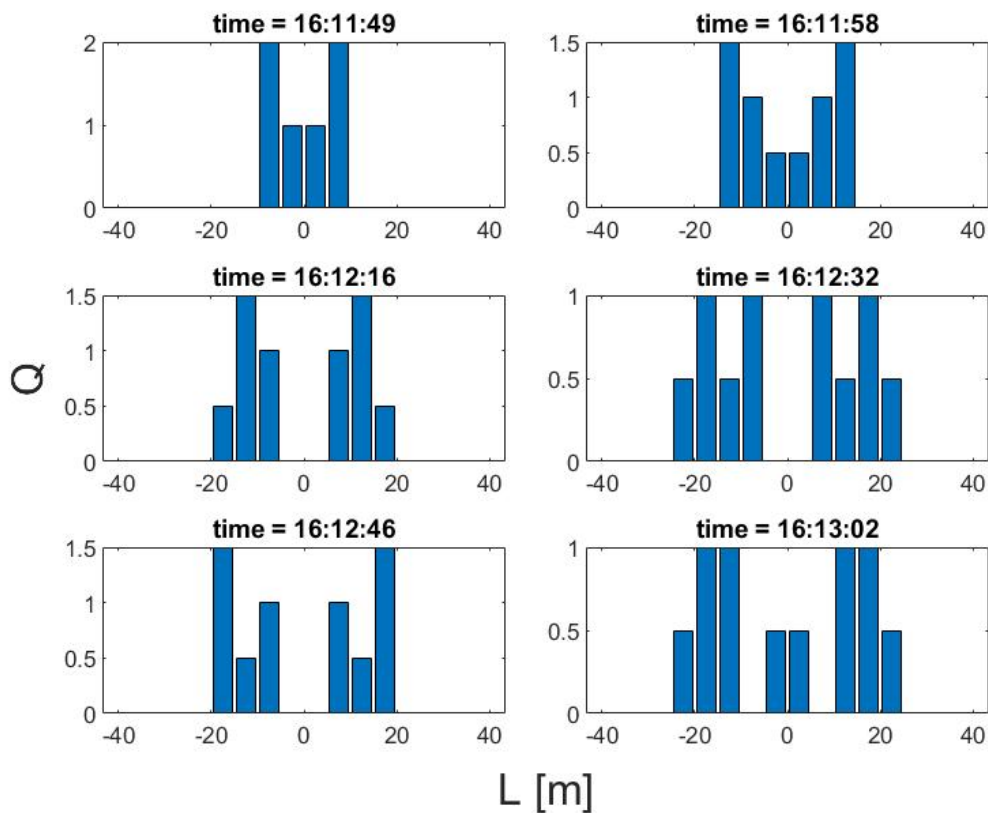


Figure 6.26: Distance-neighbor graph related to the 10/02/22 experiment at OAVdA. The dispersion of 4 balloons tied to the ground by a thread about 15 meters long is shown. The distance parameter h was chosen to be 5 meters. The effect of the constraints is clearly visible; the peaks oscillate around distances of about 20 meters (1).

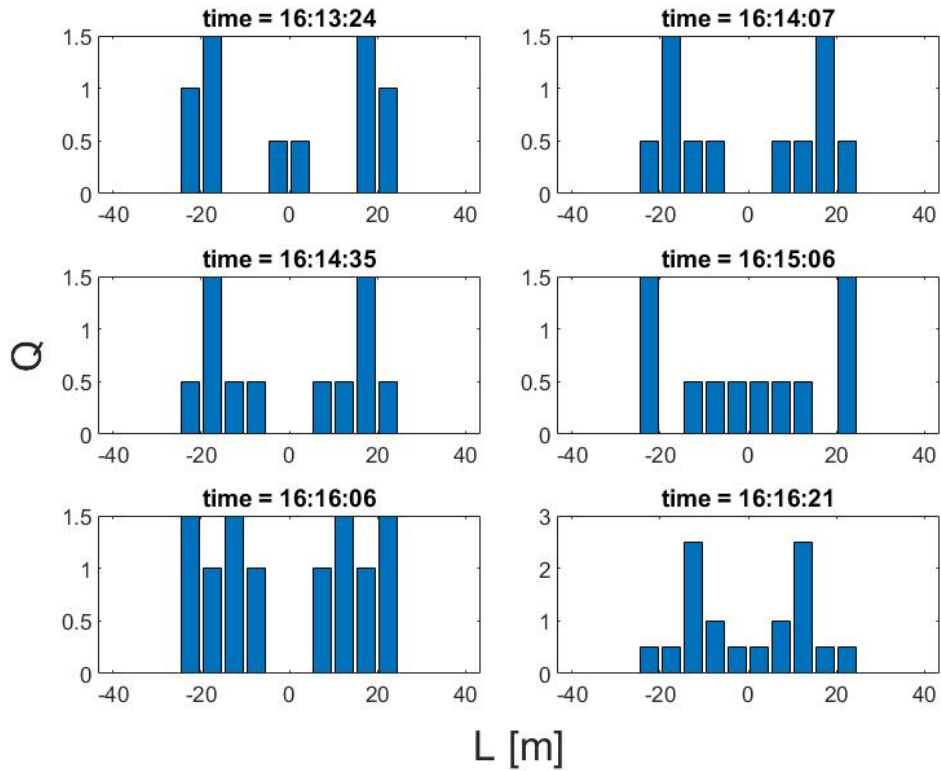


Figure 6.27: Distance-neighbor graph related to the 10/02/22 experiment at OAVdA. The dispersion of 4 balloons tied to the ground by a thread about 15 meters long is shown. The distance parameter h was chosen to be 5 meters. The effect of the constraints is clearly visible; the peaks oscillate around distances of about 20 meters (2).



Figure 6.28: Experimental setup on 10/02/22 at OAVdA with ground-tied probes.

From the graphs above, it is possible to observe the dispersion phenomenon, remembering, however, that it is not the free dispersion in the atmosphere since the probes are bound to the ground by a thread. In fact, it is possible to see that after an initial dispersion, with the peaks moving to greater distances, an almost stationary situation follows with the peaks tending to oscillate around the 20-meter value. This is clearly the effect of a constrained type of dispersion.

Several distance-neighbor graphs related to the last experiment will now be shown. The Q values will be calculated at several time instants separated by 150 seconds. The time instant 0s does not correspond to the launch, but to a later moment. In addition, Q values will be calculated assuming that the computational domain is divided into h-intervals with lengths of 20, 50 and 100 meters. The curves in the graphs were obtained by linear interpolation of the calculated values.

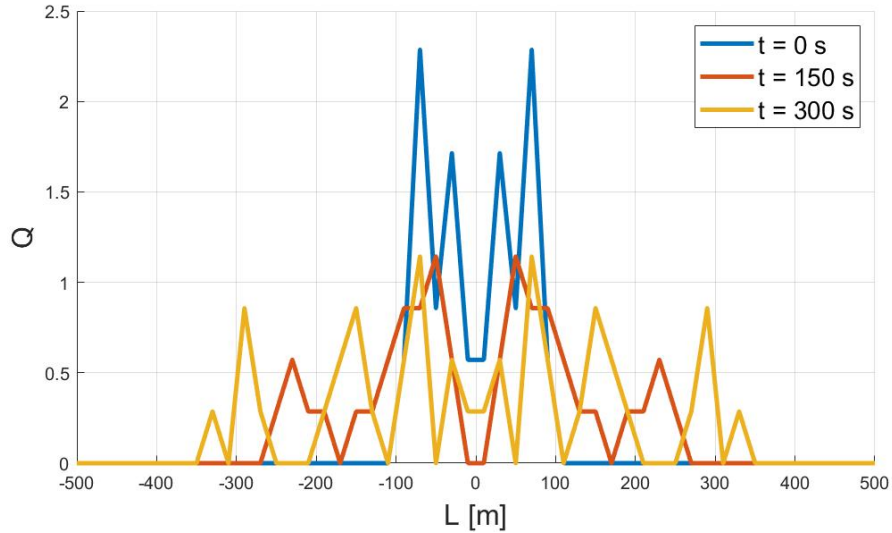


Figure 6.29: Distance-neighbor graph concerning the unconstrained dispersion of 7 balloons using $h = 20m$ as distance parameter. The first 3 instants of time considered (0s, 150s, 300s) are shown. The effects of the absence of constraints in the dispersion can be seen: the peaks move to higher mutual distances and the curves tend to flatten.

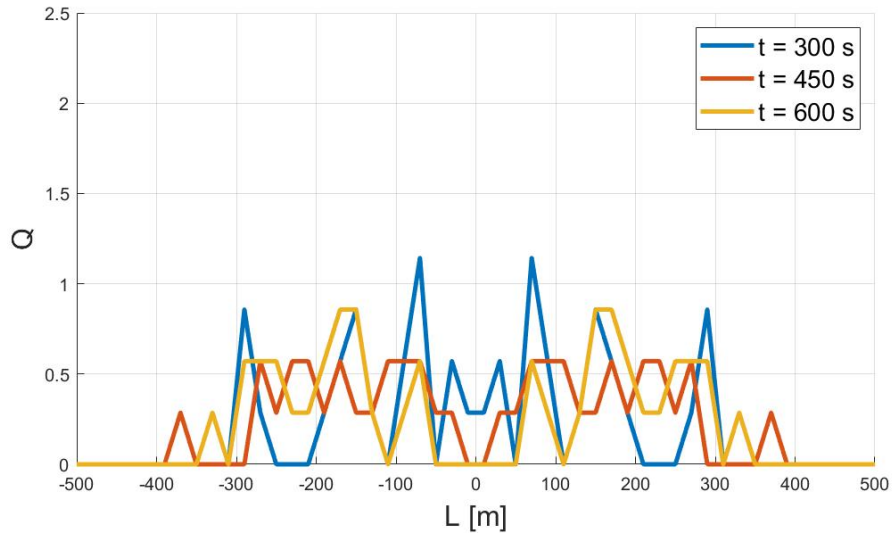


Figure 6.30: Distance-neighbor graph concerning the unconstrained dispersion of 7 balloons using $h = 20m$ as distance parameter. The last 3 instants of time considered (300s, 450s, 600s) are shown. Having used a low h value, it can be seen that the curves have many slight sparse peaks; there are not enough particles within the cells to make a good statistic.

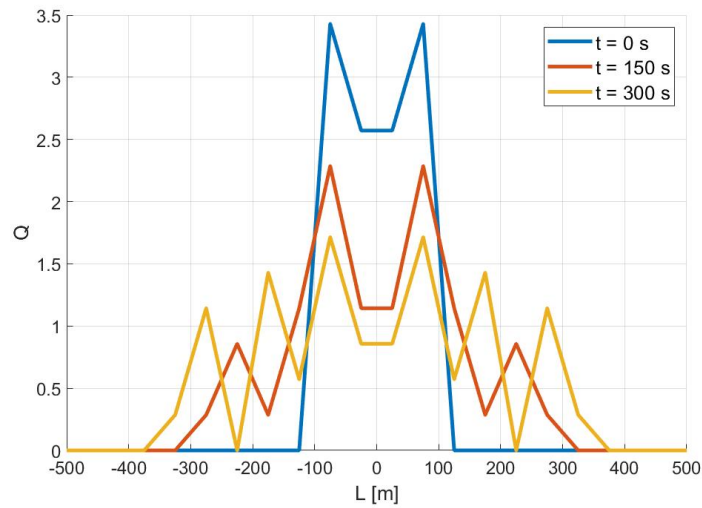


Figure 6.31: Distance-neighbor graph concerning the unconstrained dispersion of 7 balloons using $h = 50m$ as distance parameter. The first 3 instants of time considered (0s, 150s, 300s) are shown.

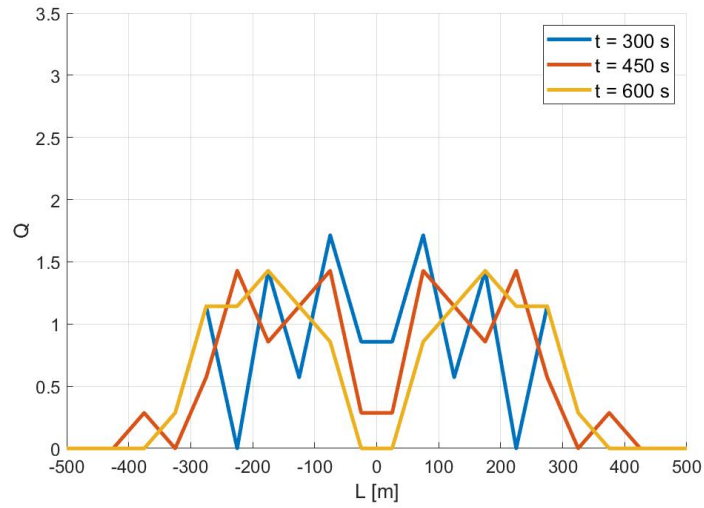


Figure 6.32: Distance-neighbor graph concerning the unconstrained dispersion of 7 balloons using $h = 50m$ as distance parameter. The last 3 instants of time considered (300s, 450s, 600s) are shown. The value of h chosen for this graph seems to be a good compromise to describe this dispersion situation.

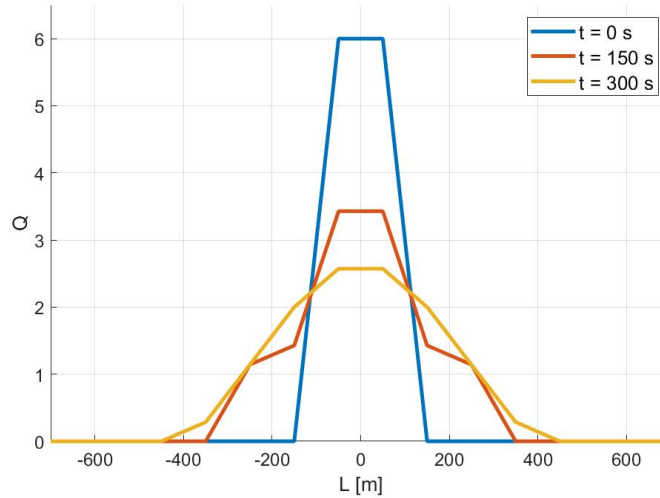


Figure 6.33: Distance-neighbor graph concerning the unconstrained dispersion of 7 balloons using $h = 100m$ as distance parameter. The first 3 instants of time considered (0s, 150s, 300s) are shown. Having used a high h value, it can be seen that the resolution of the graph is quite low.

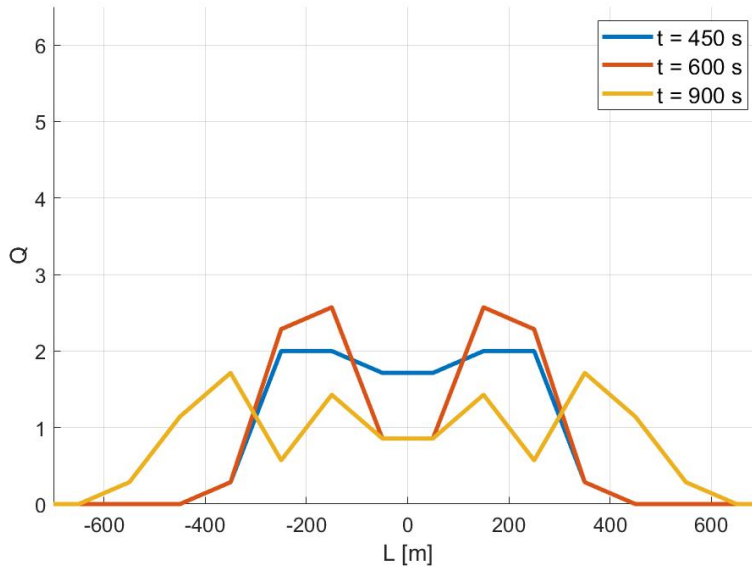


Figure 6.34: Distance-neighbor graph concerning the unconstrained dispersion of 7 balloons using $h = 100m$ as distance parameter. The last 3 instants of time considered (450s, 600s, 900s) are shown. It is possible to see that after a large time interval (900s) some balloons reached considerable distances from each other, in the range of 400-600 meters.

Looking at the graphs above, it is immediately possible to see the differences with the relative graphs of the previous experiment; in these graphs, in fact, the characteristics of particle dispersion can be seen. For any value of h chosen, the same trend is found: as time increases, the peaks tend to shift to higher mutual distances (intervals $(n - 1, n)h$) between the probes. This appears clearly in figure 6.28 and 6.29 where in the plot for $h = 100m$ we see how the peak moves from $(0 - 1)h$ gradually to the right until it reaches $(3 - 4)h$ for the last sampled instant, $t = 900s$. However, having selected a rather high h interval, the resolution of the graph will obviously be low, in fact, looking at the previous graphs in figures 6.24, 6.25, 6.26 and 6.27 it is possible to see that for $h = 20$ and $h = 50$ the resolution is definitely higher and different peaks can be observed for intermediate distances. This also goes to indicate that as the particles disperse there continue to be

turbulent motions that cause them to move away and get closer again and again.

The graphs just shown and commented were made with a very small statistical sample, only 7 particles. This type of analysis, to be effective, would require at least a hundred elements so that enough particles are present within the h-calculation cells without the need to use values of h that are too high, compromising the resolution of the graphs. The number of probes launched was low due to essentially operational issues, difficulty in producing a large number of balloons in a reliable and sustainable manner, and difficulty in receiving data from such a large number of radiosondes. More tests and experiments will be conducted in the future in order to increase the number of elements launched to hundreds.

6.4 Validation by stereo vision

Another system that was tested during this experiment is the two-camera setup that would allow positioning data to be obtained independently from the probes. Once this method is found to be reliable, the position data derived from it could be used to validate and confirm the data from the GNSS modules. Two types of analysis were considered: the first, more automated, makes use of appropriate algorithms; the second, making use of appropriate calibration attempts to obtain a law that interpolates the ratio of physical length to pixels on a video frame as distance varies. It was only possible to obtain results with the second methodology.

6.4.1 Preparation and setup

This subsection will discuss the tools used and how to prepare and use them in order to carry out a stereo vision analysis. Since this is a very complex mechanism, there are many problems that can arise during the various stages, and it is also easy to make mistakes.

For example, if small mistakes are made during the calibration or filming phase, the whole system is likely to fail. Extreme care is needed; camera parameters must remain fixed throughout operations, reference distances must be measured, and images of appropriate reference objects must be taken. Other errors may be due to the technical characteristics of the camera or environmental situations. If the camera sensor does not have sufficient resolution, an object moving away will occupy a very small number of pixels in the frame, causing errors. Regarding environmental factors, it is possible to mention the light situation, which should be neither too strong nor too weak (overexposed or underexposed images). At their turn, areas characterized by low contrast or little texture (sky, homogeneous regions) are another source of error. To conclude, one can mention the imperfect visibility or uniqueness of the object to be studied in the frame and also its motion; high speeds can result in appearing in more pixels than are actually occupied if the camera frame rate is not sufficiently high.

The equipment used for filming are:

- two Sony HDV cameras with a resolution of 1440 x 1080 pixels;
- two professional tripods;
- two balloons marked via red and black spray paint.

Considerations can be made about the painted balloons. To make them, two flat balloons were taken and laid on the ground. They were sprayed with red and black paint, respectively, and allowed to dry. Once they were ready, they were inflated and it was noticed that their flight performance was severely affected: they were found to be no longer able to rise into the air. This fact meant that the amount of paint adhered to them was several grams, thus negating their aerostatic thrust. This, since it had already been decided to launch the probes with two balloons, did not bring additional problems. In the

next experiments, therefore, it would be good not to spray paint the balloons so as not to affect their effectiveness; in case it is necessary to paint them, they should be properly oversized.



Figure 6.35: Sony HDV camera ready to shoot and freshly painted balloon.

The cameras were placed at two points, having the following coordinates.

Camera A (on the right):

- latitude = 45.78993° ;
- longitude = 7.477844° ;
- altitude = 1673m.

Camera B (on the left):

- latitude = 45.789815° ;
- longitude = 7.4777797° ;
- altitude = 1673m.

The next image shows schematically the placement of the cameras:

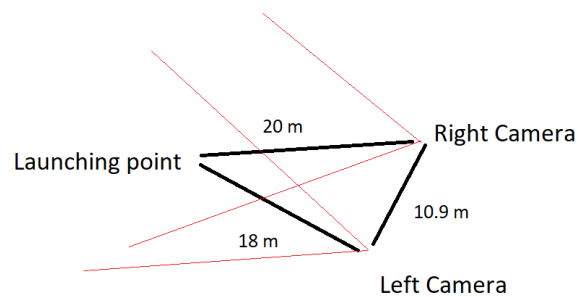


Figure 6.36: Schematic representation of the position of the cameras and their field of view, in relation to the launch position.

As can be seen from the sketch, the two cameras were placed at a mutual distance of 10.9 meters and 18 and 20 meters, respectively, from the launching point. The cameras were arranged in this way to get a good shot over the area where the balloons will move immediately after launching; the background is a mountainous (dark) area so as to increase the contrast with the (white) balloons.

6.4.2 Stereo vision attempt through OpenCv

The principle on which stereo vision is based is the so-called "disparity," a phenomenon that causes the perception of distance (even in human sight). Supposing we capture an object with two cameras, it is possible to notice how the object appears in different areas in the two images taken; by superimposing the two images, it is possible to calculate the distance between the two objects (relative to a certain axis), which corresponds precisely to the value of disparity.

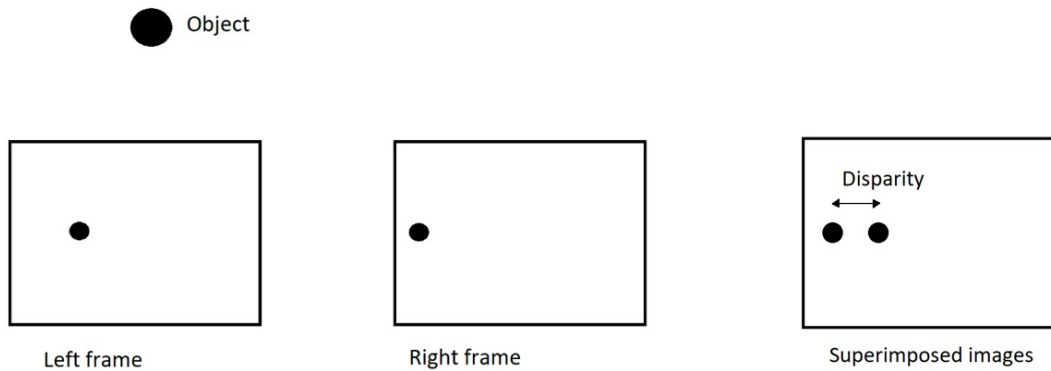


Figure 6.37: Concept of disparity: difference in the placement of an object on two frames taken from different positions.

It is possible to state that in general the distance of the object from the cameras will turn out to be inversely proportional to the change in the disparity value. Without going into theoretical details, the process can be traced back to 4 basic steps:

- camera calibration;
- image rectification;
- calculation of disparity;
- computation of three-dimensional distance.

The process begins with acquiring parameters and images that through processing allow the camera to be calibrated. Once the images to be analyzed are obtained, it is then possible through parameters computed during calibration to calculate the disparity and trace the distance of the object.

The programming language that was decided to use is Python, integrating the library called "OpenCv." It, is a software library that collects many functions dedicated to com-

puter vision. Several algorithms of this library have been tested, concerning object tracking and stereo vision.



Figure 6.38: Tracker test. In the three consecutive frames it is shown how the algorithm loses tracking of the red balloon as soon as another one approaches it.

Regarding tracking, several types were tried, but none of them proved to be effective; all failed to track the balloons' movements despite the different coloring. The test was carried out on the red balloon; as soon as it is approached by an unpainted one, the tracker gets confused and loses tracking. Considering this, it can be concluded that these tracking systems cannot be used to follow marked balloons at launch as they would lose track of them; during launch the balloons are all close together and a lot of overlapping occurs.

Regarding stereo vision, the algorithms in OpenCv require calibration using special reference figures:

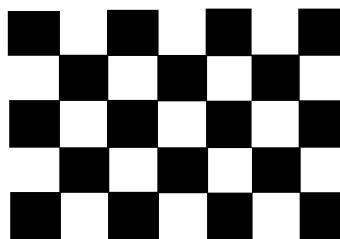


Figure 6.39: Black-white chessboard, reference figure for OpenCv camera calibration.

As shown in the image above, the reference figure needed to carry out camera calibration, which enables image rectification and disparity calculation, is a black-white chess-

board. Once the images containing the reference figure have been taken, they are given as input to the program. It, will locate the angles inside the checkerboard, and, by comparing how these appear in the two images (left and right) manages to extrapolate all the parameters needed for calibration and for subsequent calculations.

In attempting to calibrate the cameras, a problem was encountered. The current stereo vision analysis wants to investigate an area on the order of tens of meters, and therefore, calibration of the cameras cannot for reasons of accuracy be done in close proximity to the cameras. To take sharp and usable images at a distance of 10 to 20 meters would require an extremely large (order of meters) chessboard, which is difficult to achieve and apply. Therefore, an attempt was ultimately made to calibrate using another reference figure and looking for another method, unfortunately without success.

6.4.3 Length-to-pixel ratio variation method

At this point it was decided to use a less automated method, analyzing some frames individually and studying how the ratio of physical length to pixel varies as its distance from the camera varies. As objects of study, balloons painted red and black were again considered. To perform a calibration, it was decided to take as reference some objects of known size taken at different points between the launch area and the cameras; 4 points were considered. In a previous experiment, a similar procedure was attempted using a stick as a reference and two points, obtaining a linear law. Unfortunately, this law is not suitable to describe this situation, since an object moving away from a camera sees its size decrease first very quickly and then very slowly. For this reason, an attempt was made to find a power interpolating law, of the type:

$$y = a(x^b) + c$$

Considering the following data:

Distance	Length	Pixel	Lenght-pixel ratio
5.5 m	44.0 cm	143 p	0.308 cm/p
6.5 m	44.0 cm	115 p	0.383 cm/p
12.5 m	24.0 cm	32 p	0.750 cm/p
22.3 m	149.9 cm	125 p	1.199 cm/p

Figure 6.40: Objects taken as reference to find an interpolating law. A cardboard box was used for the first three data, and a segment of a fence was taken for the fourth. The measurements are relative to the horizontal axis.

it was possible to derive the following law:

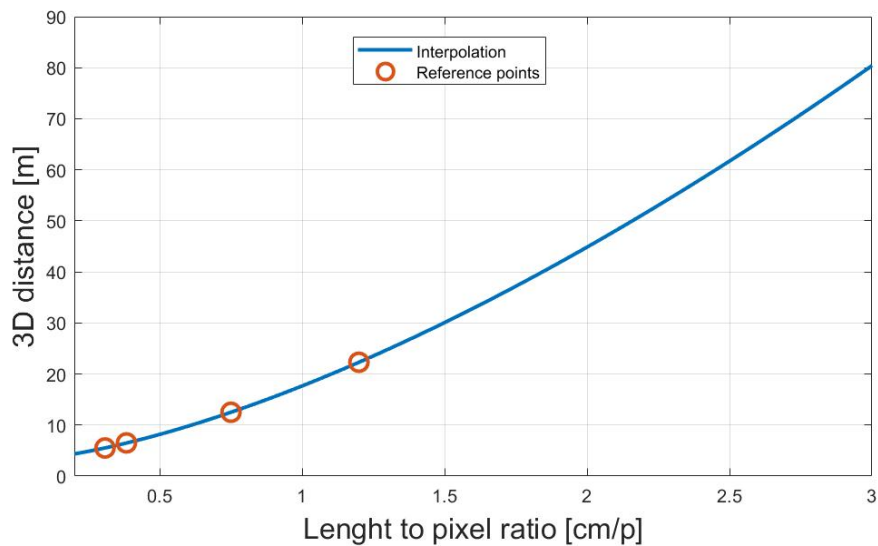


Figure 6.41: Trend obtained by interpolating with a power law the reference ratios measured and given in the table above. The interpolating function is: $y = a(x^b) + c$ where x is the length-pixel ratio, y is the distance to the camera, $a = 14.59$, $b = 1.518$ and $c = 3.078$.

Taking the power law previously written, it was derived that:

$$y = a(x^b) + c$$

where x is the length-pixel ratio, y is the distance to the camera, $a = 14.59$, $b = 1.518$ and $c = 3.078$.

At this point the comparison with the distances obtained from GNSS can be made. The GNSS module integrated into the PCB (zoe-m8b) claims the following accuracies:

- horizontal accuracy: ± 3.5 m (Super E-mode, power saving setting);
- vertical accuracy: ± 7 m (twice the horizontal accuracy is assumed)

The method that has been developed is able to find the distance to an object of known size with only one camera, so the second one will be used as a control. The width of one of the 4 shapes that compose the balloon was taken as the horizontal reference dimension, which is 33 cm. Instead of the diameter relative to the ideal sphere, this was chosen because inflated balloons have a squared shape. Before launching, the balloons were kept tied to a fence for about ten minutes using a thread approximately 1 meter long. This situation will be used to compare the distances obtained with GNSS and cameras. The idea is to detect the maximum and minimum distance the balloon takes on as it swings around the fence using interpolating law and cameras. In this way, it will be possible to check whether the positions given by the GNSS oscillate within this range.

To calculate the uncertainty of the 3d-distance obtained through GNSS measurements, a simple code was written in MatLab that is able, given the GNSS module uncertainties, to calculate the maximum overestimation and the minimum underestimation; calculating the difference between these two values and that of the estimated distance, the higher result was taken as the uncertainty associated with the 3d-distance from the camera.

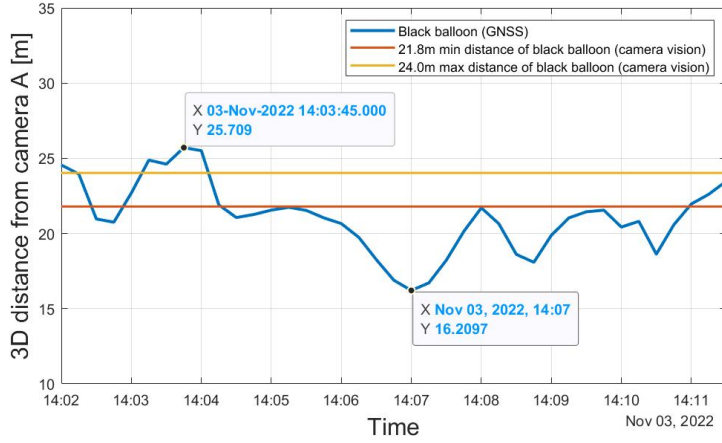


Figure 6.42: Comparison of distances obtained from GNSS and camera vision between the black balloon and camera A. The two horizontal lines represent the nearest (21.8m) and furthest (24.0m) position seen by the camera during the oscillation around the fence, respectively. Also, the nearest and farthest position obtained from the GNSS were highlighted: $16.2 \pm 6.2\text{m}$, $25.7 \pm 6.6\text{m}$.

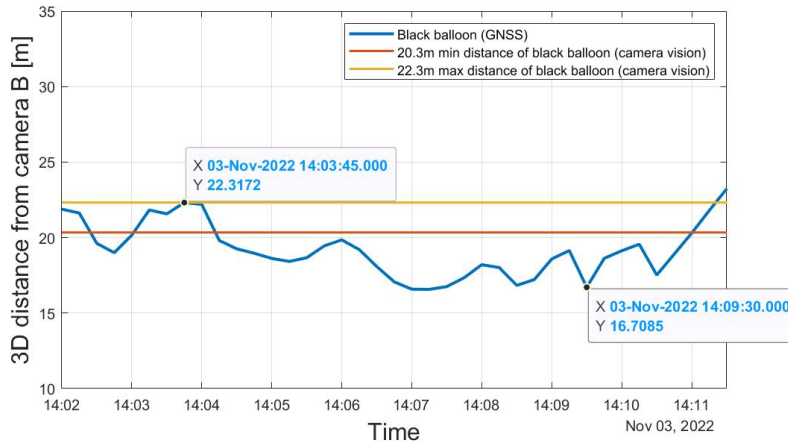


Figure 6.43: Comparison of distances obtained from GNSS and camera vision between the black balloon and camera B. The two horizontal lines represent the nearest (20.3m) and furthest (22.3m) position seen by the camera during the oscillation around the fence, respectively. Also, the nearest and farthest position obtained from the GNSS were highlighted: $16.7 \pm 7.3\text{m}$, $22.3 \pm 7.3\text{m}$.

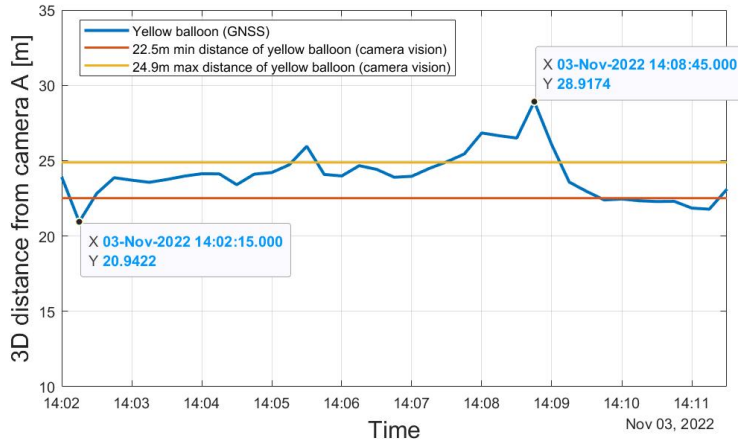


Figure 6.44: Comparison of distances obtained from GNSS and camera vision between the yellow balloon and camera A. The two horizontal lines represent the nearest (22.5m) and furthest (24.9m) position seen by the camera during the oscillation around the fence, respectively. Also, the nearest and farthest position obtained from the GNSS were highlighted: $20.9 \pm 7.3\text{m}$, $28.9 \pm 7.7\text{m}$.

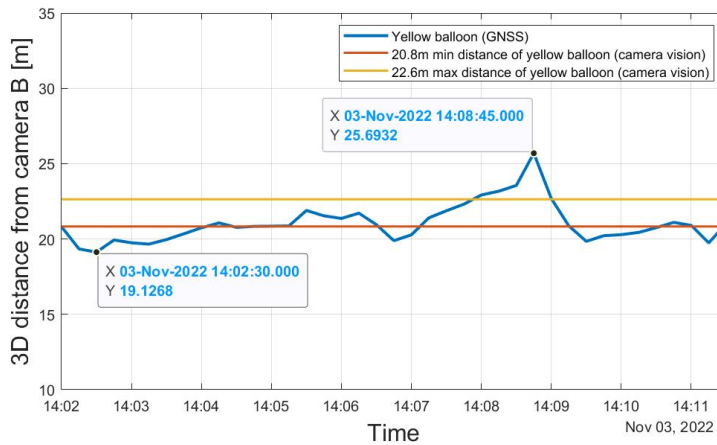


Figure 6.45: Comparison of distances obtained from GNSS and camera vision between the yellow balloon and camera B. The two horizontal lines represent the nearest (20.8m) and furthest (22.6m) position seen by the camera during the oscillation around the fence, respectively. Also, the nearest and farthest position obtained from the GNSS were highlighted: $19.1 \pm 7.3\text{m}$, $25.7 \pm 7.7\text{m}$.

From the graphs just shown, it can be seen that the data from the GNSS do not lie precisely within the range seen by the cameras; however, the measured positions are in agreement with the calculated measurement uncertainties. Both cameras detect the same situation. It was not possible to repeat the verification for the red balloon because the probe attached to it did not transmit enough data during this period. For this reason, another balloon was chosen for testing, unpainted but attached to an additional yellow latex balloon, making it recognizable. In the text, we will refer to this balloon as the "yellow balloon."

At this point, it is interesting to make a comparison between the relative distances obtained through GNSS data and those obtained through cameras. The two balloons just discussed, the black one and the yellow one (RS21, RS22), were chosen for comparison. In the GNSS case it is straightforward to calculate the distances in question while using the cameras and having only the absolute distance it was necessary to make approximations. Since the balloons are attached to the fence and therefore at about the same elevation, the problem was assumed to be two-dimensional. Once this was done, by calculating the horizontal distance between the two balloons, making projections and using triangles it was possible to derive the relative distance.

The two balloons were tied to the fence at a distance of about one meter by a thread also about one meter in length . For this reason, we expect to observe small relative distances, within a couple of meters. Relative distances were considered in absolute value. To perform the video analysis, camera B was used since it had a better view over the balloons.

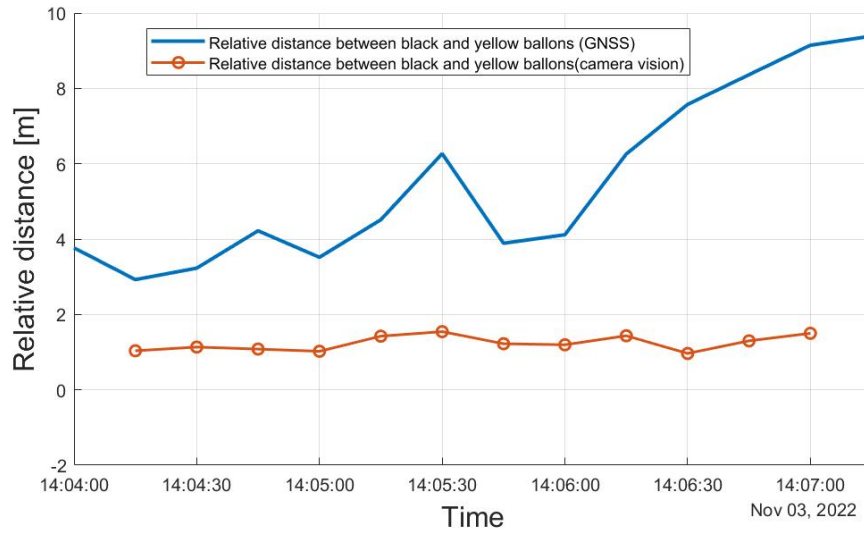


Figure 6.46: The graph shows the comparison of the relative distance between the black and yellow balloons (RS21, RS22) obtained by GNSS and camera during oscillation at the fence. It is possible to observe a discrepancy between the two curves, however, the difference lies within the tolerance calculated for the measurements obtained from the GNSS modules.

Time	Relative distance (Camera vision)	Relative distance (GNSS)
14:04:15	1.03 m	2.93 ± 16.2 m
14:04:30	1.13 m	3.23 ± 16.4 m
14:04:45	1.08 m	4.22 ± 16.2 m
14:05:00	1.02 m	3.52 ± 16.4 m
14:05:15	1.42 m	4.51 ± 16.1 m
14:05:30	1.54 m	4.11 ± 16.0 m
14:05:45	1.22 m	3.89 ± 15.3 m
14:06:00	1.20 m	4.11 ± 15.2 m
14:06:15	1.43 m	6.26 ± 14.4 m
14:06:30	0.97 m	7.57 ± 13.4 m
14:06:45	1.30 m	8.36 ± 13.5 m
14:07:00	1.50 m	9.14 ± 14.1 m

Figure 6.47: Table showing the relative distances during the oscillation at the fence between the black and yellow balloon (RS21, RS22) obtained by GNSS and camera. A period of about three minutes was analyzed. Uncertainties are high because two data from the GNSS module are used to calculate the relative distance.

In the graph above it is possible to observe the relative distance between the black and yellow balloon during oscillation at the fence. In particular, the comparison between the values obtained through GNSS data and those obtained through the camera is shown. Since the distance was considered in absolute value, no negative values are present. A difference can be seen between the two curves, in particular it seems that GNSS tends to overestimate the values. The curve obtained via camera is to be considered reliable since it shows values that are plausible with the geometry of the problem (length of wires and distance to the fence). However, considering the error that affects the values calculated by GNSS, the difference with the curve obtained by camera falls within the uncertainty range. The uncertainty of these measurements turns out to be about twice that of the distances from the cameras because in this case two data from the GNSS module of the probes are used instead of one.

It might have been interesting to make a comparison of the data during the launch. This comparison was not made for several reasons. For GNSS, the data transmitted by the probes at those instants turn out to be insufficient to draw a reliable curve. For video analysis, on the other hand, it was noted that the balloons move rapidly at the edges of the frame, so, the calculated dimensions will be affected by the distortion caused by the lens and therefore not reliable.

After performing these tests, it appears possible to state that even if there was some loss of data, the values from the GNSS that were transmitted correctly are consistent with the uncertainty values provided by the manufacturer and are therefore usable.

Chapter 7

Conclusions and future improvements

After having explained the principles of turbulence and warm cloud formation, discussed balloon sizing, and analyzed the results of an experiment, it is possible to make some concluding comments. As explained throughout the text, obtaining experimental data in a reliable manner using small radiosondes that follow atmospheric flows in a Lagrangian manner is very challenging, and is still a limitation in the study of cloud microphysics. For this reason, the MSCA-ITN-COMPLETE project aims, through the development of a biodegradable and ultralight radiosonde-balloon system, to fill this gap. This, being an ongoing project began well before the start of my thesis work; my task has been to make a contribution to a job that others have been working on before me and others will participate in the future.

In this thesis work, a systematic study of Mater-Bi balloon sizing was carried out by making graphs containing trends of weight, size and aerostatic thrust, which was followed by experimental validation by making balloons of different sizes. The performance of an

industrially made balloon in natural rubber was then tested and compared with that of Mater-Bi balloons. From these tests, it was possible to conclude that the performance of the two balloons are comparable; however, the rubber balloons in spite of their superior reliability and versatility have the drawback of being stretchable, and consequently have their volume varying on the basis of atmospheric pressure. As a consequence, the balloon buoyancy also increases; additional tests will need to investigate this aspect further.

An experiment was then carried out at OAVdA that made it possible to test the simultaneous use of a larger number of probes than in previous experiments and the behavior of the balloons in a case of unconstrained dispersion, which had also never been tested before. Prior to the launch there was a calibration phase, using temperature data obtained through instrumentation provided by INRIM it was possible to verify the reliability of the data from the probes. In addition, through the use of two cameras, it was possible to validate the positioning data coming from the GNSS modules; these data, while having discrepancies with those obtained from the cameras are within the accuracy range provided by the module manufacturer. Several critical issues were encountered during the experiment. The first was to fill all balloons with the same amount of helium, which is not feasible manually. For this reason, plans were made to design an automatic inflation system that would allow uniformity and accuracy in inflation. Another problem was leakage at the bottom of some balloons; this could be solved by testing the use of the new shape proposed in the text or by using industrially produced balloons. There were also problems in the area of transmission; in fact, several probes did not transmit continuously and stopped transmission earlier than expected. This aspect, which can be traced to a problem in the radio module of the probes or at the ground stations, will have to be well analyzed as the number of probes will be further increased in the future. A final problem was found in the measurement of relative humidity. It was seen that the sensors were unable to follow the

increase in relative humidity to saturation but peaked significantly earlier despite passing through a dense cloud cover. This problem, however, appears to be common in very small sensors and will need to be studied to limit its magnitude or develop a corrective model.

Despite these critical issues, the launch was performed and numerous data were collected and analyzed: temperature, pressure, humidity, positioning, accelerations, and velocities. Unfortunately, due to the need to launch with two balloons per probe the Lagrangian feature in the motion was lost. In addition to the presentation of the values just mentioned, distance-neighbor graphs related to free dispersion were made and compared with those made from the constrained dispersion data obtained in previous experiments. Not only data were obtained from the experiment, but also useful experience for the realization of the next ones.

Looking to the future and concluding, it is possible to say that many more radiosondes, smaller and lighter (a new PCB prototype is already being produced) may be used. They will be carried by balloons that are also smaller and made of Mater-Bi by improving the construction process or by using industrially produced ones. They will be able to be filled through an automatic system that will make it possible to float at a precise altitude realizing a true Lagrangian case study.

Bibliography

- [1] Shahbozbek Abdunabiev, Tessa C. Basso, Daniela Tordella, Miryam Paredes, Eros Pasero, and Flavio Canavero. Innovative, mini, biodegradable radiosondes to track small-scale fluctuations in warm cloud and clear air environments. In *APS Division of Fluid Dynamics Meeting Abstracts*, APS Meeting Abstracts, page B18.006, November 2019.
- [2] ATmega328P. 8-bit avr microcontrollers. <https://www.microchip.com/wwwproducts/en/ATmega328p>. Accessed on 29 November 2022.
- [3] Tessa C. Basso, Giovanni Perotto, Chiara Musacchio, Andrea Merlone, Athanassia Athanassiou, and Daniela Tordella. Evaluation of mater bi and polylactic acid as materials for biodegradable innovative mini-radiosondes to track small scale fluctuations within clouds. *Materials chemistry and physics*, 253:123411, 2020.
- [4] Eberhard Bodenschatz, Szymon P Malinowski, Raymond A Shaw, and Frank Stratmann. Can we understand clouds without turbulence? *Science*, 327(5968):970–971, 2010.
- [5] Bosch. Humidity sensor bme280. <https://www.bosch-sensortec.com/products/environmental-sensors/humidity-sensors-bme280/>. Accessed on 29 November 2022.

- [6] Jean-Louis Brenguier and Wojciech W. Grabowski. Cumulus entrainment and cloud droplet spectra: A numerical model within a two-dimensional dynamical framework. *Journal of Atmospheric Sciences*, 50(1):120 – 136, 1993.
- [7] S. Businger, R. Johnson, and Robert Talbot. Scientific insights from four generations of lagrangian smart balloons in atmospheric research. *Bulletin of The American Meteorological Society - BULL AMER METEOROL SOC*, 87, 11 2006.
- [8] K Chang, J Bench, M Brege, Will Cantrell, K Chandrakar, David Ciochetto, Claudio Mazzoleni, LR Mazzoleni, Dennis Niedermeier, and RA Shaw. A laboratory facility to study gas–aerosol–cloud interactions in a turbulent environment: The π chamber. *Bulletin of the American Meteorological Society*, 97(12):2343–2358, 2016.
- [9] Ken B Cooper and Goutam Chattopadhyay. Submillimeter-wave radar: Solid-state system design and applications. *IEEE microwave magazine*, 15(7):51–67, 2014.
- [10] CORDIS. European commission. cloud-microphysics-turbulence-telemetry: An inter-multidisciplinary training network for enhancing the understanding and modeling of atmospheric clouds. complete project. h2020. <https://cordis.europa.eu/project/id/675675>. Accessed on 24 November 2022.
- [11] B. J. Devenish, P. Bartello, J.-L. Brenguier, L. R. Collins, W. W. Grabowski, R. H. A. IJzermans, S. P. Malinowski, M. W. Reeks, J. C. Vassilicos, L.-P. Wang, and Z. Warhaft. Droplet growth in warm turbulent clouds. *Quarterly Journal of the Royal Meteorological Society*, 138(667):1401–1429, 2012.
- [12] Paul E DIMOTAKIS. Turbulent mixing. *Annual review of fluid mechanics*, 37(1):329–356, 2005.

- [13] National Centers for Environmental Information (NCEI)/National Climatic Data Center (NCDC). Picture climate: Balloons aren't just for birthdays. <https://www.ncdc.noaa.gov/news/picture-climate-balloons-aren%E2%80%99t-just-birthdays>. Accessed on 24 November 2020.
- [14] Wojciech W GRABOWSKI and Lian-Ping WANG. Growth of cloud droplets in a turbulent environment. *Annual review of fluid mechanics*, 45(1):293–324, 2013.
- [15] Richard Hamblyn. Luke Howard, namer of clouds. *Weather*, 77(11):376–379, 2022.
- [16] Hoperf. Rfm95w feature the loratm long range model. <https://www.hoperf.com/modules/lora/RFM95.html>. Accessed on 29 November 2022.
- [17] WA Hoppel, GM Frick, JW Fitzgerald, and BJ Wattle. A cloud chamber study of the effect that nonprecipitating water clouds have on the aerosol size distribution. *Aerosol science and technology*, 20(1):1–30, 1994.
- [18] John C Hubbert, James W Wilson, Tammy M Weckwerth, Scott M Ellis, Mike Dixon, and Eric Loew. S-pol's polarimetric data reveal detailed storm features (and insect behavior). *Bulletin of the American Meteorological Society*, 99(10):2045–2060, 2018.
- [19] P.R. Jonas. Turbulence and cloud microphysics. *Atmospheric research*, 40(2):283–306, 1996.
- [20] P. Kratochvi. <https://www.publicdomainpictures.net/en/view-image.php?image=438663&picture=cirrus-clouds>. Accessed on 23 March 2023.
- [21] Ralph F. Kresge. NOAA photo library. weather wonders, clouds, stratus. <https://photolib.noaa.gov/Collections/National-Weather-Service/Other/emodule/627/eitem/18666>. Accessed on 10 December 2022.

- [22] N. Kuba and Y. Fujiyoshi. Development of a cloud microphysical model and parameterizations to describe the effect of ccn on warm cloud. *Atmospheric Chemistry and Physics*, 6(10):2793–2810, 2006.
- [23] Bipin Kumar, Paul Götzfried, Neethi Suresh, Jörg Schumacher, and Raymond A Shaw. Scale dependence of cloud microphysical response to turbulent entrainment and mixing. *Journal of Advances in Modeling Earth Systems*, 10(11):2777–2785, 2018.
- [24] Bipin Kumar, Jörg Schumacher, and Raymond A Shaw. Lagrangian mixing dynamics at the cloudy–clear air interface. *Journal of the Atmospheric Sciences*, 71(7):2564–2580, 2014.
- [25] Pijush K Kundu and Ira M Cohen. *Fluid Mechanics*. Academic Press, 2007.
- [26] Dennis Lamb and Johannes Verlinde. *Physics and Chemistry of Clouds*. Cambridge University Press, Cambridge, 2011.
- [27] Katrin Lehmann, Holger Siebert, and Raymond A Shaw. Homogeneous and inhomogeneous mixing in cumulus clouds: Dependence on local turbulence structure. *Journal of the Atmospheric Sciences*, 66(12):3641–3659, 2009.
- [28] ST life. Augmented. lsm6dsm. inemo inertial module: Always-on 3d accelerometer and 3d gyroscope. <https://www.st.com/en/mems-and-sensors/lsm6dst.html>. Accessed on 29 November 2022.
- [29] S. P. Malinowski, H. Gerber, I. Jen-La Plante, M. K. Kopec, W. Kumala, K. Nurowska, P. Y. Chuang, D. Khelif, and K. E. Haman. Physics of stratocumulus top (post): turbulent mixing across capping inversion. *Atmospheric Chemistry and Physics*, 13(24):12171–12186, 2013.

- [30] Szymon P Malinowski, H Gerber, Jen-La Plante, MK Kopec, Wojciech Kumala, Katarzyna Nurowska, PY Chuang, Djamal Khelif, KE Haman, et al. Physics of stratocumulus top (post): turbulent mixing across capping inversion. *Atmospheric Chemistry and Physics*, 13(24):12171–12186, 2013.
- [31] L. Mallette. <https://www.publicdomainpictures.net/it/view-image.php?image=290510&picture=cumuli>. Accessed on 23 March 2023.
- [32] Meteorologiaenred. Cumulonimbus. <https://www.meteorologiaenred.com/it/cumulonembi.html>. Accessed on 10 December 2022.
- [33] NOAA. Air resources laboratory. low altitude balloon measurement platforms. https://www.arl.noaa.gov/wp_arl/wp-content/uploads/Review/Posters/Balloon.pdf. Accessed on 24 November 2022.
- [34] NOAA. The water cycle. (dennis cain/nws). <https://www.noaa.gov/education/resource-collections/freshwater/water-cycle>. Accessed on 6 December 2022.
- [35] Miryam E. Paredes Quintanilla, Shahbozbek Abdunabiev, Marco Allegretti, Andrea Merlone, Chiara Musacchio, Eros G. A. Pasero, Daniela Tordella, and Flavio Canavero. Innovative mini ultralight radioprobes to track lagrangian turbulence fluctuations within warm clouds: Electronic design. *Sensors*, 21(4), 2021.
- [36] H. Pawlowska, W. W. Grabowski, and J.-L. Brenguier. Observations of the width of cloud droplet spectra in stratocumulus. *Geophysical research letters*, 33(19):L19810–n/a, 2006.
- [37] Jimmy Philip and Ivan Marusic. Large-scale eddies and their role in entrainment in turbulent jets and wakes. *Physics of fluids (1994)*, 24(5):055108–055108–10, 2012.

- [38] Mark Pinsky and Alexander Khain. Theoretical analysis of the entrainment–mixing process at cloud boundaries. part i: Droplet size distributions and humidity within the interface zone. *Journal of the Atmospheric Sciences*, 75(6):2049 – 2064, 2018.
- [39] S.B. Pope and S.B. Pope. *Turbulent Flows*. Cambridge University Press, 2000.
- [40] Hans R Pruppacher and J. D Klett. *Microphysics of Clouds and Precipitation*. Springer Science + Business Media, Dordrecht, 2. Aufl. edition, 2010.
- [41] Paolo Rey. Regione autonoma valle d’aosta per il progetto transfrontaliero interreg alcotra “exo/eco” realizzato con fondi europei. <https://www.oavda.it/chi-siamo>. Accessed on 06 January 2023.
- [42] Lewis Fry Richardson. Atmospheric diffusion shown on a distance-neighbour graph. *Proceedings of the Royal Society of London. Series A, Containing Papers of a Mathematical and Physical Character*, 110(756):709–737, 1926.
- [43] H. Siebert, S. Gerashchenko, A. Gylfason, K. Lehmann, L.R. Collins, R.A. Shaw, and Z. Warhaft. Towards understanding the role of turbulence on droplets in clouds: In situ and laboratory measurements. *Atmospheric research*, 97(4):426–437, 2010.
- [44] H Siebert, RA Shaw, J Ditas, T Schmeissner, SP Malinowski, E Bodenschatz, and H Xu. High-resolution measurement of cloud microphysics and turbulence at a mountaintop station. *Atmospheric Measurement Techniques*, 8(8):3219–3228, 2015.
- [45] Holger Siebert, Katrin Lehmann, and Manfred Wendisch. Observations of small-scale turbulence and energy dissipation rates in the cloudy boundary layer. *Journal of the atmospheric sciences*, 63(5):1451–1466, 2006.

- [46] Sara Swenson, Brian Argrow, Eric Frew, Steve Borenstein, and Jason Keeler. Development and deployment of air-launched drifters from small uas. *Sensors*, 19(9):2149, 2019.
- [47] Ublox. Zoe-m8b—ultra-small, super low-power u-blox m8 gnss sip module. data sheet; ubx-17035164; u-blox: Thalwil, switzerland, 2020. https://www.u-blox.com/sites/default/files/ZOE-M8B_DataSheet_%28UBX-17035164%29.pdf. Accessed on 23 January 2021.
- [48] Metoffice UK. Cloud names and classifications. <https://www.metoffice.gov.uk/weather/learn-about/weather/types-of-weather/clouds/cloud-names-classifications#:~:text=The%20classification%20of%20clouds%20into,an%20infinite%20variety%20of%20forms>. Accessed on 9 December 2022.
- [49] Roger Williams University. Earth’s heat budget. <https://rwu.pressbooks.pub/webboceanography/chapter/8-1-earths-heat-budget/>. Accessed on 6 December 2022.
- [50] P. A. Vaillancourt, M. K. Yau, P. Bartello, and W. W. Grabowski. Microscopic approach to cloud droplet growth by condensation. part ii: Turbulence, clustering, and condensational growth. *Journal of the Atmospheric Sciences*, 59(24):3421 – 3435, 2002.
- [51] Gary A Wick, Terrence F Hock, Paul J Neiman, Holger Vömel, Michael L Black, and J Ryan Spackman. The near-noaa global hawk dropsonde system. *Journal of Atmospheric and Oceanic Technology*, 35(8):1585–1604, 2018.